Measurement of the angular and lifetime parameters in the decays $B_d^0 \to J/\psi K^{*0}$ and $B_s^0 \to J/\psi\phi$

Gilberto Alejandro García Guerra

January 16, 2009

Resumen

Presentamos las mediciones de las amplitudes lineales de polarización y de las fases relativas fuertes que describen a los decaimientos *flavor-untagged* $B_d^0 \to J/\psi K^{*0}$

$$\begin{aligned} |A_0|^2 &= 0.587 \pm 0.011\,(\text{stat}) \pm 0.013\,(\text{syst}) \\ |A_\parallel|^2 &= 0.230 \pm 0.013\,(\text{stat}) \pm 0.025\,(\text{syst}) \\ \delta_1 &= -0.381^{+0.060}_{-0.061}\,(\text{stat}) \pm 0.090\,(\text{syst})\,\text{rad} \\ \delta_2 &= 3.21 \pm 0.06\,(\text{stat}) \pm 0.06\,(\text{syst})\,\text{rad} \end{aligned}$$

y $B_s^0 \to J/\psi\phi$

$$\begin{aligned} |A_0|^2 &= 0.555 \pm 0.027\,(\text{stat}) \pm 0.006\,(\text{syst}) \\ |A_\parallel|^2 &= 0.244 \pm 0.032\,(\text{stat}) \pm 0.014\,(\text{syst}) \\ \delta_\parallel &= 2.72^{+1.12}_{-0.27}\,(\text{stat}) \pm 0.26\,(\text{syst})\,\text{rad} \end{aligned}$$

en la base de transversidad. También se reporta la vida media $\bar{\tau}_s$ de los eigenestados de masa del mesón B_s^0 y la razón de tiempo de vida $\bar{\tau}_s/\tau_d$

$$\frac{\bar{\tau}_s}{\tau_d} = 1.053^{+0.062}_{-0.061}\,(\text{stat}) \pm 0.015\,(\text{syst})$$

Los análisis están basados en aproximadamente 2.8 fb^{-1} de datos recabados con el detector D0 desde Abril de 2003 a Agosto de 2007. De las mediciones de los parámetros angulares concluimos que no existe evidencia de una desviación de la simetría de sabor SU(3) para estos decaimientos y que la suposición de factorización no es válida para el decaimiento $B_d^0 \to J/\psi K^{*0}$.

Abstract

We present measurements of the linear polarization amplitudes and the strong relative phases that describe the flavor-untagged decays $B_d^0 \to J/\psi K^{*0}$

$$\begin{aligned} |A_0|^2 &= 0.587 \pm 0.011\,(\text{stat}) \pm 0.013\,(\text{syst}) \\ |A_\parallel|^2 &= 0.230 \pm 0.013\,(\text{stat}) \pm 0.025\,(\text{syst}) \\ \delta_1 &= -0.381^{+0.060}_{-0.061}\,(\text{stat}) \pm 0.090\,(\text{syst})\,\text{rad} \\ \delta_2 &= 3.21 \pm 0.06\,(\text{stat}) \pm 0.06\,(\text{syst})\,\text{rad} \end{aligned}$$

and $B_s^0 \to J/\psi\phi$

$$\begin{aligned} |A_0|^2 &= 0.555 \pm 0.027\,(\text{stat}) \pm 0.006\,(\text{syst}) \\ |A_\parallel|^2 &= 0.244 \pm 0.032\,(\text{stat}) \pm 0.014\,(\text{syst}) \\ \delta_\parallel &= 2.72^{+1.12}_{-0.27}\,(\text{stat}) \pm 0.26\,(\text{syst})\,\text{rad} \end{aligned}$$

in the transversity basis. We also measure the mean lifetime $\bar{\tau}_s$ of the B_s^0 mass eigenstates and the lifetime ratio $\bar{\tau}_s/\tau_d$

$$\frac{\bar{\tau}_s}{\tau_d} = 1.053^{+0.062}_{-0.061}\,(\text{stat}) \pm 0.015\,(\text{syst})$$

The analyses are based on approximately 2.8 fb^{-1} of data recorded with the D0 detector from April 2003 to August 2007. From our measurements of the angular parameters we conclude that there is no evidence for a deviation from flavor SU(3) symmetry for these decays and that the factorization assumption is not valid for the $B_d^0 \to J/\psi K^{*0}$ decay.

Acknowledgements

I would like to thank all the people who contribute to this thesis; however they are too numerous to mention all of them here, but deserve many thanks anyway. The following people have special mentions for their contributions.

First of all, and in a very special way, I want to thank my advisor, Dr. Heriberto Castilla Valdez, for all his patience and guidance in this difficult area of experimental high energy physics. It was a very interesting and fruitful experience to be advised by a person who knows a lot of this bussiness and who was always there, working side by side. Heriberto, thank you for all.

My second advisor, Dr. Pedro Podesta Lerma, arrived to Fermilab when this analysis needed more than ever a little push to move forward. His patience, calmness and experience were of great help to me along all the development of this dissertation. The tedious (and important) task of process the data for this analysis was performed by Dr. Alberto Sánchez Hernández. Wihtout his support and experience in this and other important issues, the analysis would be more difficult than it was.

Special thanks to the B physics group, in particular to the conveners Wendy Taylor and Dmitri Tsybychev. I also want to thank the Editorial Board 27 members Rick Van Kooten, Bob Kehoe, and Ron Lipton; the Physics Coordinators Aurelio Juste and Stefan Soldner-Rembold; and the D0 Spokepersons Dmitri Denisov and Darien Wood. Thank you for the comments you have done to improve the quality of this analysis. Important people because of their support are part of the D0 staff: Sonya Wright and Rolando Flores.

Thanks to the members of the jury Dr. Genaro Toledo, Dr. Mauricio Carbajal, and Dr. Gene Fisk for the comments they made to this dissertation.

I want to thank my friends from the CINVESTAV-Mexico group at Fermilab: Estela Garcés, Iván Heredia, Ricardo Magaña, Jorge Martínez and Eduard De la Cruz. Work is always easier when you are surrounded by good people, even inside the *jaula de oro*. Thank you for the good time and jokes we spent together. All of them are now unforgettable moments in my mind.

I met very kind people at Fermilab: Roberto Martínez, Rebekah Davis, José Palomino, Alfonso Castillo, Tino Calancha, Juan Estrada, Lauren Younis, Pedro Ttito, Tatiana Rodríguez, Alexander Rakitin, Suneel Dutt, Gustavo Cancelo, and all the members of the soccer team. Thanks for your company while I was at the United States.

I also want to thank Patricia Villar and Flor Ibañez, both from CINVESTAV staff. Their help was priceless.

In a very special way I want to thank my mother-in-law, Guadalupe Benítez. She took care of my family when I was at the United States. It would not have been the same to work at Fermilab without knowing that my wife and my son were in good hands. Thank you very much.

This dissertation was supported by the Consejo Nacional de Ciencia y Tecnología (CONACyT), the Centro de Investigación y de Estudios Avanzados del IPN (CINVESTAV-Mexico), and by the Fermi National Accelerator Laboratory.

To my wife Marisol and my son Víctor Hugo.

It was hard for all of us to be separated for a long time.

Every page of this thesis is dedicated to you both.

All our efforts and sacrifices are here.

Without your support, this thesis would not be possible.

Thank you very much for waiting.

Flaquita, Campeón, I love you both so much.

To my son Leonardo†*, you'll always be in my heart.*

Contents

List of Tables

List of Figures

Chapter 1

Introduction

The standard model (SM) is a theoretical framework built from observation that predicts and correlates new data. The construction of the SM has been guided by principles of symmetry. In the early 1960's particle physicist described nature in terms of four distinct forces, characterized by widely different ranges and strengths as measured at typical energy scale of 1 GeV. The strong nuclear force (SF) has a range of about a Fermi or 10^{-15} m. The weak force (WF) responsible for radioactive decay, with a range of 10^{-7} m, is about 10^{-5} times weaker at low energy. The electromagnetic force (EF) that governs much of the macroscopic physics has an infinite range and strength determined by the fine structure constant, $\alpha \approx 10^2$. The fourth force, gravity, also has infinite range and a low energy coupling (about 10^{-38}) too weak to be observable in laboratory experiments. The achievement of the SM was the elaboration of a unified description of the SF, WF and EF in the language of quantum gauge field theories. Moreover, the SM combines the WF and EF in a single electroweak gauge theory, reminiscent of Maxwell's unification of the seemingly distinct forces of electricity and magnetism.

The SM includes several intrinsic parameters which have to be measured in experiments. Those parameters are related with different aspects of the theory, i.e., they can be measured via different processes that involve the EF, WF, and SF. The main goal of this dissertation is to measure some of those parameters related with the B_d^0 and B_s^0 mesons. The B_q^0 is made

by an anti-b quark (denoted by $\bar{b}$) and a q quark, where $q = d, s$. In the case of the B_s^0 meson, it is not a pure mass eigenstate, which leads to the chance that this meson can oscillate into its antiparticle ($\bar{B}_s^0$) via weak interacting processes, as shown in Fig. 1.1. Measurements of mixing parameters for these two mesons, the B_d^0 and B_s^0, have been reported widely by the Tevatron [1] and B factories [2].

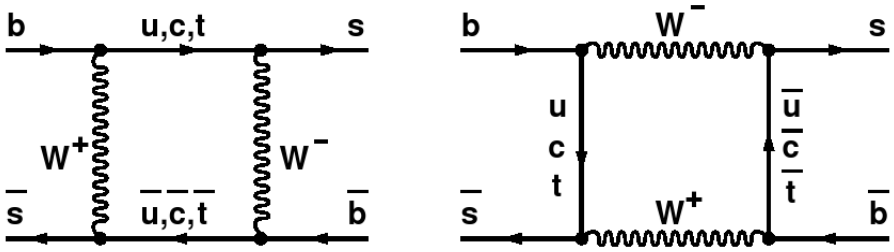

Figure 1.1: SM box diagrams representing the $B_s^0 - \bar{B}_s^0$ mixing

In addition to the mixing parameters, the decay width difference between the mass eigenstates for these mesons is of special interest for the CP violation. The measurement of this feature is important since it can explain the observation that matter is dominant over antimatter in the Universe. The theoretical prediction for the decay width difference for the B_d^0 meson is expected to be small [3]. However, the value for this parameter in the B_s^0 system is expected to be sizeable [3]. Recent measurements of the decay width difference for the B_s^0 system [4] are in agree with this prediction.

Finally, and this is what we will describe in this thesis, the description of the *flavor-untagged*[1] decays $B_d^0 \to J/\psi K^{*0}$ and $B_s^0 \to J/\psi\phi$ in the transversity basis, lead us to measure the linear polarization amplitudes and the strong relative phases that arise naturally in that description. From the measurement of these parameters, we can verify the validity of the factorization assumption and to check if flavor SU(3) symmetry holds for these decays. Furthermore, since we are doing the measurement of both channels, we are able to measure the lifetime ratio $\bar{\tau}_s/\tau_d$. Phenomenological models predict differences of about 1% [3, 5] between the B_d^0 and B_s^0 lifetimes.

[1]Flavor-untagged means that the initial B meson flavor is not determined

1.1 Standard Model

The matter fields are fermions and their antiparticles, with half unit of intrinsic angular momentum, or spin. There are three families of fermions fields that are identical in every attribute except in their masses. The first family includes the up (u) and down (d) quarks that are the constituents of nucleons as well as pions an other mesons responsible for nuclear binding. It also contains the electron and the neutrino emitted with a positron in nuclear β-decay. The quarks of other families are constituents of heavier short-lived particles; they and their companions charged leptons rapidly decay via the WF to the quarks and leptons of the first family.

The spin-1 gauge boson mediate interactions among fermions. In QED, interactions among electrically charged particles are due to the exchange of quanta of the electromagnetic field called photons (γ). The fact that γ is massless accounts for the long range of EF. The SF, quantum chromodynamics or QCD, is mediated by the exchange of massless gluons (g) between quarks that carry a quantum number called *color*. In contrast to the electrically neutral photon, gluons posses color charge and hence couple to one another. As a consequence, the color force between two colored particles increases in strength with increased distance. Thus quarks and gluons cannot appear as free particles, but exist only inside composite particles, called hadrons, with no net color charge. Nucleons are composed of three quarks of different colors, resulting in a 'white' color neutral state. Mesons contains quark and antiquark pairs whose color charges cancel. Since a gluon inside a nucleon cannot escape its boundaries, the nuclear force is mediated by color-neutral bound states, accounting for its short range, characterized by the Compton wavelength of the lightest of these: the π-meson.

The even shorter range of the WF is associated with the Compton wave-lengths of the charged W and neutral Z bosons that mediate it. Their couplings to the weak charges of quarks and leptons are comparable in strength to the electromagnetic coupling. When the weak interaction is measured over distances much larger than its range, its effects are averaged over the measurement area and hence suppressed in amplitude by a factor

$(E/M_{W,Z})^2 \approx (E/100GeV)^2$, where E is the characteristic energy transfer in the measurement. Because the W particles carry electric charge they must couple to the γ, implying a gauge theory that unites the weak and electromagnetic interactions, similar to QCD in that the gauge particles are self coupled. In distinction to γ's and gluons, W couple only to left-handed fermions (with spin oriented opposite to the direction of motion).

The SM is further characterized by a high degree of symmetry. For example, one cannot perform an experiment that would distinguish the color of the quarks involved. If the symmetries of the SM coupling were fully respected in nature, we could not distinguish an electron from a neutrino or a proton from a neutron; their detectable differences are attributed to 'spontaneous' breaking of the symmetry. Just as the spherical symmetry of the Earth is broken to a cylindrical symmetry by the earth's magnetic field, a field permeating all space, called the Higgs field, is invoked to explain the observation that the symmetries of electroweak theory are broken into the residual gauge symmetry of QED. Particles that interact with the Higgs field cannot propagate at the speed of light, and acquire masses. Particles that do not interact with the Higgs field - the photon, gluons remain massless. Fermions couplings to the Higgs field not only to determine their masses; they induce a misalignment of quark mass eigenstates with the eigenstates of the weak charges, thereby allowing all fermions of heavy families to decay to lighter ones. These couplings provide the only mechanism within the SM that can account for the observed violation of CP, i.e., invariance of the laws of nature under mirror reflection (parity P) and interchange of particles with their antiparticles (charge conjugation C).

The origin of the Higgs field has not yet been determined. However our very understanding of the SM implies that physics associated electroweak symmetry breaking (ESB) must become manifest at energies of present at Tevatron or at LHC. There is a strong reason stemming from quantum instability of scalar masses, to believe that physics will point to modification of the theory. Experiments probing higher energies and shorter distances may reveal clues connecting SM physics to gravity, and may shed light on other question unanswered. Concerning to the Higgs discovery. By the time of the writing of this the-

sis, the DØ and CDF Collaborations have reported some limits to the Higgs mass to be $165 - 175\,\mathrm{GeV}/c^2$ [6].

1.2 CP Violation

Symmetries and their conservation laws form, together with the elementary particles and their interactions, the basis of the fundamental physical description of nature. Until approximatively 1956 it was assumed that the laws of physics remain unchanged when one changes the sign of spatial coordinates in a given system. This mirroring is called the *parity operation P*. However, it was observed that the mirror image of the left-handed neutrino, the right-handed neutrino, does not exist and that therefore the symmetry of the weak interaction is broken by the P operation. The symmetry is restored when the P operator is not applied alone, but when the combined operation CP is applied. C (charge conjugation) is the operation that transforms a particle into its antiparticle. CP-transformation transforms a left-handed neutrino into a right-handed antineutrino, which does exist.

CP violation was first observed in 1964 in the decay of neutral kaons. Since then accurate measurements have taken place to determine the origin of CP violation in the K-meson system. However, with the K-meson effects due to the strong interaction are too large to draw any conclusion about the origin of CP violation. The expectation is that these effects will be less and better to determine in the case of a heavier meson such as the B meson. For a complete reference on the current measurements see Ref. [7]

The question is now simply why the universe exists out of matter and not out of antimatter. (Experimentally we are sure that less than 0.01% of the universe consists out of antimatter). Indeed, in all reactions that we know of where a quark is produced, an antiquark is also produced. By to date, there are some signs of the CP violoation in the B_s^0 system, but not with a strong conclusion about it [8].

1.3 CKM Matrix

In the SM the quark eigenstates are not the same as the weak eigenstates, and the matrix relating these bases was defined for six quarks, and giving an explicit parametrization by Kobayashi and Maskawa [9] in 1973 . This generalizes the four-quark case, where the matrix is described by a single parameter, the Cabibbo angle [10]. By convention, the mixing is often expressed in terms of a 3×3 unitary matrix V operation on the charge $-e/3$ quark mass eigenstates (d, s and b):

$$\begin{pmatrix} d' \\ s' \\ b' \end{pmatrix} = \begin{pmatrix} V_{ud} & V_{us} & V_{ub} \\ V_{cd} & V_{cs} & V_{cb} \\ V_{td} & V_{ts} & V_{tb} \end{pmatrix} \begin{pmatrix} d \\ s \\ b \end{pmatrix} \tag{1.1}$$

There are several parameterizations of the Cabibbo-Kobayashi-Maskawa (CKM) matrix. We advocate a standard parametrization [11] of V that uses angles $\theta_{12}, \theta_{23}, \theta_{13}$ and a phase δ_{13}

$$V = \begin{pmatrix} c_{12}c_{13} & s_{12}c_{13} & s_{13}e^{-i\delta_{13}} \\ -s_{12}c_{23} - c_{12}s_{23}s_{13}e^{i\delta_{13}} & c_{12}c_{23} - s_{12}s_{23}s_{13}e^{i\delta_{13}} & s_{23}c_{13} \\ s_{12}s_{23} - c_{12}s_{23}s_{13}e^{i\delta_{13}} & -c_{12}s_{23} - s_{12}s_{23}s_{13}e^{i\delta_{13}} & c_{23}c_{13} \end{pmatrix} \tag{1.2}$$

with $c_{ij} = cos\theta_{ij}$ and $s_{ij} = sin\theta_{ij}$ for the "generation" labels $i, j = 1, 2, 3$. The matrix elements in the first and third row, which have been directly measured in decay processes, are all of a simple form, and c_{13} is know to deviate from unity in the sixth decimal place, $V_{ud} = c_{12}$, $V_{us} = s_{12}$, $V_{ub} = s_{13}e^{-i\delta_{13}}$, $V_{cb} = s_{23}$ and $V_{tb} = c_{23}$ to an excellent approximation. The phase δ_{13} lies in the $0 \leq \delta_{13} < 2\pi$, with non-zero values generally breaking CP invariance for the weak interactions.

The standard parametrization can be approximated in a way that emphasizes the hierarchy in the size of the angles, $s_{12} \gg s_{23} \gg s_{13}$ [12], known as Wolfeinstein parametrization. Setting $\lambda \equiv s_{12}$, the sine of the Cabibbo angle, one express the other elements in the terms of powers of λ:

$$V = \begin{pmatrix} 1-\lambda^2/2 & \lambda & A\lambda^3(\rho - i\eta) \\ -\lambda & 1-\lambda^2/2 & A\lambda^2 \\ A\lambda^3(1-\rho-i\eta) & A\lambda^2 & 1 \end{pmatrix} + O(\lambda^4) \tag{1.3}$$

with A, ρ and η real numbers that were intended to be of the order of the unity. This form is widely used, especially for B physics, but care must be taken, especially for CP-violating effects in K physics, since the phase enter V_{cd} and V_{cs} terms are higher order in λ. The unitarity of the CKM matrix could be corroborated experimentally and hence give us physics beyond SM.

Direct and indirect information on the smallest matrix elements of the CKM matrix is neatly summarized in terms of the unitary triangle, one of six such triangles that correspond to the unitarity condition applied to two different rows or columns of the CKM matrix. Unitarity applied to the first and third column yields $V_{ud}V_{ub}^* + V_{cd}V_{cb}^* + V_{td}V_{tb}^* = 0$.

The unitarity triangle is just a geometrical presentation of this equation in the complex plane, as in Figure 1.2 (a). We can always choose to orient the triangle so that $V_{cd}V_{cd}^*$ lies along the horizontal; in the standard parametrization, V_{cb} is real and V_{cd} is real to a very good approximation in any case. The angles α, β and γ of the triangle are also referred to as ϕ_2, ϕ_1 and ϕ_3 respectively with β and γ being the phases of the CKM elements V_{td} and V_{ub} given by

$$V_{td}^* = |V_{td}|e^{-i\beta}, V_{ub} = |V_{ub}|e^{-i\gamma} \tag{1.4}$$

Rescaling the triangle so that the base is of unit length, the coordinates of the vertices A, B, and C becomes respectively:

$$\left(\frac{\mathrm{Re}\,(V_{ud}V_{ub}^*)}{|V_{cd}V_{cb}^*|}, \frac{\mathrm{Im}\,(V_{ud}V_{ub}^*)}{|V_{cd}V_{cb}*|}\right), (1,0)\,\mathrm{and}\,(0,0). \tag{1.5}$$

The coordinates of the apex of the rescaled unitarity triangle take the simple form $(\bar{\rho}, \bar{\eta})$ with $\bar{\rho} = \rho(1-\lambda^2/2)$ and $\bar{\eta} = \eta(1-\lambda^2/2)$ in the Wolfeinstein parametrization as shown in

Figure 1.2 (b).

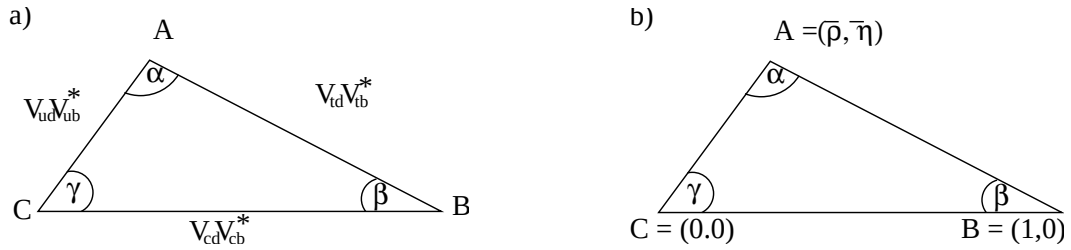

Figure 1.2: (a) Representation in the complex plane of the triangle formed by the CKM matrix elements $V_{ud}V_{ub}^*, V_{td}V_{tb}^*$, and $V_{cd}V_{cb}^*$. (b) Rescaled triangle with vertices A,B, and C at $(\bar{\rho}, \bar{\eta}), (1, 0)$ and $(0, 0)$ respectively.

1.4 B Mixing

In this section we list the necessary formulas to describe $B_d^0 - \bar{B}_d^0$ and $B_s^0 - \bar{B}_s^0$. The formulas are general and apply to both B_d^0 and to B_s^0 mesons, although with different values of the parameters. In the SM $B_d^0 - \bar{B}_d^0$ is caused by the fourth order flavor-changing weak interaction described by the box diagrams in Fig. 1.3, and similarly for $B_s^0 - \bar{B}_s^0$, represented in Fig. 1.1. Such transitions are called $|\delta B = 2|$ transitions, because they change the bottom quantum

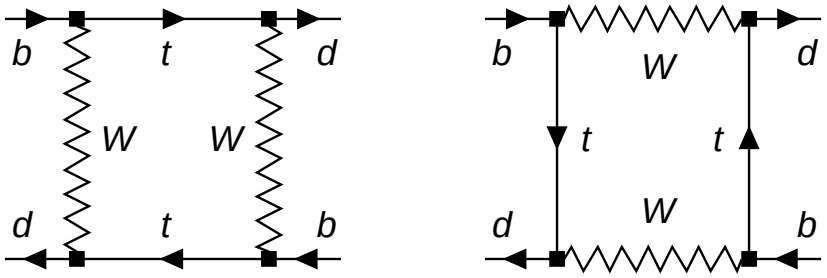

Figure 1.3: Standard Model box diagrams inducing $B_d^0 - \bar{B}_d^0$ mixing.

number by two units.

$B_d^0 - \bar{B}_d^0$ induces oscillations between B_d^0 and $\bar{B}_d^0$. An initially produced B^0 or $\bar{B}^0$ evolves in time into a superposition of B^0 and $\bar{B}^0$. Let $|B^0(t)\rangle$ denote the state vector of a B meson which is tagged as a B^0 at time $t = 0$, i.e., $|B^0(t = 0)\rangle = |B^0\rangle$. Likewise $|\bar{B}^0(t)\rangle$ represents a B meson initially tagged as a $\bar{B}^0$. The time evolution of these states is governed by a

Schrödinger equation:

$$i\,\frac{d}{dt}\begin{pmatrix}\delta_s|B(t)\rangle\\ \delta_s|\bar{B}(t)\rangle\end{pmatrix}=\left(M-i\,\frac{\Gamma}{2}\right)\begin{pmatrix}\delta_s|B(t)\rangle\\ \delta_s|\bar{B}(t)\rangle\end{pmatrix}. \tag{1.6}$$

where the *mass matrix* M and the *decay matrix* Γ are t-independent, Hermitian 2×2 matrices. *CPT* invariance implies that

$$M_{11}=M_{22}\,,\qquad\qquad \Gamma_{11}=\Gamma_{22}\,. \tag{1.7}$$

$|\Delta B|=2$ transitions induce non-zero off-diagonal elements in (1.6), so that the mass eigenstates of the neutral B meson are different from the flavor eigenstates $|B^0\rangle$ and $|\bar{B}^0\rangle$. The mass eigenstates are defined as the eigenvectors of $M-i\,\Gamma/2$. We express them in terms of the flavor eigenstates as

$$\begin{aligned}\text{Lighter eigenstate:}\quad |B_L\rangle &= p|B^0\rangle+q|\bar{B}^0\rangle\\ \text{Heavier eigenstate:}\quad |B_H\rangle &= p|B^0\rangle-q|\bar{B}^0\rangle\end{aligned} \tag{1.8}$$

with $|p|^2+|q|^2=1$. Note that, in general, $|B_L\rangle$ and $|B_H\rangle$ are not orthogonal to each other.

The time evolution of the mass eigenstates is governed by the two eigenvalues $M_H-i\Gamma_H/2$ and $M_L-i\Gamma_L/2$:

$$|B_{H,L}(t)\rangle=e^{-(iM_{H,L}+\Gamma_{H,L}/2)t}\,|B_{H,L}\rangle\,, \tag{1.9}$$

where $|B_{H,L}\rangle=|B_{H,L}(t=0)\rangle$ and

$$\Gamma_{L,H}=\frac{1}{\tau_{L,H}} \tag{1.10}$$

is the inverse of the lifetime for the light (L) and heavy (H) mass eigenstates. We adopt the following definitions for the average mass and width and the mass and width differences of the B meson eigenstates:

$$m \;=\; \frac{M_H+M_L}{2}=M_{11} \tag{1.11}$$

$$\Gamma = \frac{\Gamma_L + \Gamma_H}{2} = \Gamma_{11} \tag{1.12}$$

$$\Delta m = M_H - M_L \tag{1.13}$$

$$\Delta\Gamma = \Gamma_L - \Gamma_H \tag{1.14}$$

where Δm is positive by definition. In our convention the SM prediction for $\Delta\Gamma$ is positive. In the case of the B_d^0, the decay width difference $\Delta\Gamma_d$ is expected to be consistent with zero; but for the B_s^0, it is expected that $\Delta\Gamma_s$ be sizeable [3, 5]. We can find the time evolution of $|B(t)\rangle$ and $|\bar{B}(t)\rangle$ as follows. We first invert (1.8) to express $|B^0\rangle$ and $|\bar{B}^0\rangle$ in terms of the mass eigenstates and using their time evolution in (1.9):

$$\begin{aligned} |B^0(t)\rangle &= \frac{1}{2p}\left[\, e^{-iM_L t-\Gamma_L t/2}\,|B_L\rangle \,+\, e^{-iM_H t-\Gamma_H t/2}\,|B_H\rangle\,\right], \\ |\bar{B}^0(t)\rangle &= \frac{1}{2q}\left[\, e^{-iM_L t-\Gamma_L t/2}\,|B_L\rangle \,-\, e^{-iM_H t-\Gamma_H t/2}\,|B_H\rangle\,\right]. \end{aligned} \tag{1.15}$$

These expressions will be very useful in the discussion of B_s mixing. With (1.8) we next eliminate the mass eigenstates in (1.15) to obtain:

$$\begin{aligned} |B^0(t)\rangle &= \quad g_+(t)\,|B^0\rangle + \frac{q}{p}\,g_-(t)\,|\bar{B}^0\rangle\,, \\ |\bar{B}^0(t)\rangle &= \frac{p}{q}\,g_-(t)\,|B^0\rangle + \quad g_+(t)\,|\bar{B}^0\rangle\,, \end{aligned} \tag{1.16}$$

where

$$\begin{aligned} g_+(t) &= e^{-imt}\,e^{-\Gamma t/2}\left[\quad \cosh\frac{\Delta\Gamma\, t}{4}\,\cos\frac{\Delta m\, t}{2} - i\sinh\frac{\Delta\Gamma\, t}{4}\,\sin\frac{\Delta m\, t}{2}\,\right], \\ g_-(t) &= e^{-imt}\,e^{-\Gamma t/2}\left[-\sinh\frac{\Delta\Gamma\, t}{4}\,\cos\frac{\Delta m\, t}{2} + i\cosh\frac{\Delta\Gamma\, t}{4}\,\sin\frac{\Delta m\, t}{2}\,\right]. \end{aligned} \tag{1.17}$$

Note that, giving to $\Delta\Gamma \neq 0$, the coefficient $g_+(t)$ has no zeros, and $g_-(t)$ vanishes only at $t = 0$. Hence an initially produced B_d^0 will never turn into a pure $\bar{B}_d^0$ or back into a pure B^0. The coefficients in (1.17) will enter the formulae for the decay asymmetries in the

combinations

$$\begin{aligned} |g_\pm(t)|^2 &= \frac{e^{-\Gamma t}}{2}\left[\cosh\frac{\Delta\Gamma\, t}{2} \pm \cos\left(\Delta m\, t\right)\right], \\ g_+^*(t)\, g_-(t) &= \frac{e^{-\Gamma t}}{2}\left[-\sinh\frac{\Delta\Gamma\, t}{2} + i\sin\left(\Delta m\, t\right)\right]. \end{aligned} \tag{1.18}$$

In the Standard Model, one can calculate the off-diagonal elements M_{12} and Γ_{12} entering (1.6) from $|\Delta B| = 2$ diagrams. In order to exploit the formulae (1.15)–(1.17) for the time evolution we still need to express Δm, $\Delta\Gamma$ and q/p in terms of M_{12} and Γ_{12}. By solving for the eigenvalues and eigenvectors of $M - i\Gamma/2$ one finds

$$(\Delta m)^2 - \frac{1}{4}(\Delta\Gamma)^2 = 4\,|M_{12}|^2 - |\Gamma_{12}|^2\,, \tag{1.19}$$

$$\Delta m\,\Delta\Gamma = -4\ \mathrm{Re}\left(M_{12}\Gamma_{12}^*\right), \tag{1.20}$$

$$\frac{q}{p} = -\frac{\Delta m + i\Delta\Gamma/2}{2M_{12} - i\Gamma_{12}} = -\frac{2M_{12}^* - i\Gamma_{12}^*}{\Delta m + i\Delta\Gamma/2}\,. \tag{1.21}$$

The relative phase between M_{12} and Γ_{12} appears in many observables related to B mixing. We introduce

$$\phi = \arg\left(-\frac{M_{12}}{\Gamma_{12}}\right). \tag{1.22}$$

Now one can solve (1.21) for Δm and $\Delta\Gamma$ in terms of $|M_{12}|$, $|\Gamma_{12}|$ and ϕ.

The general solution is not illuminating, but a simple, approximate solution may be derived when

$$|\Gamma_{12}| \ll |M_{12}| \qquad \text{and} \qquad \Delta\Gamma \ll \Delta m \tag{1.23}$$

These inequalities hold (empirically) for both B_d^0 systems. We first note that $|\Gamma_{12}| \le \Gamma$ always, because Γ_{12} stems from the decays into final states common to B_d^0 and $\bar{B}_d^0$. For the B_s^0 meson the lower bound on Δm_s establishes experimentally that $\Gamma_{B_s} \ll \Delta m_s$. Hence $\Gamma_{12}^s \ll \Delta m_s$, and Eqs. (1.19) and (1.20) imply $\Delta m_s \approx 2|M_{12}^s|$ and $|\Delta\Gamma_s| \le 2|\Gamma_{12}^s|$, so that 1.23 holds. For the B_d^0 meson the experiments give $\Delta m_d \approx 0.75\Gamma_{B_d^0}$. The Standard Model predicts $|\Gamma_{12}^d|/\Gamma_{B_d^0} = \mathcal{O}(1\%)$, but Γ_{12}^d stems solely from CKM-suppressed decay channels (common

to B_d^0 and $\bar{B}_d^0$) and could therefore be affected by new physics. New decay channels would, however, also increase $\Gamma_{B_d^0}$ and potentially conflict with the precisely measured semileptonic branching ratio. A conservative estimate is $|\Gamma_{12}^d|/\Gamma_{B_d^0} < 10\%$. Hence for both the B_s^0 and B_d^0 system an expansion in Γ_{12}/M_{12} and $\Delta\Gamma/\Delta m$ is a good approximation, and we easily find

$$\Delta m = 2|M_{12}| \left[1 + \mathcal{O}\left(\left|\frac{\Gamma_{12}}{M_{12}}\right|^2\right)\right], \tag{1.24}$$

$$\Delta\Gamma = 2|\Gamma_{12}| \cos\phi \left[1 + \mathcal{O}\left(\left|\frac{\Gamma_{12}}{M_{12}}\right|^2\right)\right]. \tag{1.25}$$

1.5 B lifetimes

In the spectator model, a heavy quark in a hadron is bound to the lighter spectator quark. For as long as the spectator holds, the decay is governed by the weak decay of the heavy quark Q, and, for this reason, the lifetime of all hadrons containing Q are the same and equal to that of a free Q. However lifetimes of B hadrons have been experimentally observed to follow a hierarchy scheme

$$\tau_{B_c} < \tau_{barion} < \bar{\tau}_s \leq \tau_d < \tau_{B_u} \tag{1.26}$$

We are interested in measuring the ratio $\bar{\tau}_s/\tau_d$, where

$$\bar{\tau}_s \equiv \frac{\tau_L + \tau_H}{2} \tag{1.27}$$

is the mean lifetime for the B_s^0 and τ_d is the lifetime for the B_d^0.

1.6 Heavy Quark Effective theory

A very successful theory to describe the decay of the meson containing a heavy and a light quark is the Heavy Quark Effective Theory (HQET), a more detailed treatment is in Ref. [3, 5], where a heavy quark is defined by $m_Q >> \lambda_{QCD}$ with λ_{QCD} $0.2GeV$. In the

HQET the Lagrangian is expressed in an expansion in powers of $1/m_Q$, usually referred to as the Operator Product Expansion (OPE). In practice only the b and c quarks have masses large enough that HQET is valid. It it does not apply to the top quark because it decays before hadronization.

The lifetime ratio of the B_s/B^0 has been calculated using OPE to be:

$$\frac{B_s}{B^0} = 1.00 \pm 0.01 \tag{1.28}$$

In conclusion lifetime ratios are predicted by theory very precisely hence can give us a powerful tool to test the Standard Model. We will compare our measurement for the lifetime ratio $\bar{\tau}_s/\tau_d$.

1.7 Time-dependent angular analysis for the B_d^0 and B_s^0 mesons

Once we have established some definitions related with mixing for the two mesons under study in this dissertation, we will show now their relation with the description of the flavor-untagged decays $B_d^0 \to J/\psi K^{*0}$ and $B_s^0 \to J/\psi\phi$.

Both neutral B decays considered in this dissertation are decays of a pseudo-scalar to a vector-vector intermediate state. In such decays one can statistically distinguish those of different parity by looking at the angular correlations among the final state particles. Furthermore, both decays have the same four-vertex track topology, as shown in Fig. 1.4. The $p\bar{p}$ collisions take place in the primary vertex. When a B_d^0 or a B_s^0 is produced, it travels a distance $|\boldsymbol{L}_{xy}|$ until it decays in the secondary vertex. This vertex is called a four-track vertex. In the case of the $B_d^0(B_s^0)$, we have a kaon and a pion (kaon), which both come from the $K^{*0}(\phi)$. The muons account for the J/ψ. The fact that the topology is the same for both decays, lead us to the possibility to describe them in a very similar way. Now, we will establish the angular distributions for both decays.

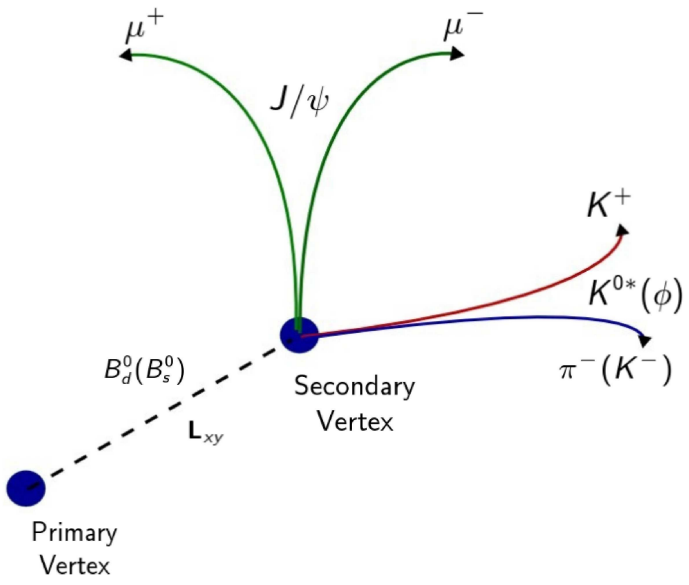

Figure 1.4: Four-vertex topology for the decays $B_d^0 \to J/\psi K^{*0}$ and $B_s^0 \to J/\psi\phi$.

1.7.1 The transversity basis and the transversity variables

The basis where we will describe the flavor-untagged decays $B_d^0 \to J/\psi K^{*0}$ and $B_s^0 \to J/\psi\phi$ is the transversity basis. It is defined as follows [13]: Consider the decay chain $B_d^0 \to J/\psi K^{*0} \to \mu^+\mu^- K^+\pi^-$. The transversity basis is fixed in the rest frame of the J/ψ. The K^{*0} flight direction defines the positive x axis, while the plane of $K^+\pi^-$ system defines the $x-y$ plane with the y axis oriented such that $p_y(K^+) > 0$. The two-fold ambiguity in choosing the z axis is solved by adopting a right-handed coordinate system. The angle θ is defined as the angle between μ^+ flight direction and the positive direction of the z axis. Angle φ is the angle between the x-axis and the projection of the μ^+ direction onto the $x-y$ plane. Finally, the ψ angle is the angle of the K^+ relative to the negative direction of the J/ψ in the K^{*0} rest frame. The angles are represented in Fig. 1.5. We will denote these three angles by $\boldsymbol{\omega} = \{\varphi, \cos\theta, \cos\psi\}$.

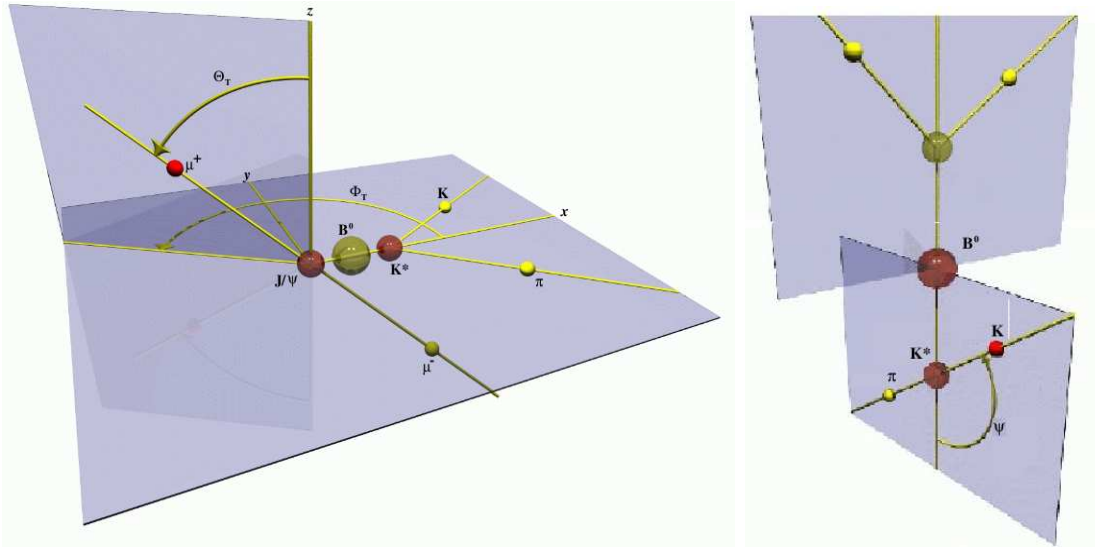

Figure 1.5: Transversity basis and angle definitions for the case $B_d^0 \to J/\psi K^{*0}$ decay. In the left, it is the schematic representation of the angles φ and θ; in the right, the angle ψ. Due to the same four-vertex track topology for both mesons, the translation to the $B_s^0 \to J/\psi\phi$ is straightforward just by interchange $\phi \to K^{*0}$ and $\pi \to K$

1.7.2 Time-dependent angular distributions for the decays $B_d^0 \to J/\psi K^{*0}$ and $B_s^0 \to J/\psi\phi$

In the description of the decays under study in this thesis in the transversity basis, the corresponding decay amplitudes for the decays take the form [13]

$$A(B_q(t) \to V_1V_2) = \frac{A_0(t)}{x}\varepsilon_{V_1}^{*L}\cdot\varepsilon_{V_2}^{*L} - \frac{A_\parallel(t)}{\sqrt{2}}\varepsilon_{V_1}^{*T}\cdot\varepsilon_{V_2}^{*T} - i\frac{A_\perp(t)}{\sqrt{2}}\varepsilon_{V_1}\times\varepsilon_{V_2}\cdot\hat{\boldsymbol{p}}_{V_2} \tag{1.29}$$

where $x \equiv p_{V_1}p_{V_2}/(m_{V_1}m_{V_2})$, $p_{V_{1(2)}}$ and $m_{V_{1(2)}}$ are the momentum and the mass of the vector meson 1 (2), and the symbols ε denote the polarization vectors of the final-state vector mesons V_1 and V_2. The factors A_α, with $\alpha = 0, \parallel, \perp$, in Eq.(1.29) are the linear polarization amplitudes of the vector mesons $(J/\psi, K^{*0}/\phi)$, which are either longitudinal (A_0), or transverse to their flight direction and parallel $(A_\parallel)$ or perpendicular $(A_\perp)$ to one another. Here the time dependences originate from $B_q - \bar{B}_q$ mixing, explained in section 1.4.

Only the relative phases of the amplitudes can enter as physics observables, so we are free to fix one of the phases. We choose to fix $\arg(A_0(0)) \equiv 0$ and define the phases

$\delta_\parallel \equiv \arg\ (A_\parallel(0))$ and $\delta_\perp \equiv \arg(A_\perp(0))$, where $A_i(0), i = \{0, \parallel, \perp\}$ are the linear polarization amplitudes at $t = 0$. Other condition is that the sum of the squares of the amplitudes should be the unit, i.e., $|A_0(0)|^2 + |A_\parallel(0)|^2 + |A_\perp(0)|^2 = 1$. This condition is related with the fact that we will need a normalized distribution. Unless it is explicity stated, throughout this thesis, we will denote $A_i(0) \equiv A_i$.

The flavor-untagged $B_s^0 \to J/\psi\phi$ decay

We will begin the description of the time-dependent angular distributions for the decays under study with the $B_s^0 - \bar{B}_s^0$ system.

In the case of the $B_s^0 \to J/\psi(\to \mu^+\mu^-)\phi(\to K^+K^-)$, the three-angle distribution for the decay of an initially present (i.e. tagged) B_s^0 meson takes the form [13]

$$\begin{aligned}\frac{d^4\mathcal{P}'}{d\boldsymbol{\omega}\, dt} &= |A_0(t)|^2 f_1(\boldsymbol{\omega}) + |A_\parallel(t)|^2 f_2(\boldsymbol{\omega}) + |A_\perp(t)|^2 f_3(\boldsymbol{\omega}) \\ &- \mathrm{Im}\left(A_\parallel^*(t)A_\perp(t)\right) f_4(\boldsymbol{\omega}) + \mathrm{Re}\left(A_0^*(t)A_\parallel(t)\right) f_5(\boldsymbol{\omega}) \\ &+ \mathrm{Im}\left(A_0^*(t)A_\perp(t)\right) f_6(\boldsymbol{\omega}) \end{aligned} \tag{1.30}$$

Now when an initially present $\bar{B}_s$ meson, the angular distribution is given by

$$\begin{aligned}\frac{d\bar{\mathcal{P}}}{d\boldsymbol{\omega}\, dt} &= |\bar{A}_0(t)|^2 f_1(\boldsymbol{\omega}) + |\bar{A}_\parallel(t)|^2 f_2(\boldsymbol{\omega}) + |\bar{A}_\perp(t)|^2 f_3(\boldsymbol{\omega}) \\ &- \mathrm{Im}\left(\bar{A}_\parallel^*(t)\bar{A}_\perp(t)\right) f_4(\boldsymbol{\omega}) + \mathrm{Re}\left(\bar{A}_0^*(t)\bar{A}_\parallel(t)\right) f_5(\boldsymbol{\omega}) \\ &+ \mathrm{Im}\left(\bar{A}_0^*(t)\bar{A}_\perp(t)\right) f_6(\boldsymbol{\omega}) \end{aligned} \tag{1.31}$$

where in both cases, the functions $f_i(\boldsymbol{\omega})$ are as follows:

$$f_1(\boldsymbol{\omega}) = \frac{9}{32\pi} 2\cos^2\psi(1 - \sin^2\theta\cos^2\varphi) \tag{1.32}$$

$$f_2(\boldsymbol{\omega}) = \frac{9}{32\pi} \sin^2\psi(1 - \sin^2\theta\sin^2\varphi) \tag{1.33}$$

$$f_3(\boldsymbol{\omega}) = \frac{9}{32\pi} \sin^2\psi\sin^2\theta \tag{1.34}$$

$$f_4(\boldsymbol{\omega}) = \frac{9}{32\pi} \sin^2\psi\sin 2\theta\sin\varphi \tag{1.35}$$

$$f_5(\boldsymbol{\omega}) = \frac{9}{32\pi}\frac{1}{\sqrt{2}}\sin 2\psi \sin^2\theta \sin 2\varphi \quad (1.36)$$

$$f_6(\boldsymbol{\omega}) = \frac{9}{32\pi}\frac{1}{\sqrt{2}}\sin 2\psi \sin 2\theta \cos\varphi \quad (1.37)$$

The amplitudes $A_i(t)$ are given in the following way [14]:

$$|A_0(t)|^2 = |A_0|^2 e^{-\Gamma t}\left[\cosh\frac{\Delta\Gamma_s t}{2} - |\cos\phi_s|\sinh\frac{\Delta\Gamma_s t}{2} + \rho(\phi_s,\Delta m_s,t)\right] \quad (1.38)$$

$$|A_\parallel(t)|^2 = |A_0|^2 e^{-\Gamma t}\left[\cosh\frac{\Delta\Gamma_s t}{2} - |\cos\phi_s|\sinh\frac{\Delta\Gamma_s t}{2} + \rho(\phi_s,\Delta m_s,t)\right] \quad (1.39)$$

$$|A_\perp(t)|^2 = |A_\perp|^2 e^{-\Gamma t}\left[\cosh\frac{\Delta\Gamma_s t}{2} + |\cos\phi_s|\sinh\frac{\Delta\Gamma_s t}{2} - \rho(\phi_s,\Delta m_s,t)\right] \quad (1.40)$$

$$\begin{aligned}\mathrm{Re}\,(A_0^*(t)A_\parallel(t)) &= |A_0||A_\parallel|e^{-\Gamma t}\cos\delta_\parallel \\ &\times\left[\cosh\frac{\Delta\Gamma_s t}{2} - |\cos\phi_s|\sinh\frac{\Delta\Gamma_s t}{2} + \rho(\phi_s,\Delta m_s,t)\right]\end{aligned} \quad (1.41)$$

$$\begin{aligned}\mathrm{Im}\,(A_\parallel^*(t)A_\perp(t)) &= |A_\parallel||A_\perp|e^{-\Gamma t}\left[\sin(\delta_\perp-\delta_\parallel)\cos(\Delta m_s\, t)\right. \\ &\left. -\cos(\delta_\perp-\delta_\parallel)\cos\phi_s\sin(\Delta m_s\, t) - \varpi(\delta_\perp-\delta_\parallel,\Delta\Gamma_s,t)\right]\end{aligned} \quad (1.42)$$

$$\begin{aligned}\mathrm{Im}\,(A_0^*(t)A_\perp(t)) &= |A_0||A_\perp|e^{-\Gamma t}\left[\sin\delta_\perp\cos(\Delta m_s\, t) - \cos\delta_\perp\cos\phi_s\sin(\Delta m_s\, t)\right. \\ &\left. -\varpi(\delta_\perp,\Delta\Gamma_s,t)\right]\end{aligned} \quad (1.43)$$

where $\rho(\phi_s,\Delta m_s,t) = \sin\phi_s\sin(\Delta m_s\, t)$ and $\varpi(\mathrm{phase},\Delta\Gamma_s,t) = \cos(\mathrm{phase})\sinh(\Delta\Gamma_s t/2)$. On the other hand, the amplitudes $\bar{A}_i(t)$ are as follows:

$$|\bar{A}_0(t)|^2 = |A_0|^2 e^{-\Gamma t}\left[\cosh\frac{\Delta\Gamma_s t}{2} - |\cos\phi_s|\sinh\frac{\Delta\Gamma_s t}{2} - \rho(\phi_s,\Delta m_s,t)\right] \quad (1.44)$$

$$|\bar{A}_\parallel(t)|^2 = |A_0|^2 e^{-\Gamma t}\left[\cosh\frac{\Delta\Gamma_s t}{2} - |\cos\phi_s|\sinh\frac{\Delta\Gamma_s t}{2} - \rho(\phi_s,\Delta m_s,t)\right] \quad (1.45)$$

$$|\bar{A}_\perp(t)|^2 = |A_\perp|^2 e^{-\Gamma t}\left[\cosh\frac{\Delta\Gamma_s t}{2} + |\cos\phi_s|\sinh\frac{\Delta\Gamma_s t}{2} + \rho(\phi_s,\Delta m_s,t)\right] \quad (1.46)$$

$$\begin{aligned}\mathrm{Re}\,(\bar{A}_0^*(t)\bar{A}_\parallel(t)) &= |A_0||A_\parallel|e^{-\Gamma t}\cos\delta_\parallel \\ &\times\left[\cosh\frac{\Delta\Gamma_s t}{2} - |\cos\phi_s|\sinh\frac{\Delta\Gamma_s t}{2} - \rho(\phi_s,\Delta m_s,t)\right]\end{aligned} \quad (1.47)$$

$$\begin{aligned}\mathrm{Im}\,(\bar{A}_\parallel^*(t)\bar{A}_\perp(t)) &= |A_\parallel||A_\perp|e^{-\Gamma t}\left[-\sin(\delta_\perp-\delta_\parallel)\cos(\Delta m_s\, t)\right. \\ &\left. +\cos(\delta_\perp-\delta_\parallel)\cos\phi_s\sin(\Delta m_s\, t) - \varpi(\delta_\perp-\delta_\parallel,\Delta\Gamma_s,t)\right]\end{aligned} \quad (1.48)$$

$$\mathrm{Im}\,(\bar{A}_0^*(t)\bar{A}_\perp(t)) = |A_0||A_\perp|e^{-\Gamma t}\left[-\sin\delta_\perp\cos(\Delta m_s\, t) + \cos\delta_\perp\cos\phi_s\sin(\Delta m_s\, t)\right.$$

$$-\varpi(\delta_\perp, \Delta\Gamma_s, t)] \tag{1.49}$$

To obtain the *flavor-untagged distributions* for the $B_s^0 \to J/\psi\phi$ decay, we need to assume that there are the same number of B_s^0 and $\bar{B}_s^0$ mesons in the sample. With this in mind, we can substitute Eqs. (1.38)-(1.43) and (1.44)-(1.49) into Eqs.(1.30) and (1.31) respectively, and sum these two latter. This leads to the relation

$$\begin{aligned}
\frac{d^4\mathcal{P}}{d\boldsymbol{\omega}dt} &= |A_0|^2 \left(\beta_+ e^{-\Gamma_L t} + \beta_- e^{-\Gamma_H t}\right) f_1(\boldsymbol{\omega}) \\
&+ |A_\parallel|^2 \left(\beta_+ e^{-\Gamma_L t} + \beta_- e^{-\Gamma_H t}\right) f_2(\boldsymbol{\omega}) \\
&+ |A_\perp|^2 \left(\beta_- e^{-\Gamma_L t} + \beta_+ e^{-\Gamma_H t}\right) f_3(\boldsymbol{\omega}) \\
&- \frac{1}{2}|A_\parallel||A_\perp| \cos(\delta_\perp - \delta_\parallel) \sin\phi_s \left(e^{-\Gamma_L t} - e^{-\Gamma_H t}\right) f_4(\boldsymbol{\omega}) \\
&+ |A_0||A_\parallel| \cos\delta_\parallel \left(\beta_+ e^{-\Gamma_L t} + \beta_- e^{-\Gamma_H t}\right) f_5(\boldsymbol{\omega}) \\
&+ \frac{1}{2}|A_0||A_\perp| \cos\delta_\perp \sin\phi_s \left(e^{-\Gamma_L t} - e^{-\Gamma_H t}\right) f_6(\boldsymbol{\omega})
\end{aligned} \tag{1.50}$$

where we have used the definitions of Γ and $\Delta\Gamma$ (Eqs.(1.12) and (1.14) respectively), and

$$\beta_\pm = \frac{1}{2}(1 \pm \cos\phi_s) \tag{1.51}$$

where ϕ_s is the *CP-violating phase* for the B_s^0 system. Note that in Eq.(1.50) there are no more contributions from the mixing parameter Δm_s, and a flavor-untagged expression is now at hand.

We can factorize equation (1.50) in terms of $e^{-\Gamma_L t}$ and $e^{-\Gamma_H t}$ to obtain

$$\begin{aligned}
\frac{d^4\mathcal{P}}{d\boldsymbol{\omega}dt} &= e^{-\Gamma_L t}\Big\{\beta_+ \Big[|A_0|^2 f_1(\boldsymbol{\omega}) + |A_\parallel|^2 f_2(\boldsymbol{\omega}) + |A_0||A_\parallel| \cos\delta_\parallel f_5(\boldsymbol{\omega})\Big] + |A_\perp|^2 \beta_- f_3(\boldsymbol{\omega}) \\
&- \frac{1}{2}|A_\parallel||A_\perp| \cos(\delta_\perp - \delta_\parallel) \sin\phi_s f_4(\boldsymbol{\omega}) + \frac{1}{2}|A_0||A_\perp| \cos\delta_\perp \sin\phi_s f_6(\boldsymbol{\omega})\Big\} \\
&+ e^{-\Gamma_H t}\Big\{\beta_- \Big[|A_0|^2 f_1(\boldsymbol{\omega}) + |A_\parallel|^2 f_2(\boldsymbol{\omega}) + |A_0||A_\parallel| \cos\delta_\parallel f_5(\boldsymbol{\omega})\Big] + |A_\perp|^2 \beta_+ f_3(\boldsymbol{\omega}) \\
&+ \frac{1}{2}|A_\parallel||A_\perp| \cos(\delta_\perp - \delta_\parallel) \sin\phi_s f_4(\boldsymbol{\omega}) - \frac{1}{2}|A_0||A_\perp| \cos\delta_\perp \sin\phi_s f_6(\boldsymbol{\omega})\Big\}
\end{aligned} \tag{1.52}$$

Here we still have the contribution from the phase ϕ_s; however, according with the SM, CP-violation effects in the B_s^0 system are very small [3]. Since we are not interested in this dissertation to measure this parameter, without lost of generality, we can fix $\phi_s = 0$ in Eq.(1.52). By doing this, we will have that $\beta_+ = 1$ and $\beta_- = 0$, so Eq.(1.50) can be written as follows:

$$\frac{d^4\mathcal{P}}{d\boldsymbol{\omega}\, dt} = e^{-\Gamma_L t}\left[|A_0|^2 f_1(\boldsymbol{\omega}) + |A_\parallel|^2 f_2(\boldsymbol{\omega}) + |A_0||A_\parallel|\cos\delta_\parallel f_5(\boldsymbol{\omega})\right] + e^{-\Gamma_H t}|A_\perp|^2 f_3(\boldsymbol{\omega}) \quad (1.53)$$

We can rewrite Eq. (1.53) as follows:

$$\frac{d^4\mathcal{P}}{d\boldsymbol{\omega}\, dt} = e^{-\Gamma_L t}\sum_{i=1,2,5} k_i f_i(\boldsymbol{\omega}) + e^{-\Gamma_H t} k_3 f_3(\boldsymbol{\omega}) \quad (1.54)$$

where

$$\begin{aligned} k_1 &= |A_0|^2, \\ k_2 &= |A_\parallel|^2, \\ k_3 &= |A_\perp|^2, \\ k_5 &= |A_0||A_\parallel|\cos\delta_\parallel. \end{aligned}$$

Eq. (1.54) is the final flavor-untagged expression we were looking for and that which will be used to extract the values of the mean lifetime $\bar{\tau}_s$, the decay width difference $\Delta\Gamma_s$ (defined in Eqs. (1.27) and (1.14), respectively), the linear polarization amplitudes $|A_0|^2, |A_\parallel|^2$, and $|A_\perp|^2$, and the strong phase $\delta_\parallel$. Note that, in the absence of another term that involves the parameter $\delta_\parallel$, it has an ambiguity, since $\delta_\parallel \to -\delta_\parallel$ is also a solution for the Eq. (1.53).

The flavor-untagged decay $B_d^0 \to J/\psi K^{*0}$

Now we will find the equation to describe the flavor-untagged decay $B_d^0 \to J/\psi K^{*0}$. As we did for the B_s^0, we should take into account the B_d^0 and $\bar{B}_d^0$ decay modes into a J/ψ and a

K^{*0} and assume the same number of mesons and antimesons in our sample. However, we should mention before the interaction of the three partial waves: S-, P-, and D-waves.

The B meson is a particle with spin 0, and the vector mesons J/ψ and K^{*0} are particles with spin 1. So the relative angular moment, L, between the two vector mesons have the values $L = 0, 1, 2$. With this in mind, the $B_d^0 \to J/\psi K^{*0}$ decay can be write as a superposition[2] of the three partial waves S-wave (corresponding to $L = 0$), P-wave ($L = 1$), and D-wave ($L = 2$) [15]. In this dissertation, we will only consider the S- and P-waves and their interference.

By taking into account only the P-wave contribution for the decay mode $B_d^0 \to J/\psi (\to \mu^+\mu^-)K^{*0}(\to K^+\pi^-)$, and assuming that the decay width difference $\Delta\Gamma_d$ is small, as stated in section 1.4, the angular distribution is given by

$$\begin{aligned}\frac{d^4\mathcal{P}_1}{d\boldsymbol{\omega}\, dt} &= \cos^2\left(\frac{\Delta m_d\, t}{2}\right) e^{-\Gamma_d t}\Big[|A_0|^2 f_1(\boldsymbol{\omega}) + |A_\parallel|^2 f_2(\boldsymbol{\omega}) + |A_\perp|^2 f_3(\boldsymbol{\omega}) \\ &\quad -K^{sign}\,\mathrm{Im}\,(A_\parallel^* A_\perp) f_4(\boldsymbol{\omega}) + \mathrm{Re}\,(A_0^* A_\parallel) f_5(\boldsymbol{\omega}) + K^{sign}\,\mathrm{Im}\,(A_0^* A_\perp) f_6(\boldsymbol{\omega})\Big] \quad (1.55)\end{aligned}$$

and for the decay $\bar{B}_d^0 \to J/\psi(\to \mu^+\mu^-)K^{*0}(\to K^+\pi^-)$

$$\begin{aligned}\frac{d^4\mathcal{P}_2}{d\boldsymbol{\omega}\, dt} &= \sin^2\left(\frac{\Delta m_d\, t}{2}\right) e^{-\Gamma_d t}\Big[|A_0|^2 f_1(\boldsymbol{\omega}) + |A_\parallel|^2 f_2(\boldsymbol{\omega}) + |A_\perp|^2 f_3(\boldsymbol{\omega}) \\ &\quad -K^{sign}\,\mathrm{Im}\,(A_\parallel^* A_\perp) f_4(\boldsymbol{\omega}) + \mathrm{Re}\,(A_0^* A_\parallel) f_5(\boldsymbol{\omega}) + K^{sign}\,\mathrm{Im}\,(A_0^* A_\perp) f_6(\boldsymbol{\omega})\Big] \quad (1.56)\end{aligned}$$

where the K^{sign} is related with the sign of the kaon in the K^{*0} decay and $f_i(\boldsymbol{\omega})$ are the same as those of Eqs. (1.32)-(1.37).

The B_d^0 can also decay as $B_d^0 \to J/\psi(\to \mu^+\mu^-)\bar{K}^{*0}(\to K^-\pi^+)$ which lead us to a distribution

$$\begin{aligned}\frac{d^4\mathcal{P}_3}{d\boldsymbol{\omega}\, dt} &= \sin^2\left(\frac{\Delta m_d\, t}{2}\right) e^{-\Gamma_d t}\Big[|A_0|^2 f_1(\boldsymbol{\omega}) + |A_\parallel|^2 f_2(\boldsymbol{\omega}) + |A_\perp|^2 f_3(\boldsymbol{\omega}) \\ &\quad -K^{sign}\,\mathrm{Im}\,(A_\parallel^* A_\perp) f_4(\boldsymbol{\omega}) + \mathrm{Re}\,(A_0^* A_\parallel) f_5(\boldsymbol{\omega}) + K^{sign}\,\mathrm{Im}\,(A_0^* A_\perp) f_6(\boldsymbol{\omega})\Big] \quad (1.57)\end{aligned}$$

[2]Strictly speaking, we should also take into account this decomposition for the B_s^0 decay, since ϕ is also a vector meson; however, it was found that the contribution from the S-wave to this decay is negligible. See Appendix D

and the corresponding $\bar{B}^0_d \to J/\psi(\to \mu^+\mu^-)\bar{K}^{*0}(\to K^-\pi^+)$

$$\begin{aligned}\frac{d^4\mathcal{P}_4}{d\boldsymbol{\omega}\,dt} &= \cos^2\left(\frac{\Delta m_d\, t}{2}\right) e^{-\Gamma_d t}\Big[|A_0|^2 f_1(\boldsymbol{\omega}) + |A_\parallel|^2 f_2(\boldsymbol{\omega}) + |A_\perp|^2 f_3(\boldsymbol{\omega}) \\ &\quad -K^{sign}\,\mathrm{Im}\,(A^*_\parallel A_\perp) f_4(\boldsymbol{\omega}) + \mathrm{Re}\,(A^*_0 A_\parallel) f_5(\boldsymbol{\omega}) + K^{sign}\,\mathrm{Im}\,(A^*_0 A_\perp) f_6(\boldsymbol{\omega})\Big] \quad (1.58)\end{aligned}$$

To obtain the *flavor-untagged distribution* for the B^0_d meson we should sum over equations with the same K^{*0} meson, i.e., we need to sum Eqs. (1.55) and (1.56) or Eqs. (1.57) and (1.58). In any of the two cases, we will have then the problem of assign the correct mass to the kaon and the pion. In chapter 4 we will discuss how we solve this feature.

By taking into account only the P-wave contribution to the decay $B^0_d \to J/\psi K^{*0}$, the untagged distribution is given by

$$\begin{aligned}\frac{d^4\mathcal{P}}{d\boldsymbol{\omega}\,dt} \equiv \alpha_P &= e^{-\Gamma_d t}\Big[|A_0|^2 f_1(\boldsymbol{\omega}) + |A_\parallel|^2 f_2(\boldsymbol{\omega}) + |A_\perp|^2 f_3(\boldsymbol{\omega}) - K^{sign}\,\mathrm{Im}\,(A^*_\parallel A_\perp) f_4(\boldsymbol{\omega}) \\ &\quad + \mathrm{Re}\,(A^*_0 A_\parallel) f_5(\boldsymbol{\omega}) + K^{sign}\,\mathrm{Im}\,(A^*_0 A_\perp) f_6(\boldsymbol{\omega})\Big] \quad (1.59)\end{aligned}$$

Now, we should incorporate the contribution from the S-wave and its interference with the P-wave. From previous measurements [16], it is known that there exists a significant $K\pi$ S-wave contribution to this decay. To take this into account, we introduce an absolute amplitude $|A_s|$ and a relative phase δ_s for the S-wave component:

$$\begin{aligned}\alpha_{S+P} &= \cos^2\lambda\cdot\alpha_P + \sin^2\lambda\cdot f_7(\boldsymbol{\omega}) + \frac{1}{2}\sin 2\lambda\Big[f_8(\boldsymbol{\omega})\cos(\delta_\parallel - \delta_s)|A_\parallel| \quad (1.60)\\ &\quad + f_9(\boldsymbol{\omega})\sin(\delta_\perp - \delta_s)|A_\perp| + f_9(\boldsymbol{\omega})\cos\delta_s\cdot|A_0|\Big] \quad (1.61)\end{aligned}$$

where

$$\begin{aligned}f_7(\boldsymbol{\omega}) &= \frac{3}{32\pi}2\Big[1-\sin^2\theta\cos^2\varphi\Big] \quad (1.62)\\ f_8(\boldsymbol{\omega}) &= -\frac{3}{32\pi}\sqrt{6}\sin\psi\sin^2\theta\sin 2\varphi \quad (1.63)\\ f_9(\boldsymbol{\omega}) &= \frac{3}{32\pi}\sqrt{6}\sin\psi\sin 2\theta\cos\varphi \quad (1.64)\end{aligned}$$

$$f_{10}(\boldsymbol{\omega}) = \frac{3}{32\pi} 4\sqrt{3} \cos\psi \left[1 - \sin^2\theta \cos^2\varphi\right] \tag{1.65}$$

$$\cos\lambda = \frac{A_P}{\sqrt{A_P^2 + |A_2|^2}} \tag{1.66}$$

$$\sin\lambda = \frac{|A_S|}{\sqrt{A_P^2 + |A_2|^2}} \tag{1.67}$$

$$\tag{1.68}$$

with $0 \leq \lambda \leq \pi/2$. Note that, when $\lambda = 0$, the amplitude related with the S-wave vanishes and only the first term of Eq. (1.60) survives, leading to a contribution only by the P-wave. On the other hand, if $\lambda = \pi/2$, only the S-wave is present and the second term in Eq. (1.60) is different from zero.

We can rewrite Eq. (1.60) as follows

$$\alpha_{P+S} = e^{-\Gamma t} \sum_{i=1}^{10} g_i f_i(\boldsymbol{\omega}) \tag{1.69}$$

where

$$g_1 = |A_0|^2 \cos^2\lambda, \tag{1.70}$$

$$g_2 = |A_{||}|^2 \cos^2\lambda, \tag{1.71}$$

$$g_3 = |A_\perp|^2 \cos^2\lambda = \left(1 - |A_0|^2 + |A_\parallel|^2\right) \cos^2\lambda \tag{1.72}$$

$$g_4 = -K^{sign} |A_{||}||A_\perp| \sin(\delta_\perp - \delta_{||}) \cos^2\lambda \tag{1.73}$$

$$g_5 = |A_0||A_{||}| \cos\delta_{||} \cos^2\lambda \tag{1.74}$$

$$g_6 = K^{sign} |A_0||A_\perp| \sin\delta_\perp \cos^2\lambda \tag{1.75}$$

$$g_7 = \sin^2\lambda \tag{1.76}$$

$$g_8 = \frac{\sin 2\lambda}{2} \cos\left(\delta_\parallel - \delta_s\right) |A_\parallel| \tag{1.77}$$

$$g_9 = \frac{\sin 2\lambda}{2} \sin\left(\delta_\perp - \delta_s\right) |A_\perp| \tag{1.78}$$

$$g_{10} = \frac{\sin 2\lambda}{2} |A_0| \cos\delta_s \tag{1.79}$$

The usefulness of Eqs. (1.53) and (1.69) will be shown in chapter 4.

Once we have established the time-dependent angular relations for the flavor-untagged $B_d^0 \to J/\psi K^{*0}$ and $B_s^0 \to J/\psi\phi$ decays, we will now show a brief description of the factorization method and the flavor SU(3) symmetry. As mentioned above, the measurement of the angular parameters will give some conclusions about these two features of the SM.

1.8 Factorization

The hypothesis that the decay amplitude can be expressed as the product of two single current matrix elements is called factorization [17]. This hypothesis is taken by analogy to semileptonic decays where the amplitude can be decomposed into a leptonic and a hadronic current. Under this hypothesis, for the $B_d^0 \to J/\psi K^{*0}$ decay, both strong phases δ_1 and δ_2 defined above, should be $0\,(\mathrm{mod}\,\pi)$. It therefore predicts vanishing values of the observables

$$\mathrm{Im}\,[A_0^* A_\perp] = 0 \tag{1.80}$$

$$\mathrm{Im}\left[A_\parallel^* A_\perp\right] = 0 \tag{1.81}$$

and the equality

$$\mathrm{Re}\left[A_0^* A_\parallel\right] = \pm|A_0 A_\parallel| \tag{1.82}$$

The breakdown of the naive factorization assumption is unequivocally if *any* of the three Eqs.(1.80)-(1.82) is not satisfied. These interactions occur in a space-time region where the final-state particles have already been formed by the combined action of weak and strong forces but are still strongly interacting while recoiling from each other.

For the sake of comparison with theory [13], we will define two strong phases:

$$\delta_1 \equiv \arg(A_\parallel^* A_\perp) = \delta_\perp - \delta_\parallel \tag{1.83}$$

$$\delta_2 \equiv \arg(A_0^* A_\perp) = \delta_\perp \tag{1.84}$$

$$\tag{1.85}$$

These phases should be 0 (mod π) if factorization assumption holds for these decay [13].

There are other tests of the factorization hypothesis [17]. One of them is that it can be tested by comparing hadronic exclusive decays to the corresponding semileptonic mode. This is also known as the test with branching ratios. These tests can be performed for exclusive hadronic decays of either D or B mesons.

1.9 SU(3) symmetry for the $B_d^0 - B_s^0$ system

The B_d^0 meson can be formed by replacing the s quark with the d quark in the B_s^0 meson (see Fig. 1.6). For the $B_d^0 \to J/\psi K^{*0}$ decay, in the quark model representation of the mesons, this process is the sum of a tree and a penguin diagram [18] dressed with gluons in all possible places. It is the contribution of these soft gluons which we cannot calculate. Still the amplitude for this process is the sum of two complex numbers, one coming from the tree diagram and the other from the penguin diagram. The phase associated with each diagram has a weak and a strong contributions. The weak phases are due to the CKM matrix elements and they change sign in the CP conjugate process whereas the strong phases are due to hadronization and final state rescattering effects and they do are the same for both the original and the CP conjugate process. This is because CP violation does not occur in the strong interactions, but only in the weak sector. Since it is not easy to separate the contributions from the weak and strong phases to measure the CKM phases, flavor SU(3) symmetry can help to split these contributions, so that direct CP-violation (which comes from the interference of the tree and penguin diagrams) measurements in the B sector can in fact be used to extract the weak phases cleanly.

Whereas the use of the factorization assumption is somewhat not strongly supported for the channels $B_d^0 \to J/\psi K^{*0}$ and $B_s^0 \to J/\psi\phi$, flavor SU(3) symmetry is probably a good working assumption[13]. Following SU(3) [7], the nine possible $q_1\bar{q}_2$ combinations, where q_1 represents a quark and $\bar{q}_2$ an antiquark, containing the light u, d, and s quarks are grouped

into an octect and a singlet of light quark mesons:

$$\mathbf{3} \otimes \bar{\mathbf{3}} = \mathbf{8} \oplus \mathbf{1}$$

The decay of a $q\bar{q}$ meson into a pair of mesons involves the creation of a $q\bar{q}$ pair from the vacuum, and SU(3) symmetry assumes that the matrix elements for the creation of $s\bar{s}$, $u\bar{u}$, and $d\bar{d}$ pairs are equal. Thus all the hadronization dynamics of the $B_s^0 \to J/\psi\phi$, such as the strong phases δ_1 and δ_2, and the magnitudes of the linear polarization amplitudes $|A_0|$, $|A_\parallel|$, and $|A_\perp|$ can be obtained from the $B_d^0 \to J/\psi K^{*0}$ mode.

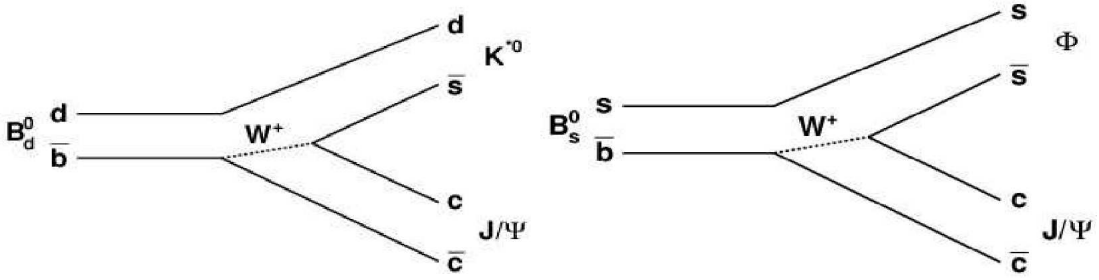

Figure 1.6: Feynman diagrams for the $B_d^0 \to J/\psi K^{*0}$ (left) and $B_s^0 \to J/\psi\phi$ (right) decays. Observe that if we replace the d quark by the s quark in the $B_d^0 \to J/\psi K^{*0}$ decay, we get the $B_s^0 \to J/\psi\phi$ decay.

The fact that the SU(3) symmetry holds for the $B_d^0 - B_s^0$ system is relevant in order to obtain information about the CP-violating phase ϕ_s: the measurements of the strong phases δ_1 and δ_2 for the B_s^0 meson can be done directly with the likelihood method (described later) or by *assuming* that the flavor SU(3) symmetry holds for these decays [19]. For this reason, it is very important a measurement that could be a solid test for flavor SU(3) symmetry which leads to an experimental basis for this phenomena.

However, S. Nandi and U. Nierste [20] argue that flavor SU(3) symmetry links $B_d^0 \to J/\psi K^{*0}$ only partially to $B_s^0 \to J/\psi\phi$. They argue that only the component of the ϕ meson with U-spin equal to 1 belongs to the symmetry multiplet of the K^{*0}. Furthermore, the decay amplitude into the equally large U-spin-zero component cannot be related to $B_d^0 \to J/\psi K^{*0}$. The results reported in this analysis possibly can clarify this argument.

By the date of writting the paper related with this dissertation, M. Gronau and J. L. Ros-

ner [21] state that the relation between the angular parameters for the $B_d^0 - B_s^0$ system are related by flavor U(3) symmetry rather than flavor SU(3) symmetry. For a detailed study of this statement, the reader is referred to [21]. In this thesis, we will work with the assumption that is the flavor SU(3) symmetry rather than the flavor U(3) symmetry the one that is applied to the $B_d^0 - B_s^0$ system under study.

In this chapter we have established a brief theoretical introduction on the topics that are related with the $B_d^0 \to J/\psi K^{*0}$ and $B_s^0 \to J/\psi\phi$ that we study on this dissertation. The structure of the thesis is as follows: in chapter 2 we will describe the most relevant systems of the DØ detector. In chapter 3 we describe the data selection and the Monte Carlo analysis. In chapter 4 we will describe the distribution models we will use to do the fits in order to extract the values of the relevant parameters of this dissertation. Finally, in chapter 5 we will report the measurements of the parameters involved in these analyses and the conclusions.

Chapter 2

Experimental Apparatus

The data used for this analysis was collected at the D0 detector, one of the collider detectors at the Tevatron at Fermi National Accelerator Laboratory in Batavia, Illinois, USA. In this chapter we briefly describe the experimental apparatus.

2.1 The Tevatron

The Tevatron is a collider of four miles in circumference and over one mile across that accelerates protons and anti-protons moving in the opposite directions, and collides them at the center-of-mass energy of $\sqrt{s} = 1.96$ TeV. The beam of protons or anti-protons is created as discrete bunches of particles that collide in the two experiments at the Tevatron: the CDF and DØ detectors. A schematic view is in Fig. 2.1. The collision points are surrounded by arrays of detecting devices that identify the nature of the particles emerging from the collision.

The proton beam originates from the preaccelerator, where negatively charged hydrogen ions are accelerated to 750 keV in a Cockroft-Walton accelerator. Then, the ions are passed through a direct current voltage ladder producing a voltage difference of 750 keV. From there, the hydrogen ions are bunched and led into a 130 meter long linear accelerator (LINAC) consisting of a series of drift tubes separated by vacuum gaps. Ions pass through the drift tubes where they are accelerated by the Radio Frequency (RF) cavities across the gap. The

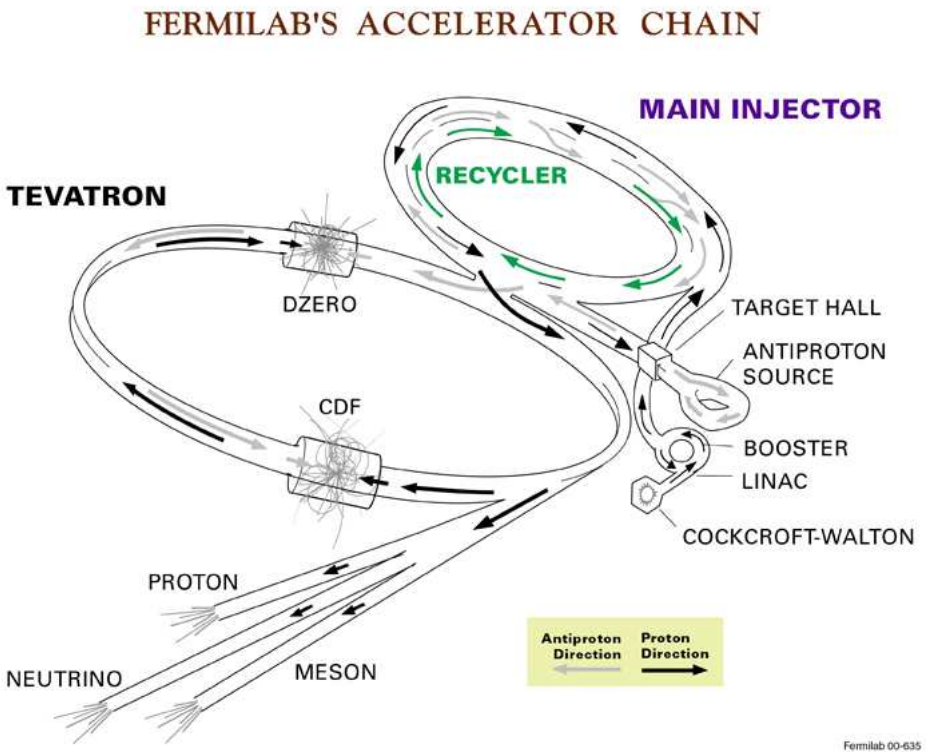

Figure 2.1: A Tevatron scheme. Not to scale.

RF source produces alternative electric field (with the frequency of 200 MHz in the beginning and 805 MHz towards the end) that lets the ions accelerate toward the next drift tube as long as the direction of the electric field is along the direction of the motion of the ions. As the ion's energy increases, the length of drift tubes and vacuum gaps increases to keep the velocity of the ion matching with the phase velocity of the electromagnetic wave. The alternating electric field concentrates the continuos ion beam into bunches, with a pulse length of 80 μs. After the ions are accelerated to 400 MeV, they are further passed through a carbon foil to strip the electrons off and leaving only the positevely charged protons. After this stage, the protons are injected into a synchroton, called booster, which is 472 m in circunference. The protons are accelerated using RF cavities to 8 GeV after circulating the booster withing 33 ms. After this stage, they enter the Main Injector (MI). This is a circular synchroton with 3319 m in circumference that accepts 8 GeV of protons from the booster. It raises the protons energy to 120 GeV, where they impinge upon the nickel target to produce the anti-protons and other short-lived particles. To produce 20 anti-protons with energy up

to 8 GeV it is required about one million of 120 GeV. The particles from the target are collimated using lithium lensing, and the magnets are used to transfer only the negatively charged anti-protons to the debuncher and eventually to the accumulator. The antiprotons from the target comes off with various energies, and the debuncher, consisting of RF, is used to equalize the energy of anti-protons before sending them to the accumulator. Anti-protons are stored in the accumulator ring until need. When approximately 10^{11} anti-protons have been produced, they are assembled, bunched and inserted in the MI to an energy of 150 GeV for injection in the Tevatron. The tunnel of the MI also holds the anti-proton recycler, which stores decelerated anti-protons coming from the previous run in the Tevatron for future use. After separate acceleration of the protons and anti-protons in the main injector to an energy of 150 GeV, both beams are inserted in the Tevatron, where they are further accelerated to an energy of 980 GeV.

The Tevatron uses superconducting magnets with a filed strength of 4.2 Tesla (at a beam energy of 980 GeV) to bend the protons and anti-protons through the 1000-meter radius tunnel. The proton beam traverses the Tevatron clockwise, while the antiproton beam moving in the opposite direction. The beams meet at the two interactions points, at the BØ, where the CDF detector is located, and at the DØ , where the DØ detector is located. The current parameters of the Tevatron are reported in Table 2.1.

2.2 The DØ detector

The DØ detector [22, 23] is about 18 m long, 10 m high and 12 m wide hermetic device that sourrounds the beam pipe, and detects the particle after the collision occurs at the center of the detector. The DØ experiment is a multipurpose detector consisting of three major subsystems: central tracking detectors, calorimeter, and a muon spectrometer. Tracking subdetectors provide a measure of the momentum charged particles near the center of the detector while large calorimeters force particles to shower and measure their energy. Outer layers flag and locally measure muon candidates that escape the rest of the detector. A

Parameter	value
Maximum beam energy (TeV)	0.980
Luminosity ($10^{30} cm^{-2} s^{-1}$)	286
Time between collision (ns)	396
Full crossing angle (μrad)	0
Energy spread (units 10^{-3})	0.14
Bunch length (cm)	p: 50, $\bar{p}$: 45
Beam radius (10^{-6} m)	p:28, $\bar{p}$:16
Free space at interaction point (m)	$\pm$6.5
Initial luminosity decay time $-L/(dL/dt)$ (hr)	6 (average)
Turn-around time (min)	150
Injection energy (TeV)	0.15
Transverse emittance ($10^{-9}\pi$ rad-m)	p: 3, $\bar{p}$:1
Beam-beam tune shift per crossing (units 10^{-4})	p: 120, $\bar{p}$: 120
Particles per bunch (units 10^{10})	p:26, $\bar{p}$: 9
Bunches per ring per species	36
Average beam current per species (mA)	p: 70, $\bar{p}$: 24
Circumference (km)	6.28
Magnetic length dipole (m)	6.12
Length of standard cell (m)	59.5
Phase advance per cell (deg)	67.8
Dipoles in ring	774
Quadrupoles in ring	216
Peak magnetic field(T)	4.4

Table 2.1: Tevatron Parameters

side view of the upgraded DØ detector is show in Fig. 2.2. The only particles that cannot be directly measured at DØ are neutrinos, though measurements of the missing transverse energy from the calorimeter may indicate the presence of neutrinos in interactions.

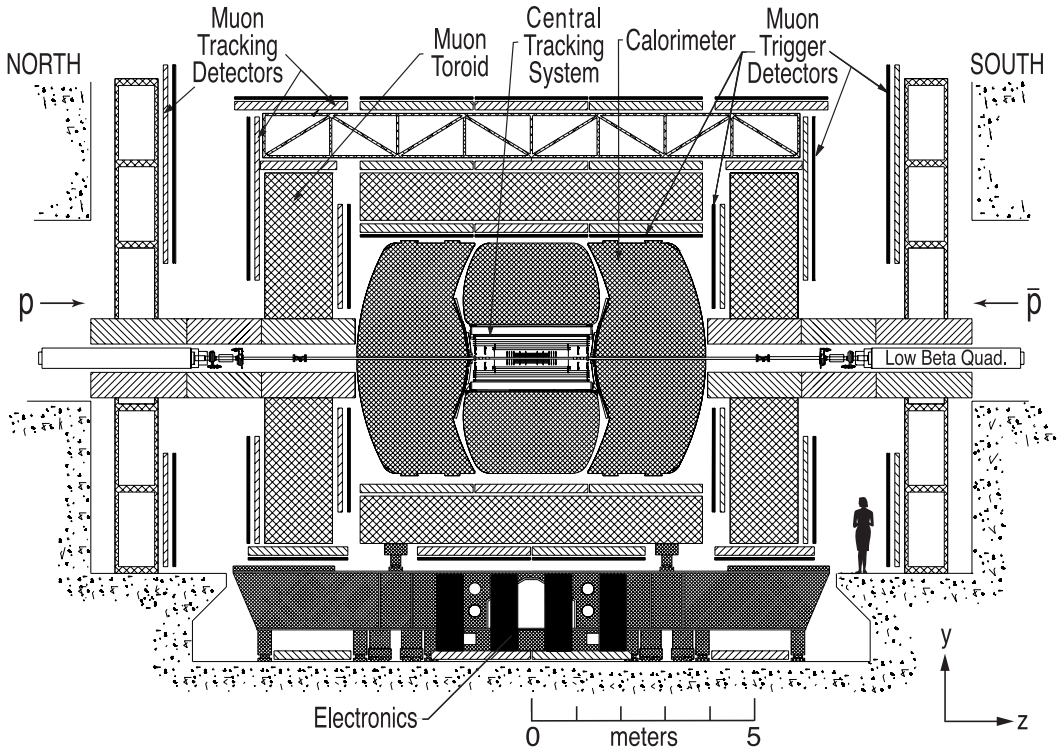

Figure 2.2: Diagram of the RunII DØ detector. The right-handed coordinate system in the detector is also shown here.

The detector was significantly upgraded before the start of RunIIa [22]. The system includes a silicon microstrip tracker and a scintillator-fiber tracker located within a 2 T solenoidal magnet. The silicon microstrip tracker is able to identify displaced vertex for b-quark tagging, and also measuring of mesons lifetimes. The Forward muon system's proportional drifts chambers have been replaced by minidrift tubes and trigger scintillation counters that can withstand the harsh radiation environment and additional shielding has been added. In the central region, scintillation counters have been added for improved muon triggering. In addition, the DØ detector was upgraded during the 2006 shutdown just prior to the start of RunIIb. During that shutdown, another silicon layer was added to the silicon tracking system. The trigger system was also upgraded to handle the expected increases in luminosity while keeping within data bandwidth constrains.

2.2.1 Luminosity, coordinate system and parameters at DØ

Luminosity

The DØ detector is designed to operate with delivered instantaneous luminosities of $2 \times 10^{32}\text{cm}^{-2}\text{s}^{-1}$. The Tevatron timing structure produces a 1.7 MHz rate of bunch crossings within the detector, with the detector capturing data during each bunch crossing window. At typical DØ luminosities, about $10^{32}\text{cm}^{-2}\text{s}^{-1}$ where the total proton-anti-proton interaction cross section is about 70 mb, about two proton-anti-proton interactions are expected during each beam crossing. The instantaneous luminosity is a measure of beam interactions per unit area per unit time and it is given by

$$\mathcal{L} = f\frac{n_p n_{\bar{p}}}{4\pi\sigma_x\sigma_y} \tag{2.1}$$

where $n_{p(\bar{p})}$ is the number of particles in the proton (anti-proton) beam, f is the rate at which these particle interacts, and $\sigma_{x(y)}$ is the transverse (longitudinal) profiles of the beams. The luminosity integrated over time is called integrated luminosity, which is expressed in units of inverse barns, where $1\,\text{b} = 10^{-24}\,\text{cm}^2$.

Coordinate system and variables at DØ .

The DØ collider detector is cylindrically symmetric. The coordinates r, ϕ, and z are used. The coordinate system of the detector is defined such that the proton's direction of motion is along the z-axis, i.e., along the axis of the beampipe as can be seen on Fig. 2.2. The radial coordinate is a perpendicular distance away from the center of the beampipe. The angle ϕ, ranging between 0 and 2π , is measured counterclockwise from a horizontal plane bisecting the detector. The antiprotons move in the opposite direction of the protons.

It is convenient to define the transverse momentum of a particle, p_T. It is defined as the component of the momentum vector that is perpendicular to the beam axis and can be written as $p_T = \sqrt{p_x^2 + p_y^2} = |\mathbf{p}|\sin\theta$. Similarly, the longitudal momentum is expressed as $p_z = |\mathbf{p}|\cos\theta$. In the same way, the transverse energy is $E_T = E\sin\theta$, where $\mathbf{p}$ and E

represents the three-dimensional momentum and total energy of the particles and θ is the production angle, that is measured from the z-axis.

The pseudo-rapidity η, defined as

$$\eta \equiv -\ln \tan\left(\frac{\theta}{2}\right) \tag{2.2}$$

approximates to the true rapidity, y, given by

$$y = \frac{1}{2}\ln\left(\frac{E + p_z c}{E - p_z c}\right), \tag{2.3}$$

for finite angles in the limit $(mc^2)/E \to 0$. The so-called central region is defined as the region where $|\eta| < 1$ and the forward region where $1 < |\eta| < 2$.

Since both ϕ and η differences between particles are Lorentz invariant, we can define the Lorentz invariant cone around a single particle or detector position, ΔR, as

$$\Delta R = \sqrt{(\Delta\phi)^2 + (\Delta\eta)^2} \tag{2.4}$$

where $\Delta\phi$ and $\Delta\eta$ are the differences between the two particles for those variables.

In the following section we will give a description of the components of the detector, focusing in the relevant components to this analysis. For completeness we will mention all components of the detector. For a detailed description of the DØ detector, see Ref. [22].

2.3 The tracking system

The DØ tracking system consists of the following systems: the silicon microstrip tracker (SMT), silicon track trigger (STT), central fiber tracker (CFT), central preshower (CPS) and forward preshower (FPS), and the central tracker trigger (CTT). The SMT, CFT, CPS and FPS are all hardware systems. The STT uses information from the SMT and CTT to make Level 2 trigger decisions, while the CTT uses information from the CFT, CPS and FPS

to make both Level 1 and Level 2 trigger decisions. Working together, the SMT and CFT can locate the primary (PV) and secondary (SV) vertices, which are the particle's points of production and decay, respectively. A schematic view of the tracking system is shown in Fig. 2.3. More information on STT and CTT can be found in Ref. [22].

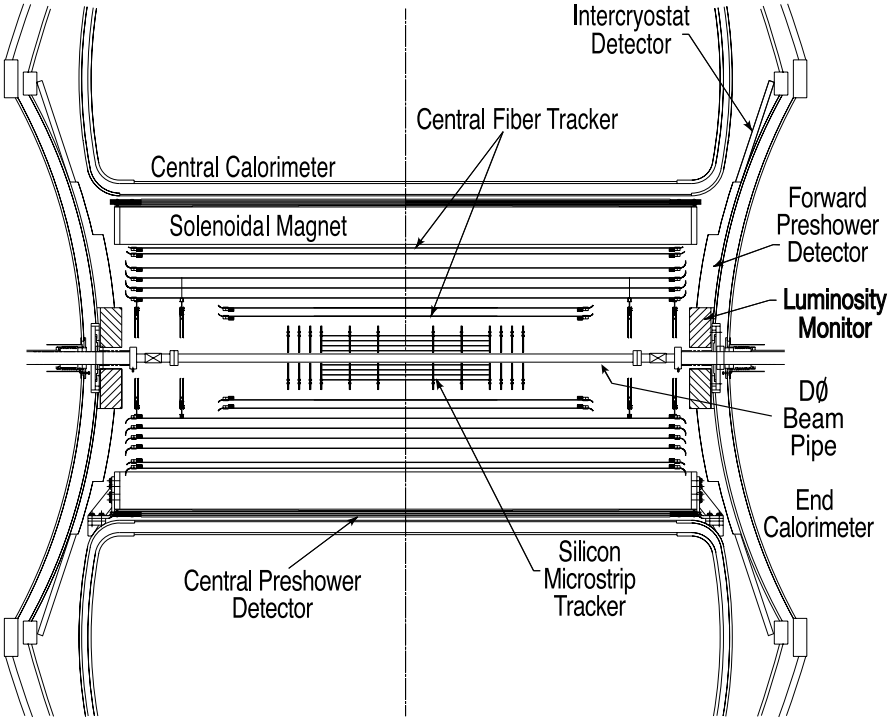

Figure 2.3: The tracking system. Also shown are the locations of the solenoid, the preshower detectors, luminosity monitor, and calorimeters. Not to scale.

2.3.1 Silicon Microstrip Tracker

The DØ detector's vertexing capability is greatly enhanced by a silicon tracking system. Silicon-based tracking provides good hit resolution and was placed close to the interaction region for better resolution. The Silicon Microstrip Tracker is the innermost section of the DØ detector. It consists of fabricated layers of thin silicon wafers oriented parallel or perpendicular to the beam pipe. Particles pass through the silicon wafers and produce electron-hole pairs that are separated by electric fields and collected by the capacitors and later read-out in the form of the electronic signals. The SVX2 read-out chips of 128 channels each carry out the particle's information. It is a hybrid system as it is composed of both barrels and

disk detectors, called F-disks and H-disks. The RunIIa SMT detector was comprised of six 12 cm long barrels in four layers with F-disk detectors in between the barrel sections and four large-area H-disk detectors, two at each of the far ends of the barrels. The H-disks provide coverage up to $|\eta| < 3$. Figures 2.4 and 2.5 shows the layout of the RunIIa SMT silicon system and a schematic view of a SMT ladder, respectively. A more detailed description of the RunIIa SMT system can be found in Ref. [22].

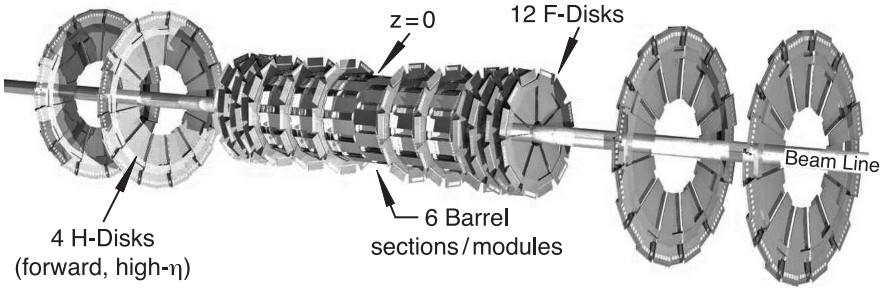

Figure 2.4: The layout of the RunIIa SMT system. It is composed by barrels, F-disks, and H-disks. The barrels are parallel to the beampipe, and the F-disks are spaced in between the barrels. The H-disks are the four larger-area disks at the outer ends of the silicon system.

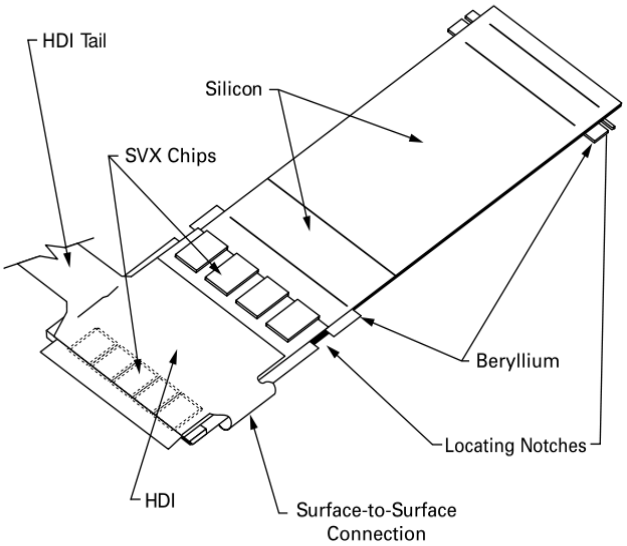

Figure 2.5: Schematic view of a SMT ladder

The detector uses a combination of single sided (SS), double sided (DS), and double-sided double-metal (DSDM) technology. All sensors were required to exhibit a leakage current less than 260 nA/cm^2. Each channel was tested for that leakage current, AC coupling capacitance, and AC coupling leakage to 80 V. Barrel ladders are supported by beryllium bulkheads

machined with the posts and pinholes for ladder support. Disks are supported by beryllium rings.

The layer Ø in the SMT

For the RunIIb, the SMT system was upgraded with a new barrel layer of silicon called Layer Ø. It was added fitting around the beampipe and inside the RunIIa SMT silicon layers at a distance of 1.67 cm from the interaction region. In addition, the outermost H-disks on either end of the SMT were removed. This was done to provide readout electronics for Layer Ø by sacrificing the least-important SMT disks, as installation of new electronics was not possible due to physical logistics in the DØ collision hall.

The Layer Ø uses SVX4 readout chips, whereas the RunIIa SMT system is comprised of SVX2 readout chips. The SVX4 chips are more stable and more radiation hard than the SVX2 chips. In addition, Layer Ø provides approximately a 30% improvement in single-hit resolution, making Layer Ø an important improvement over the RunIIa SMT detector. Layer Ø is comprised of 48 single-sided silicon sensors of 256 channels each. Note that the F- and H-disks of the original SMT system are made from double-sided silicon sensors. Layer Ø has an inner layer at $r = 16.0\,\text{mm}$ and an outer layer at $r = 17.6\,\text{mm}$; the edges of the two layers slightly overlap to maximize the acceptance of Layer Ø. Each of the sensors is attached to a hybrid of two $0.25\,\mu\text{m}$ silicon SVX4 chips using a low-mass along cable. Signals from the sensors are carried through the low-mass cables to the hybrid chips. From there, the signal is digitized and then sent using digital jumper cables connected to junction cards to adapter cards through twisted pair cables. The adapter cards allow the voltage requirements of the SVX4 chips to interface to the remaining electronics, as the voltage requirements of the SVX2 chips are different. The electronics that were used by outer H-disks removed during the 2006 shutdown make up the remaining readout electronics for Layer Ø.

2.3.2 Central fiber tracking

The Central Fiber Tracking (CFT) consists of scintillating fibers mounted on eight concentric support cylinders and occupies the radial space from 20 to 52 cm from the center of the beampipe. The two innermost cylinder are 1.66m long; the outer six cylinders are 2.52 m long. Each cylinder supports one doublet layer of fibers oriented along the beam direction (z) and a second doublet layer at stereo angle of $+3^o(u)$ or $-3^o(v)$. Doublet layers with fibers oriented along the beam axis are referred to as axial layers, while the doublet layers oriented at small angles to as stereo layers. From the smallest cylinder outward , the fiber orientation is $zu - zv - zu - zv - zu - zv - zu - zv$. The scintillator fibers are coupled to clear fiber waveguides which carry the scintillation light to visible photon counters (VLPCs) for readout. The small fiber diameter gives fiber of the CFT an inherent doublet layer resolution of about 100 μm.

Signal form the axial doublet layers are used to form a fast Level 1 hardware trigger based upon the number of track candidates above a specific p_T threshold (with a minimum threshold of 1.5 GeV/c). Level 1 track candidates are used for the Level 2 trigger, and the Level 3 trigger uses the full CFT readout.

The scintillating fibers, including cladding, are 835 μm in diameter and 1.66 or 2.53 m in length. They are optically connected to clear fibers waveguides of identical diameter which are 7.8 to 11.9 m long. The fibers have a multi-clad structure consisting of a core surrounded by two claddings. The scintillating fiber is structurally and chemically similar to the clear fiber, but contains fluorescent dyes. The CFT uses about 200 km of scintillating fiber and 800 km of clear fiber.

Light production in the fibers is a multistep process. The bass core material is polystyrene (PS). The PS is doped with the organic fluorescent dye paraterphenyl (PT) to about 1% in weight. Excitations in the PS are rapidly transferred to the PT via a non-radiative dipole-dipole interactions. PT has a rapid florescence decay (a few nanoseconds) and a short emission wavelength (approx. 340 nm). The mean free path of the emitted light is only a few hundred microns in the PS. To get the light out of the detector, a secondary or wave

shifter, dye, 3-hydroxyflavone (3HF), is added at low concentration (1500ppm). The 3HF is spectrally matched to the PT but has a minimal optical self-absorption. The 3HF absorbs the 340 nm radiation from the PT and re-emits it at 530 nm which is well transmitted in PS.

Surrounding the PS core, whose refractive index is $n = 1.59$, are two claddings, each approximately $25\,\mu$m thick: an inner layer of polymethylmethacrylate (PMMMA) with $n = 1.49$, and a outer layer fluoro-acrylic with $n = 1.42$, the PMMA inner cladding serves as a mechanical interface between the core an the outer cladding, which are mechanically incompatible. The multiclad fibers is both mechanically an optically superior to single-clad fiber and typical values of the attenuation length are about 5 m for the scintillator fibers and 8 m for the clear fiber.

We observe light form only one end of each scintillator fiber. The opposite end of each of the scintillator fibers was mirrored by sputtering with an aluminum coating that provides a reflectivity of 85% to 90%.

The scintillators fibers were made into ribbons consisting of 256 fibers in two layers of 128 fibers each. Precisely spaced grooves were machined into a long, 1/16"-thick piece of Delrin plastic. The spacing between groves varies between 928 and $993\,\mu$m and depends on the radius of the corresponding support cylinder. The grooved plastic was inserted into a rigid, curved backing with the desired radius an the scintillator fibers were laid in and glued together to form the doublet ribbons; the two layers of fiber are offset by one-half of the fiber spacing.

The readout ends of the fibers were carefully positioned and adhesively bonded into v-groove connectors, and the mass-terminated ribbon and connectors were polished to facilitate high efficiency light transmission across the connectors. The light transmission through the v-groove connectors, with optical grease between the fibers ends, is approximately 95%. The position of each fiber within the ribbon was verified with and accuracy of better than $25\,\mu$m rms.

The eighth mechanical support for the CFT consist of eight carbon fibers support cylin-

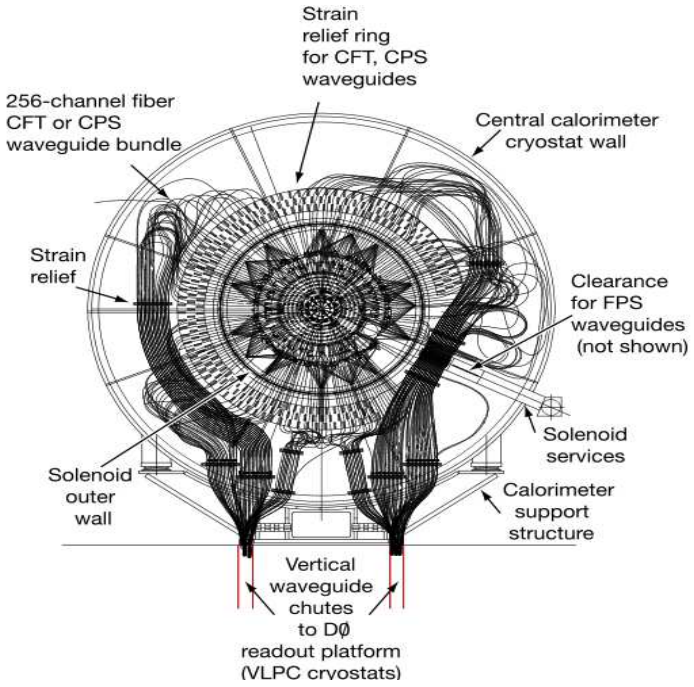

Figure 2.6: A schematic view of the CFT

ders double walled with a 0.25"-thick core of Rohacell. For tracks traversing the detector at normal incidence, the thickness of each cylinder can be broken down as follows: 0.28% of radiation length fo the scintillators fibers, 0.32% for the carbon fibers support cylinder, 0.13% for the glue used to make the ribbons out of fibers, and 0.17% for the glue used to attach the ribbons to the support cylinders.

The light generated by the passage of charged particles through the scintillator fibers of the CFT is converted into electrical signal by the VLPCs, housed in the VLPC cassettes. VLPCs are impurity-band silicon avalanche photodetectors that operate at 9K, an are capable of detecting single photons. They provide fast response, excellent quantum efficiency ($> 75\%$) high gain (17,000 to 65,000) , low gain dispersion, and capability of functioning in a high background environment.

The CFT requires 76,800 channels of VLPC readout. Better than 99.8% of the individual VLPC channels in these cassettes met or exceeded the desired performance specification during cryogenic qualifications test preformed prior to installation at DØ . An schematic view of the CFT is shown in Fig. 2.6.

2.4 Solenoidal Magnet

The superconducting solenoidal magnet was designed to optimize the momentum resolution, $\delta p_T/p_T$, and tracking pattern recognition within the constraints imposed by the Run I detector. The overall physical size of the magnet was determined by the space available within the central calorimeter vessel: 2.73 m in length and 1.42 m in diameter. We selected a central field of 2 T after considering the momentum resolution and tracking pattern recognition, the available space, and thickness of the cryostat which depends on the thickness of the conductor and support cylinder. Services such as cryogens, magnet high currents buses, and vacuum pumpout and relief must reach the magnet from the control dewar; that is the interface between the fixed cryogenic piping and the movable detector through the narrow space (7.6 cm) between the central and end calorimeter vacuum vessels. The magnet system is controlled remotely, including cool down, energization, de-energization for field reversal, quench recovery and warmup, without access to the magnet cryostat, service chimney , or control dewar. A perspective view of the solenoid inside the central calorimeter with its chimney and control dewar is shown in Figure 2.7.

2.4.1 Magnetic field

The magnetic field of the full magnet system is modeled using the TOSCA [24] program. The calculated field map was compared with the measured field in two locations: near the internal radius of the solenoid cryostat ($r \approx 54\,\mathrm{cm}$) at $z = 4$ and in the gap at the top of the central muon toroid steel. Within the solenoid the measured filed is $20.141 \pm 0.005\,\mathrm{kG}$; the calculated field at this location is 20.158 kG. The calculated magnetic field is scaled by 0.09% to agree with the measurement. With full operating current in the toroid coils here is a 4.5% difference between the calculated and measured field at the CF gap, requiring an adjustment in the calculated field for the CF toroid. A $y-z$ view of the magnetic field with both the toroid and solenoid magnets at full current is show in Figure 2.8

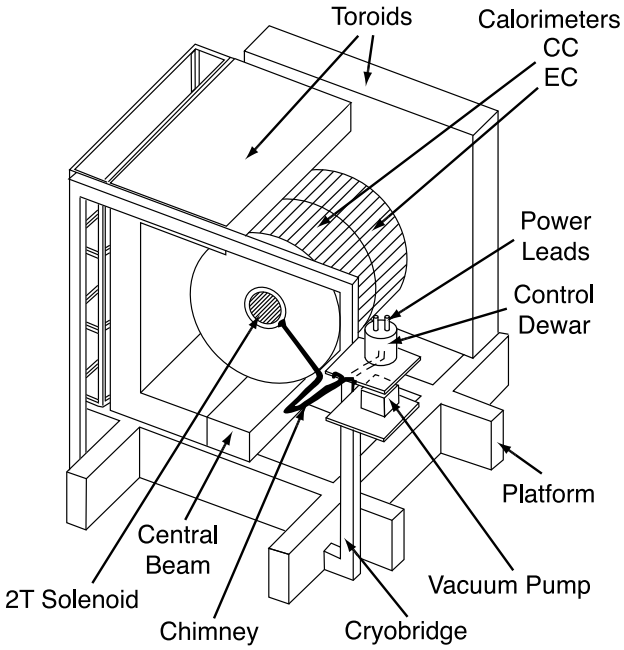

Figure 2.7: Perspective view of the solenoid inside the central calorimeter. One end calorimeter and several muon chambers have been omitted for clarity. Also shown are the service chimney an the control dewar.

2.5 Preshower Detectors

The preshower detector aid in the electron identification and background rejection, They function as calorimeter as well as tracking detectors, enhancing the spacial matching between tracks and calorimeter showers. The central central preshowers detectors (CPS) covers the regions $|\eta| < 1.3$ and is located between the solenoid an the central colorimeter. The two forward preshower detectors (FPS) cover $1.5 < |\eta| < 2.5$ and are attached to the faces of the end of the calorimeters. The locations of the preshower are shown in Fig. 2.3. Since in this analysis we do not use the preshowers because of that we will not give further description.

2.6 Calorimeters

The DØ calorimeter consist of three uranium/liquid argon calorimeter an the intercryostat detector. The calorimeter were designed to provide the energy measurement for electrons, photons,and jets in the absence of a central magnetic field (as was the case during Run I on the Tevatron) , as well as assist in the identification of electrons, photons, jets and

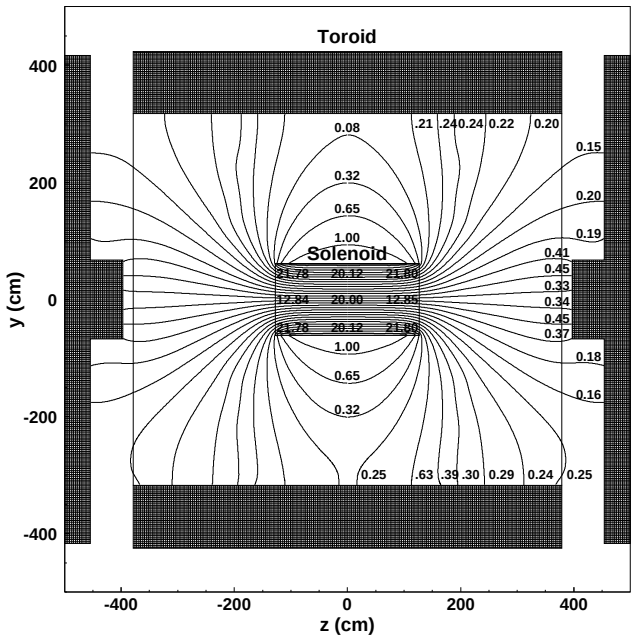

Figure 2.8: The $y - z$ view of the DØ magnetic field with both the toroid and solenoid magnets at full current. The field lines are projections onto the $y - z$ plane; the left and right line ends differ by up to 2.5 m in x. The numbers give strength of the magnetic field at various locations in kG.

muons and establish the transverse energy balance in an event. The calorimeter themselves are unchanged from Run I and are described in detail in Ref. [23]. They are shown in Figure 2.2.

The Central calorimeter (CC) cover $|\eta| \leq 1$ and the two end calorimeters, ECN (north) and ECS (south), extend coverage to $|\eta| \approx 4$. Each calorimeter contains an electromagnetic sections closest to the interaction region followed by fine and coarse hadronic sections. The active medium for all of the calorimeters is argon and each of the three calorimeters (CC,ECN,ECS) is located within a cryostat that maintains the temperature at approximately 80 K. Different absorber plates are used in different locations. The electromagnetic sections (EM) use thin (3 or 4 mm in the CC and EC, respectively) plates, made from nearly pure depleted uranium. The fine hadronic sections are made from 6-mm-thick uranium-niobium (2%) alloy. The coarsic hadronic modules contains a relatively thick (46.5 mm) plates of either cooper in the CC or stainless steel in the EC. Since this detector play a very modest role in the analysis we will not describe more of it, see Ref. [22] for a more detailed

description.

2.7 Muon system

Muons played a main part in the analysis of B_d^0 and B_s^0 since two of the four final particles are muons, and even more we use the $J/\psi \to \mu^+\mu^-$ as our very first discriminating criteria.

For Muon triggering and measurement, the upgraded detector uses the original central muon system proportional drift tubes (PDTs) and a toroidal magnets, central scintillator counters (some new and some installed during Run I), and a completely new forward muon system. The central muon system provides coverage for $|\eta| \leq 1.0$. The new forward muon system extends muon detection to $|\eta| \approx 2.0$, uses minidrift tubes (MDTs) rather that PDTs, and includes trigger scintillator counters and beam pipe shielding.

During Run I, a set of scintillators counters, the cosmic cap, was installed on the top and upper sides of the outer layer of the central muon PDTs. This coverage has been extended to the lower sides and bottom detector, to form the cosmic bottom. These trigger scintillator counters are fast enough to allows us to associate a muon in a PDT with the appropriate bunch crossing and to reduce the cosmic ray background. Additional scintillator counters, the Aϕ counters, have been installed on the PDTs mounted between the calorimeter an the toroidal magnet. The Aϕ counters provide a fast detector triggering and identifying muons for rejecting out-of-time background events.

The scintillators counters are used for triggering; the wire chambers are used to precise coordinate measurements as well as triggering. Both types of detectors contribute to background rejection: the scintillator with timing information an the wire chambers with track segments. Exploded views of the muon system are shown in Figures 2.9 and 2.10.

2.7.1 Central muon detector

The central muon system consist of a toroidal magnet, drift chambers, the cosmic cap an a bottom scintillation counters, an the Aϕ scintillation counters.

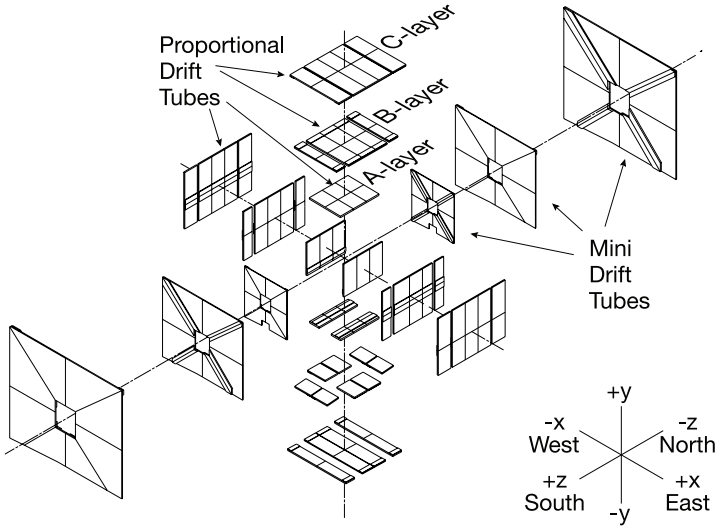

Figure 2.9: Exploded view of the muon wire chambers.

Toroidal magnets

The Toroidal magnets are described in detail in Ref. [23] and shown in Figure 2.2. Having a Stand-alone muon-system momentum measurement: enables a low p_T cutoff in the Level1 muon trigger, allow for a cleaner matching with the central detector tracks, rejects π/K decays and improves the momentum resolution for high momentum muons.

The central toroid is a square annulus 109 cm thick whose inner surface is about 318 cm from the Tevatron beamline;it covers the region $|\eta| \leq 1$. The two ends toroids are located at $454 \leq |z| \leq 610$ cm. In the center of each toroid is a 183 cm square hole centered on the beamline. in x and y the magnets extends 426 cm from the beamline. During Run II, the magnets are being operated at series, at a currents of 1500A. As in Run I, the polarity of the magnets during data collection is regularly reversed.

Central muon drift chambers

The central drift chambers consist in three layers of drift chambers: one inside the toroidal magnet called A-layer and two outside called B-layer and C-layer, and cover $|\eta| \leq 1$. Approximately 55% of the central region is covered by three layers of PDT; close to 90% is covered by at least two layers. The drift chambers are large, typically 2.8 X 5.6 m_2, and made of rectangular extruded aluminum tubes. The PDTs outside the magnets have three decks of

drift cells; the A-layer has fourth decks with the exception of the bottom A-layer which have three decks. The cells are 10.1 cm across; each chamber is 24 cells wide an typically contains 72 or 96 cells. Along with an node wire at the center of each cells, vernier cathode pads are located above and below the wires to provide information on the hit position along the wire. the wire are ganged together in pairs within a deck and then read by electronics located at the end of each chamber.

For each PDT hit the following information is recorded: the electron drift time, the difference ΔT in the arrival time of the hit between a hit cell an the neighbor connected to it, an the charge deposition on the inner an outer vernier pads. Both ΔT and the charge deposition are used to determine the hit position along the wire. The drift distance resolution is $\sigma \approx 1\,\mathrm{mm}$. The resolution of the ΔT varies from 10cm to 50 cm. Using charge division the pad signal resolution is about 5 mm.

To reduce the number of bunch crossing which occur during one maximum drift time interval, we are using a faster gas mixture than we used during Run I. The new mixture is 84 % argon, 8% methane, and 8%CF_4. The operating high voltage is 2.3 kV for the pads and 4.7 kV for the wires. The drift velocity is approximately 10 $cm/\mu s$, for a maximum drift time of about 500 ns. The contribution to the hit position uncertainty due to diffusion is about 0.4 mm.

Cosmic cap and bottom counters

The cosmic cap for bottom counters are installed on the top, sides and bottom of the layer of the central muon PDTs. They provide a fast timing signal to associate a muon in a PDT with the appropriate bunch crossing an discriminate against the cosmic ray background.

The cosmic cap counters are made from grooved 0.5". Bicron 404a scintillator with BCF 91 a an Kuraray Y11 wave-shifting fibers glued into the groves using bicron 600 optical epoxy. There are 240 counters, 25" wide, and 81.5"-113" long. The counters are positioned with their width along z and length along ϕ . The grooves are 1.75 mm deep and 4 mm wide; they run along the length of the counter, from end to just pass the center of the counter.

They are spaced 8 mm apart so that half of the surface is covered with fibers. Each groove contain four fibers. The fibers are read using phototubes.

The cosmic bottom complete the scintillator coverage of the central toroidal magnet. There are 132 counters. of two different design. The forty eight counters located in the outside of the center of the bottom layer B-layer of PDT, are nearly identical to the cosmic cap counters described above. The sixty-eight counters located on the undersides of the remaining B and C layers are similar to the cosmic cap counters except that the bottom counters have fewer fibers and are placed in vertical rather than horizontal grooves.

An important difference between the cosmic cap an the cosmic bottom counters is that the bottom counters are positioned with their narrow dimension along ϕ and their long dimension along η. This orientation has better matching in ϕ with the central fiber tracker trigger.

Aϕ scintillator counters

The Aϕ scintillator cover the A-Layer PDTs, those between the calorimeter and the toroid. They provide a fast detector for triggering on and identifying muons and for rejecting out-of-time backscatter from the forward direction. In-time scintillation counter hits are matched with tracks in the CFT level 1 trigger for high-p_T single muon and for low-p_T dimuon triggers. The counters also provide the time stamp for low-p_T muons which did not penetrate the toroid and thus do not reach the cosmic cap or bottom counters.

The layout of the forward muon system is shown in Fig. 2.2. It covers $1.0 \leq |\eta| \leq 2.0$ and consist of four major parts: the end toroidal magnet, three layer of MDTs for muon track reconstruction, three layer of scintillator counters for triggering on events with muons, and shielding around the beampipe.

Mini drift tubes were chosen for their short electron drift time (less than 132 ns), good coordinate resolution (less than 1 mm), radiation hardness, high segmentation, and low occupancy, The MDTs are arranged in three layers (A, B, and C, with A closest to the interaction region inside the toroidal magnet and C furthest away), each of which is divided

into eight octant's Fig. 2.9. A layer consists of three (layers B and C) or four (layer A) planes of tubes; each tube comprises eight $1 \times 1\text{cm}^2$ cells. The tubes are mounted along magnetic filed lines (the field shape in the forward toroids is more "square" than "circular"). The entire MDT system contains 48,640 wires; the maximum tube length is 5830 mm in layer C.

The efficiency of the MDT is 100% in the active area of the cells for tracks which are perpendicular to the MDT plane. The overall plane efficiency is less, due to the wall thickness and PVC sleeves, and is approximately 95% for our geometry.

The momentum resolution of the forward muon spectrometer is limited by multiple scattering in the toroid and the coordinate resolution of the tracking detector. The standalone momentum resolution of the forward muon system is approximately 20% for muon momentum below 40 GeV/c. The overall muon momentum resolution, including information from the SMT and CFT, is defined by the central tracking system for muons with momentum up to approximately 100 GeV/c; the forward muon system improves the resolution for higher momentum muons and is particularly important for tracks with $1.6 \leq \eta \leq 2.0$, i.e. those which do not go through all layers of the CFT.

Trigger scintillation counters

The muon trigger scintillator counters are mounted inside (layer A) or outside (layer B and C) of the toroidal magnet (Fig. 2.2). Each layer is divided into octants containing about ninety-six counters. The ϕ segmentation is 4.5^o and matches the CFT trigger sectors. The $\eta = 0.12(0.07)$ for the first inner (last three) rows of counters. The largest counters, outers counters in the C layer, are $60 \times 110\,\text{cm}^2$. The B and C layers have geometries similar to that of the A layer, but limited in places by the collision hall ceiling and floor.

2.8 Forward proton Detector

There is a forward proton detector that measures protons and antiproton scattered at small angles (of the orders of 1 mrad) that are missed by the main DØ detector. These detector

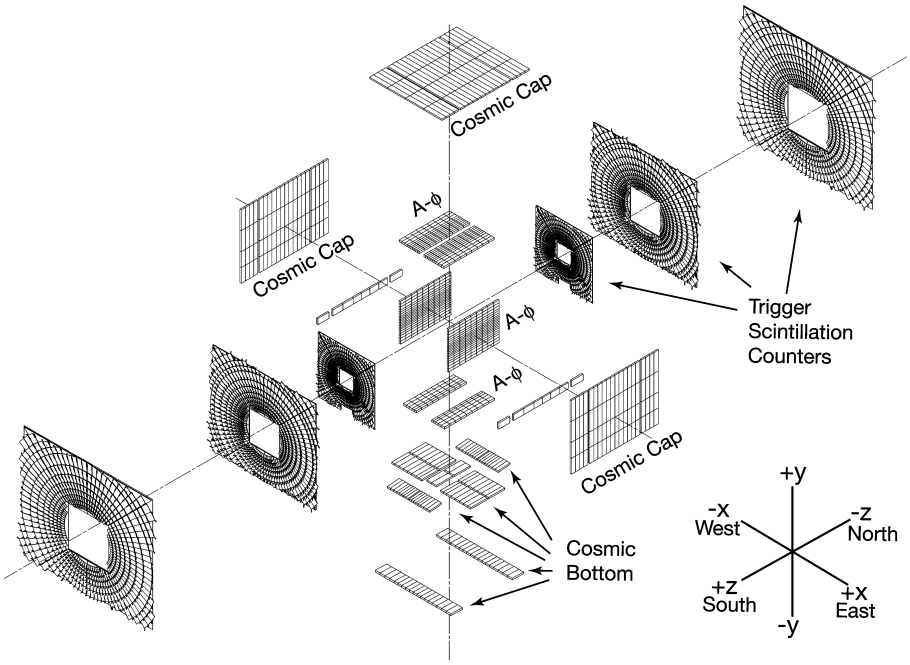

Figure 2.10: Exploded view of the muon scintillation detectors. Note that the backs of the scintillation detectors are shown for the south end.

is not used in this analysis. And we will not talk further of it.

2.9 Luminosity monitor

The primary purpose of the luminosity monitor (LM) is to make an accurate determination of the Tevatron luminosity at the DØ interaction region. This is accomplished by detecting inelastic $p\bar{p}$ collisions in a dedicated detector. The LM also serves to measure the beam halo rates, to make a fast measurement of the z-coordinate of the interaction vertex, and to identify beam crossings with multiple $p\bar{p}$ interactions. In these analysis we did not use a specific trigger and then the luminosity estimation was done in an approximate way we will explain the method in the analysis section.

2.10 Triggering

As a explained above we did not use a specific trigger. The trigger system in DØ consists of three levels. The first stage(Level 1 or L1) comprises a collection of hardware trigger elements

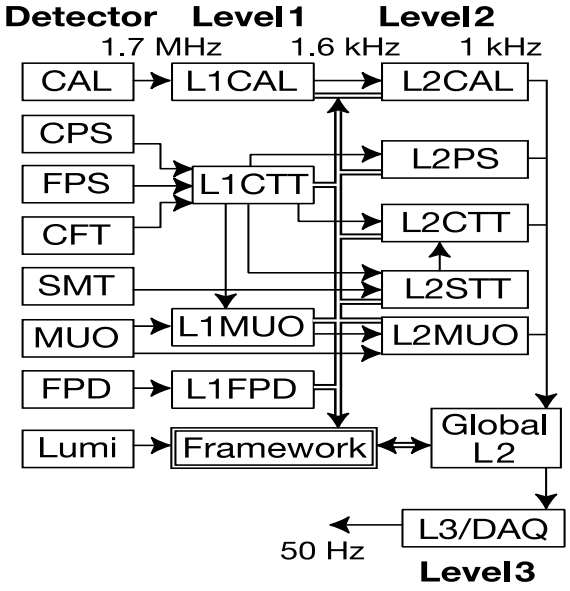

that provide a trigger accept rate of 1.6 kH. In the second stage (Level 2 or L2), hardware engines and embedded microprocessors associated with specific subdetectors process information used by a global processor in determining correlations between different detectors. L2 decisions are made within $100\mu s$ with and accept rate of about 1 kHz. Candidates from L1/L2 are passed to a farm of level 3 (L3) microprocessors sophisticated algorithms reduce the rate to about 50 Hz and these events are recorded for offline reconstruction a block diagram of elements of the DØ trigger system is shown in figure 2.10.

2.11 Event Simulation

The DØ event data model (EDM) is a library of C++ classes and templates whose purpose is to support the implementation of reconstruction and analysis software.

The conversion of the C++ objects used in the reconstruction program to a persistent format is handled by the DØ object model (DOoM) [34]. First, DOoM maintains a dictionary describing the layout of the C++ classes that are used persistently, which is generated by running a preprocessor over the C++ headers defining the classes. This preprocessor is based in a modified version of the CINT C/C++ interpreter (which also is used in the ROOT system [35])

The generation of Monte Carlo (MC) events involves multiple stages and many executables. To integrate all processes, all programs use the EDM to carry data in memory and DOoM to store persistent data. All code is organized in independent packages running in a standard DØ framework and is written in C++ or embedded in C++ driving routines.

The first step in MC event generation is the simulation of a physical process, a $p\bar{p}$ collision producing a particular final state. Nearly all existing event generator programs are written in Fortran, but the StdHep [36] code from FNAL Computing Division can be used to store the output is a standard common block format. This allowed us to write a C++ wrapper that converts the StdHep Fortran format to C++ classes satisfying the EDM requirements.

To trace particles through the DØ detector, determine where their paths intersect active areas, and simulate their energy deposition and secondary interactions, we use the CERN program GEANT v3.21 [37], which also is written in Fortran. A C++ wrapper is used to read files produced by the event generators and write the output of GEANT in DOom format this executable is called DØGSTAR. All subsequent steps in the event simulation are handled by programs written almost entirely in C++.

The DØSIM program modifies the generated Monte Carlo data to account for various detector-related effects. After particles from the simulated reaction have been traced through the detector, the generated energy depositions must be converted to the form that the real data takes when processed through the DØ electronics. Detector inefficiencies and noise (from detector an electronic readout) must be taken into account, an more than one interaction may occur during beam crossing. In a addition, some portions of the detector (such as the calorimeter) remain sensitive to interactions over the period of time that includes more than one beam crossing. Simulation of the trigger electronics and the effects of trigger on data selection is performed by a separate program, DØTRIGSIM. DØTRIGSIM contains simulation code only for the L1 trigger. The L2 and L3 triggers are based on filtering code, and exactly the same software run in DØTRIGSIM. The output of the DØSIM and DØTRIGSIM is in the same format as the data recorded at DØ data acquisition system, but contains additional MC information to make it possible to correlate detector data with the

original generator output.

2.12 Reconstruction

The DØ offline reconstruction program (RECO) is responsible for reconstructing objects used from physics analysis. It is a CPU-intensive program that processes collider events recorded during online data taking and simulated MC events. The executable is run on the offline farms and the results are placed into the central data storage system for further analysis. Information and results for each event are organized using the EDM. The EDM manages information within the event blocks called chunks. The raw data chunk (RDC), created either by an L3 processor node or the MC, contains the raw detector signals and is the primary input to RECO. The output from RECO consist of many additional chunks associated associated with each type of reconstructed object. RECO produces two formats or data tiers. The data summary tier (DST) contains all information necessary to perform any physics analysis, including limited re-reconstruction of high-level physics objects. The thumbnail (TMB) is a physics summary format less than one-tenth the size of the DST format. the TMB can be used directly to perform many analysis, an it allows the rapid development of event selection criteria to be applied to the DST sample.

RECO reconstruct events in several hierarchical steps. The first involves detector-specific processing. Detector unpackers process individual detector data blocks within the RDC, decoding the raw data information. associating electronic channels with physical detector elements, and applying detector-specific constants. For many of the detectors , this information is then used to reconstruct a cluster (for example, from the calorimeter and preshower detectors) or hit (from racking detectors) objects. These objects use the geometry constants to associate detector elements (energies and positions) with physical position in space. The second step in RECO focuses on the output of the tracking detector, reconstructing global tracks from hits in the SMT and CFT. This process, involving several different tracking algorithms, is the most CPU-intensive activity or RECO. The results are stored in corresponding

tracks chunks, which are used as input to the third step in RECO, vertexing. First primary vertex candidates are found . These vertexes indicate the location of the $p\bar{p}$ interactions and are used in the calculation of various kinematic quantities (e.g. E_T). Next, displaced vertex candidates are identified. Such vertexes are associated with decays of long-lived particles. The results of the above algorithms, information from each of the preceding reconstruction steps in combined and standard physics objects candidates are created. RECO first find electron, photon, muon neutrino, and jet candidates, after which it identifies candidates for heavy-quark and tau are identified next.

Chapter 3

Data selection and Monte Carlo analysis

In the following lines we will describe the cuts we use for the data selection in order to obtain the B_d^0 and B_s^0 mesons candidates. This is actually one of the toughest and more labor consuming part of the analysis, we will try to be as explicit as we can. Next we will make a Monte Carlo (MC) analysis in order to obtain the angular efficiencies which have a relevant importance in this analysis.

A cut is a selection criteria we use to eliminate the events that are not interesting for us, for example, if in given event we do not have a primary vertex how can we measure the decay distance, a global cut is a cut that we decide not to use in the optimization of the signal because was inherent to signal or because we consider will not improve the signal.

Because we want to reconstruct $B_s^0 \to J/\psi\phi$ and $J/\psi \to \mu^+\mu^-$, $\phi \to K^+K^-$ and we have a muon detector we use the J/ψ as a pseudo-trigger.

3.1 Data samples

The data samples used in these analyses are from the "b physics" single muon sample [49]. Those samples were further filtered using the standard J/ψ selection.

The data selection follow the same selection criteria as in Ref. [8]. It is worth to mention that this sample was optimized for the $B_s^0 \to J/\psi\phi$ decay and not for both.

3.1.1 SMT and CFT hits

The SMT and CFT hits are required to warranty good vertex and save time in process.

Reconstructed muon candidates are classified using two parameters: muon type and muon quality. The type of muon is given by the parameter *nseg*. A positive value for nseg indicates that the muon reconstructed in the muon system was matched to a track in the central tracking system. A negative value of nseg tells that the local muon could not be matched to a central track. The absolute value —nseg— indicates that the local muon is made up of a A-layer only hits, B or C-layer only hits (outside the toroid), or both A- and B- or C-layer hits. For this analysis, we deal only with muon types with a central track and a hit only in the A-layer (nseg=1) and with a central track and hits only in the B- and C-layers (nseg=2).The second parameter used to classify muon is the quality. The muon quality can be 'loose', 'medium' or 'tight'. Only —nseg—=3 muons can be tight.

- All four tracks are required to have at least one SMT (axial) hit;
- Tracks of opposite charge for muons and kaons;
- nseg of muons is allowed for any combination of nseg=1 and nseg=2 such that nseg=1+nseg=2> 4 and none being 0;
- Number of SMT (axial) hits > 1 for both mesons;
- Number of SMT (axial) hits + number of CFT hits > 7 for both muon tracks;
- Number of SMT (axial) hits + number of CFT hits > 7 for both kaon/pion tracks;
- Number of CFT hits > 0 or number of SMT(axial) hits > 4 for the muon tracks;
- Number of SMT (axial) hits > 1 for both tracks from K^{*0}

3.1.2 p_T of the candidates

- If leading muon is central, $p_T(J/\psi) > 4.0$ GeV/c;
- $p_T(\mu) > 1.5$ GeV/c;
- $p_T(K, \pi) > 0.7$ GeV/c;
- $p_T(K^{*0}, \phi) > 1.5$ GeV/c;
- $p_T(B_d^0, B_s^0) > 6.0$ GeV/c;
- If there are several ϕ candidates then the one with the largest p_T is selected.

The transverse momentum distributions are reported in Figs. 3.1 and 3.2

3.1.3 Mass windows

- $2.90 \leq M(J/\psi) \leq 3.3$ GeV/c^2 since we are only interested in the J/ψ signal;
- $0.85 \leq M(K^{*0}) \leq 0.93$ GeV/c^2;
- $1.01 \leq M(\phi) \leq 1.03$ GeV/c^2;
- $4.9355 \leq M(B_d^0) \leq 5.6105$ GeV/c^2;
- $5.0285 \leq M(B_s^0) \leq 5.7035$ GeV/c^2.

3.1.4 Lifetime windows

For both particles, we have the following lifetime windows

- $-0.08 < ct < 0.370$ cm;
- $\sigma_{ct} < 0.006$ cm.

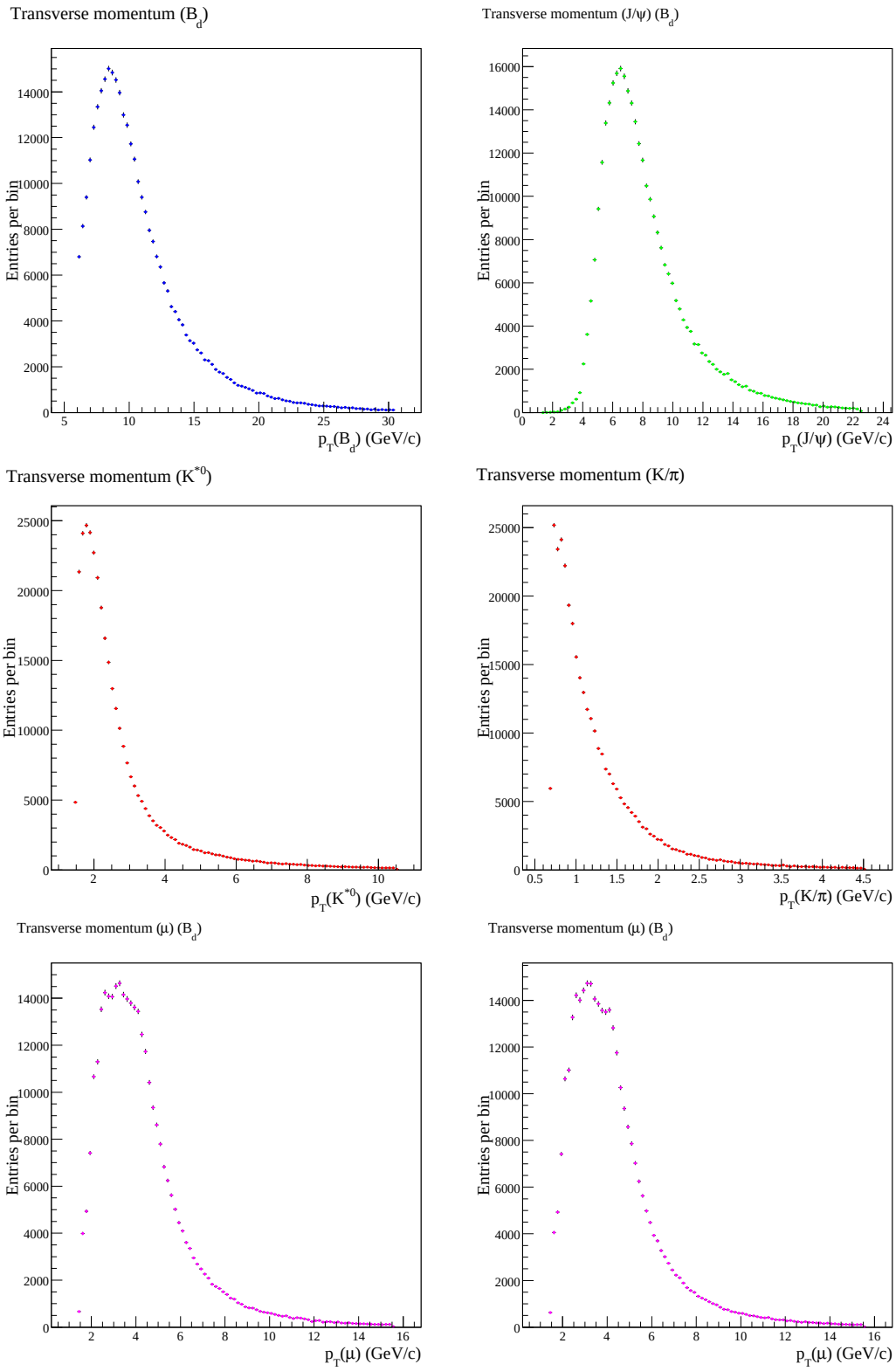

Figure 3.1: For the B_d^0. Transverse momentum distributions for B_d^0 (top left) and J/ψ (top right), K^{*0} (middle left) and trailing particle from K^{*0} (kaon or π) (middle right), and leading μ (bottom left) and trailing μ (bottom right).

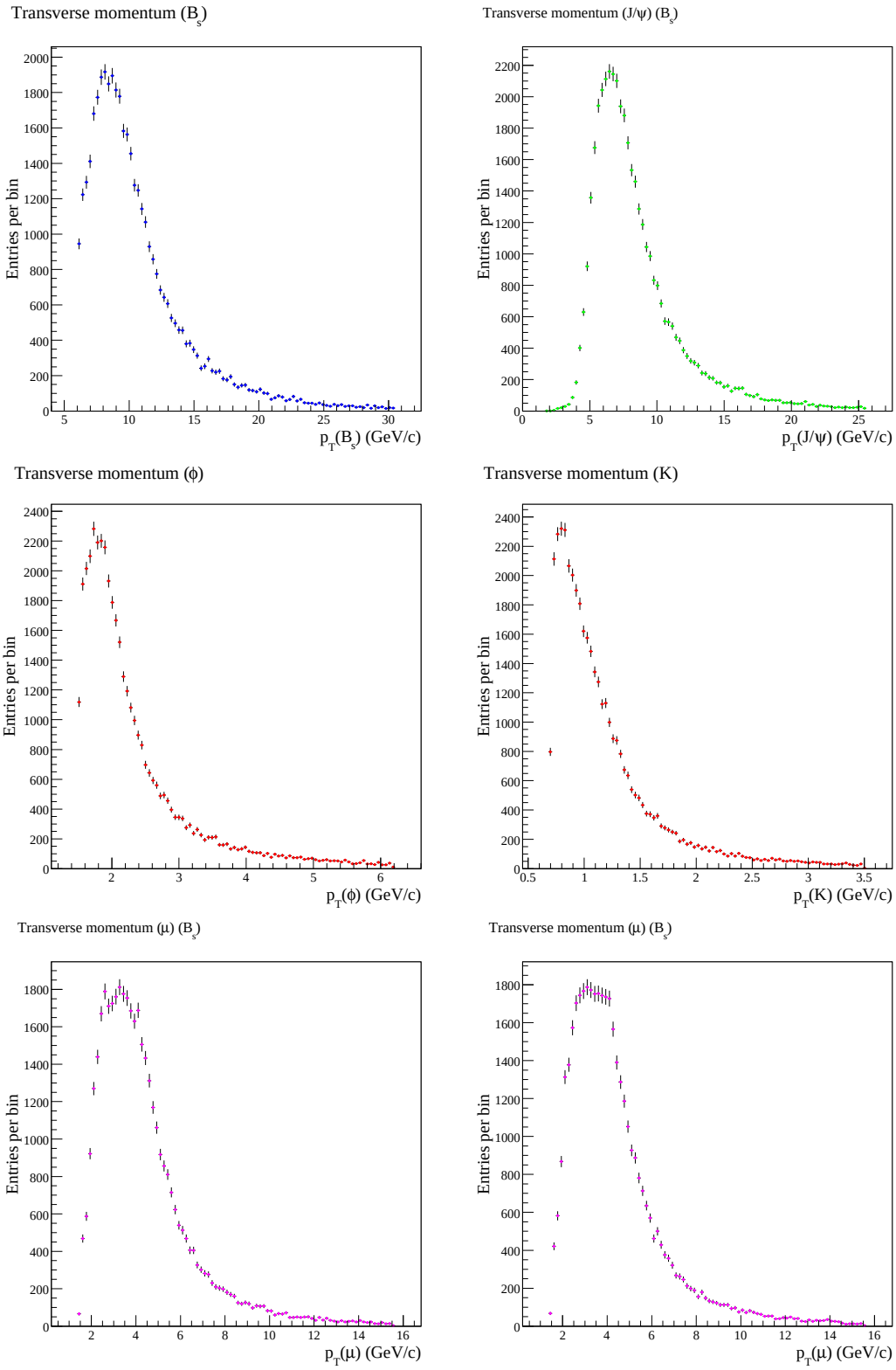

Figure 3.2: For the B_s^0. Transverse momentum distributions for B_s^0 (top left) and J/ψ (top right), ϕ (middle left) and trailing kaon (middle right), and leading μ (bottom left) and trailing μ (bottom right).

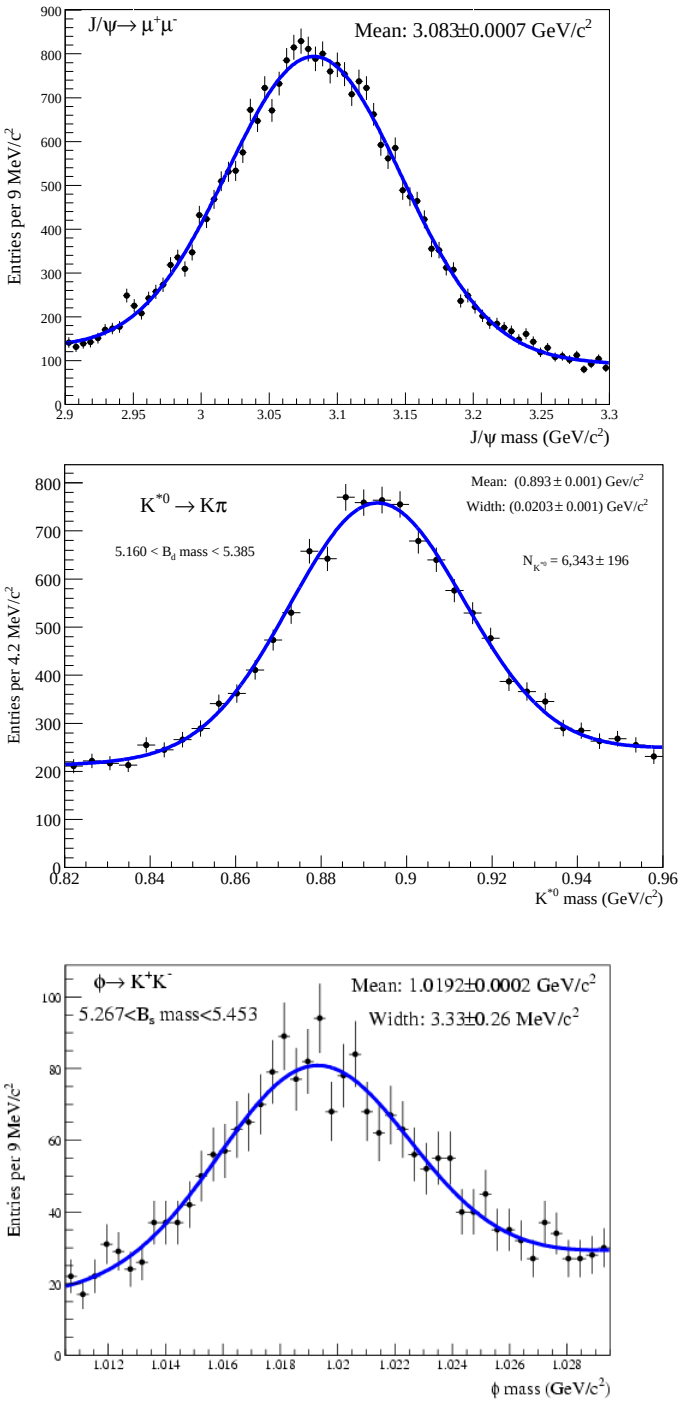

Figure 3.3: Plots of masses for the J/ψ (top), K^{*0} (middle), and ϕ (bottom). For illustrative purposes, all of them have a cut such that $(ct/\sigma_{ct}) > 5.0$

After applying all cuts, we found 334,199 total entries (signal+background) for the B_d^0, and 41,691 total entries for the B_s^0. The plots of the B_d^0 distributions for the variables that will be used in the analysis are reported in Appendix A. Similar distributions are obtained for the B_s^0 meson.

All available data from April 20th, 2003 to August 4th, 2007 were processed using the above criteria. We have removed events that fired only ip triggers and all the bad and special MUON, SMT and CFT runs from our analysis, using the DØ Official Offline Run Quality Database" [50].

For this dissertation, the integrated luminosity is about $2.8\,\mathrm{fb}^{-1}$. A plot of the RunII integrated luminosity is shown in Fig. 3.4.

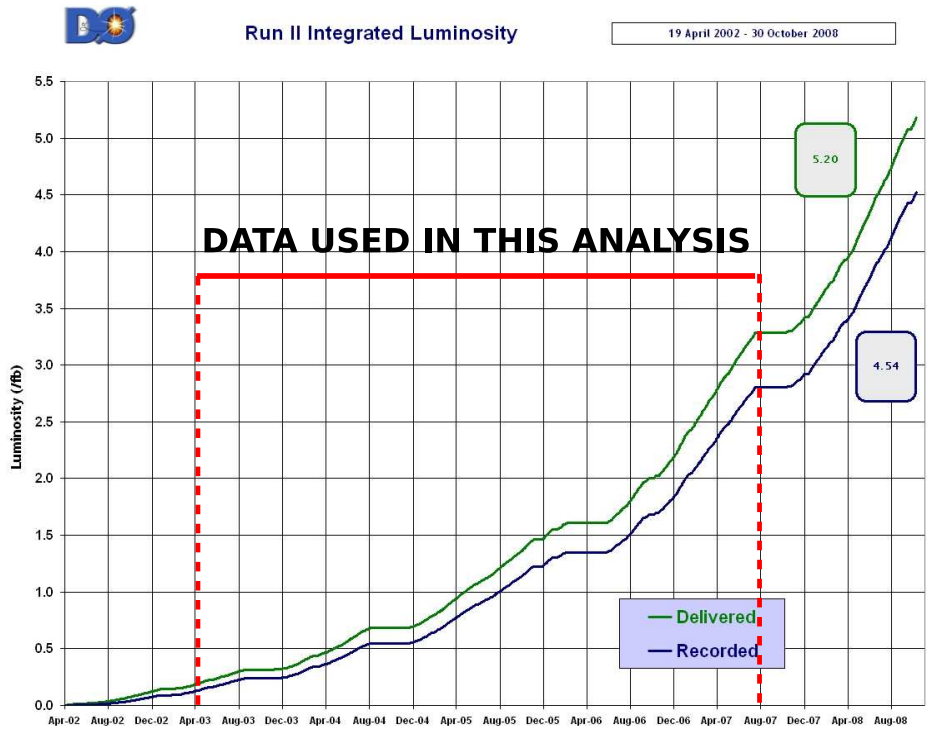

Figure 3.4: Delivered and recovered integrated luminosity for the DØ detector. For this dissertation, we use the integrated luminosity obtained from April 2003 to August 2007.

3.2 Monte Carlo Samples

Samples were generated using MCpythia [38] for the production and hadronization phase, and EvtGen [39] for decaying the "b" hadrons produced. DØ release p17.09.06 was used in all cases. All B_s^0 were forced to decay to $J/\psi + \phi$, and $J/\psi \to \mu^+\mu^-$, $\phi \to K^+K^-$, to save time. The EvtGen model to decay B_s^0 was SVV_HELAMP with default parameter that correspond to CP even states. We also generate a sample with CP-odd parameters and other with phase space model (e.g. no polarization or CP effects) for efficiency studies. Finally, an inclusive J/ψ sample is used for resolution studies.

The kinematic cuts applied to the samples (using dØ_mess) were: muons from J/ψ had to have $p_T > 4.0$ GeV and $|\eta| < 2.5$, and the kaons(pions) from $\phi(K^*)$ had to have $p_T > 0.3$ GeV. The sample was then processes using the standard full chain procedure DØ gstar-DØ sim-DØ reco.

Chapter 4

Distribution models and Fitting of data

From the description of the $B_d^0 \to J/\psi K^{*0}$ and $B_s^0 \to J/\psi\phi$ decays in Chapter 1.7, it is clear that we need to have the distributions for the angular variables $\boldsymbol{\omega}$ and the PDL ct. In order to do a better separation between the signal and the background entries, we will incorporate to our list of variables the invariant mass of the B meson under study. The distributions for the B_d^0 are shown in Appendix A.

In this Chapter we will describe the equations that will be used to model the distributions for the B_d^0 and the B_s^0 mesons. In addition to this, we will also describe the fitting method employed in these analyses and the measurements for the parameters involved in these descriptions.

4.1 Modeling the $B_d^0 \to J/\psi K^{*0}$ decay

4.1.1 Signal

Angular-mass model

The theoretical angular distribution for the $B_d^0 \to J/\psi K^{*0}$ is established in Eq. (1.69). However, in order to construct the correct angular distribution for this decay, we should

take into account the effect of the detector in the theoretical distribution. We denote by $\varepsilon(\boldsymbol{\omega})$ the efficiency of the detector, and it enters in the last equation in the following way:

$$\frac{d^4\mathcal{P}}{d\boldsymbol{\omega}dt} \propto e^{-\Gamma_d t}\sum_{i=1}^{10} g_i f_i(\boldsymbol{\omega}_j)\varepsilon(\boldsymbol{\omega}_j) \tag{4.1}$$

Since the way of describe the angular efficiency is somewhat empirical, we can model this function as the product of three normalized polynomials, each one as a function of one of the transversity variables, i.e.,

$$\varepsilon(\boldsymbol{\omega}) = p_1(\varphi)p_2(\cos\theta)p_3(\cos\psi). \tag{4.2}$$

The coefficients of this polynomials and the procedure to obtain them are in Appendix B.

As mentioned in section 1.7.2, we need to take into account that we are unable to distinguish completely the kaon and the pion in the decay $K^{*0} \to K^{\pm}\pi^{\mp}$. Since this could have an important effect on the angular distribution (due to the definition of the axes and the angular variables in terms of the daughter particles), we should also need to model this effect. The procedure to take this into account is described in Appendix C. From the MC studies, we have found that in about $f_{sw_A} = 13\%$ of the signal candidates, the candidate with the wrong mass assignment passes our selection algorithm.

As a result, our original set of transversity variables $\boldsymbol{\omega}$ suffers a change in their definition, and we denote this new set by $\boldsymbol{\omega}_{sw}$. With this in mind, our angular signal can be described as follows: the $1 - f_{sw}$ of our signal will correspond to our *unswapped* signal, and it will be modeled using Eq. (1.69). The rest of our signal, corresponding to the *swapped* signal, will be modeled in the following way:

- Since we have the set $\boldsymbol{\omega}_{sw}$, the functions f_i will be evaluated in this set of swapped transversity variables, i.e., $f_i(\boldsymbol{\omega}_{sw})$.

- We will now have a new function of efficiency denoted by $\varepsilon_{sw}(\boldsymbol{\omega})$, i.e., we are assuming that the information of the incorrect assignment of the masses is in the form of the

function, and we will evaluate it in the unswapped variables.

- We do not consider an S-wave contribution to the swap component.

The swap of the mass of the final products of the K^{*0} decay has an implication in the modeling of the mass too, not only in the angular distribution. So, it is also necessary to construct two functions that describe both components of the mass distribution. For the signal unswapped, we write a Gaussian as the PDF, i.e., we write

$$M_{sig}(\mu, \sigma\ ;\ m_j) = \frac{1}{\sqrt{2\pi}\sigma} \exp\left[-\frac{(m_j-\mu)^2}{2\sigma^2}\right]. \tag{4.3}$$

where the free parameters are the mean μ and the width σ of the Gaussian distribution.

Our Monte Carlo mass distributions for swap candidates suggest that the model for the swap mass consists of two Gaussian with fixed and different widths as follows:

$$\begin{aligned} M_{sig,sw}(\mu\ ;\ m_j) &= \frac{(1-f_w)}{N_n} G(m_j - \mu - \Delta M_{sw}, \sigma_n) \\ &+ \frac{f_w}{N_w} G(m_j - \mu - \Delta M_{sw}, \sigma_w) \end{aligned} \tag{4.4}$$

where the only free parameter is the mean μ of the Gaussians, which is the same mean as that in Eq. (4.3); f_w is the fraction of the wide component, ΔM_{sw} is the offset of the swapped Gaussian with respect to the unswapped Gaussian, $\sigma_w(\sigma_n)$ is the width of the wide(narrow) Gaussian, and

$$N_{n,w} = \frac{1}{2}\ \mathrm{Erf}\left[\frac{m-\mu-\Delta M_{sw}}{\sqrt{2}\ \sigma_{n,w}}\right]\Bigg|_{m=5.1605}^{m=5.3855} \tag{4.5}$$

are the normalization factors. All this numbers are calculated from Monte Carlo, and are fixed in the fit (see appendix B).

With all this in mind, the complete angular-mass signal PDF for this decay is given by

$$\begin{aligned} \mathcal{G}(|A_0|, |A_\parallel|, \delta_1, \delta_2, \mu, \sigma\ ;\ \boldsymbol{\omega}_j, m_j) &= \frac{1}{N_{d,sig}} \Bigg[(1-f_{sw}) M_{sig}(\mu, \sigma\ ;\ m_j) \sum_{i=1}^{10} g_i f_i(\boldsymbol{\omega}_j) \\ &+ f_{sw} M_{sw}(\mu\ ;\ m_j) \sum_{i=1}^{6} g_i f_i(\boldsymbol{\omega}_{j_{sw}}) R(\boldsymbol{\omega}_j)\Bigg] \varepsilon(\boldsymbol{\omega}_j) \end{aligned} \tag{4.6}$$

where the normalization factor for all the angular-mass distribution,$N_{d,sig}$, is given by

$$N_{d,sig} = \sum_{i=1}^{10} g_i \left[(1 - f_{sw})\xi_i + f_{sw}\xi_i^{sw}\right] \tag{4.7}$$

and

- f_{sw} is the fraction of swap events into the signal (calculated from Monte Carlo and fixed in the fit),

- $R(\boldsymbol{\omega}_j) = \varepsilon_{sw}(\boldsymbol{\omega}_j)/\varepsilon(\boldsymbol{\omega}_j)$ is a product of three normalized polynomials (see appendix B), and

- ξ_i and ξ_i^{sw} represent the normalization factors for the unswapped and swapped angular signal, respectively, and are related to the efficiency polynomials via the integrals

$$\xi_i = \int_{\boldsymbol{\omega}} d\boldsymbol{\omega} f_i(\boldsymbol{\omega})\varepsilon(\boldsymbol{\omega}) \tag{4.8}$$

$$\xi_i^{sw} = \int_{\boldsymbol{\omega}} d\boldsymbol{\omega} f_i(\boldsymbol{\omega}_{sw})R(\boldsymbol{\omega})\varepsilon(\boldsymbol{\omega}) \tag{4.9}$$

  which are calculated by Monte Carlo methods (see appendix B).

Proper Decay Length Model.

From the distributions showed in Appendix A, we model the proper decay length (PDL) distribution for the signal as an exponential decay

$$E(c\tau_d \,;\, ct_j) = \begin{cases} 0 & , \quad ct_j < 0 \\ \frac{1}{c\tau_d}\, e^{-ct_j/c\tau_d} & , \quad ct_j \geq 0 \end{cases} \tag{4.10}$$

convoluted with the PDL resolution function, assumed to be *two* weighted Gaussians

$$\mathrm{Res}(s_1, s_2, f_g \,;\, ct_j, \sigma_{ct_j}) = f_g G(s_1 \,;\, ct_j, \sigma_{ct_j}) + (1 - f_g)G(s_2 \,;\, ct_j, \sigma_{ct_j}) \tag{4.11}$$

where

$$G(s_i\ ;\ ct_j, \sigma_{ct_j}) = \frac{1}{\sqrt{2\pi s_i^2 \sigma_{ct_j}^2}}\ e^{-(ct_j)^2/(2s_i^2\sigma_{ct_j}^2)} \tag{4.12}$$

i.e.,

$$\mathcal{T}_{sig}(c\tau_d, s_1, s_2\ ;\ ct_j, \sigma_{ct_j}) = E(c\tau_d\ ;\ ct_j) \otimes \mathrm{Res}(s_1, s_2\ ;\ ct_j, \sigma_{ct_j}) \tag{4.13}$$

where

- ct_j is the PDL measurement for each event,
- σ_{ct_j} is the error for the PDL measurement,
- $c\tau_d$ is the lifetime of the B^0_d, and
- s_i is the correction factor to the error σ_{ct_j} that accounts for possible underestimate of the errors in the data
- f_g is the relative fraction between the two Gaussians.

4.1.2 Background

PDL model

We describe the PDL background as two separate components: the prompt component modeled by the same resolution as in the Eq. (4.11)

$$\mathcal{T}^p_{bg}(s, \lambda_+, \lambda_-, f_+, f_-\ ;\ ct_j, \sigma_{ct_j}) = (1 - f_{++} - f_+ - f_-)\mathrm{Res}(s_1, s_2\ ;\ ct_j, \sigma_{ct_j}) \tag{4.14}$$

and the non prompt component modeled by the contribution of one short-lived exponential for $ct_j < 0$, and one short-lived and one long-lived exponentials for $ct_j > 0$

$$\mathcal{T}^{np}_{bg}(\lambda_{++}, f_{++}\ ;\ ct_j) = f_{++}E(\lambda_{++}\ ;\ ct_j) + f_+E(\lambda_+\ ;\ ct_j) + f_-E(\lambda_-\ ;\ -ct_j), \tag{4.15}$$

where:

- λ_{++} is the slope of the right exponential long lifetime,
- λ_{+} is the slope of the right exponential short lifetime,
- λ_{-} is the slope of the left exponential
- f_{++} is the fraction of events in the positive exponential with long lifetime,
- f_{+} is the fraction of events in the positive exponential with short lifetime, and
- f_{-} is the fraction of events in the negative exponential.

Angular model

In the same way as we did in the PDL model of the background, we describe the angular background as a prompt and no prompt components, *assuming that both have a shape like* in Eq. (1.69) with a different set of amplitudes: $|B_0^x|, |B_\parallel^x|, |B_\perp^x| = \sqrt{1-|B_0^x|^2-|B_\parallel^x|^2}$, the relative phases $\beta_\parallel^x = arg(B_\parallel^x), \beta_\perp^x = \arg(B_\perp^x)$, and similar parameters λ^x and δ_s^x, where x stands for the prompt (p) and non prompt (np) components. From this, we have for the angular background the following:

$$\mathcal{A}^x_{bg,B_d^0}(|B_0^x|, |B_\parallel^x|, \beta_\parallel^x, \beta_\perp^x, \lambda^x, \delta_s^x \ ; \ \boldsymbol{\omega}_j) = \sum_{i=1}^{10} h_i^x f_i(\boldsymbol{\omega}_j)\ \varepsilon(\boldsymbol{\omega}_j) \tag{4.16}$$

where the h_i^x are obtained just by interchange $|A_i|$ by the corresponding $|B_i^x|$ as well as the phases in g_i [see Eqs. (1.70)-(1.79)].

Mass model

Finally, we model the mass background with two negative exponentials, one for the prompt and one for the non-prompt components as follows:

$$\mathcal{M}^x_{bg}(b^x \ ; \ m_j) = \frac{b^x e^{-b^x m_j}}{e^{-b^x m_{min}} - e^{-b^x m_{max}}} \tag{4.17}$$

where $x = \{p, np\}$ and

- b^p and b^{np} are the free parameters to fit, and

- $m_{min}(m_{max})$ is the lower(upper) limit of the mass window.

Taking into account the above prompt and no prompt contributions, we write the complete background PDF in the following form:

$$\mathcal{J}_{bg,B_d^0}(|B_0^x|,|B_\parallel^x|,\beta_\parallel^x,\beta_\perp^x,\lambda^x,\delta_s^x,s,\lambda_{++},f_{++},\lambda_+,f_+,\lambda_-,f_-,b^x\ ;\ \boldsymbol{\omega}_j,ct_j,\sigma_{ct_j},m_j) = \frac{1}{N_{d,bg}} \times \left[\mathcal{T}_{bg}^p\mathcal{M}_{bg}^p\mathcal{A}_{bg}^p + \mathcal{T}_{bg}^{np}\mathcal{M}_{bg}^{np}\mathcal{A}_{bg}^{np}\right]\varepsilon(\boldsymbol{\omega}_j) \quad (4.18)$$

where the normalization factor $N_{d,bg}$ is

$$N_{d,bg} = \sum_{i=1}^{10}\left[(1-f_{np})\,h_i^p + f_{np}h_i^{np}\right]\xi_i, \quad (4.19)$$

$f_{np} = f_{++} + f_+ + f_-$ is the fraction of events for the non prompt component, and the ξ_i are the same as in Eq. (4.8).

4.2 Modeling the $B_s^0 \to J/\psi\phi$

4.2.1 Signal

Angular-PDL model

For the $B_s^0 \to J/\psi\phi$ decay, the theoretical time-dependent angular behavior was established in Eq. (1.54). However, as we did it with the B_d^0 meson, we need to take into account the effects of the detector for this decay. We take the same model for the efficiency as in the B_d^0 −i.e., a product of three polynomials, each one depending on one of the angular variables− but with different coefficients from those of the B_d^0. The coefficients for the efficiency for the B_s^0 meson are reported in Appendix B.

After introduce the detector effects on Eq. (1.54), the angular-PDL distribution for the

signal of the $B_s^0 \to J/\psi\phi$ decay is given by

$$\mathcal{F}_{sig}(|A_0|, |A_\parallel|, \delta_\parallel, c\tau_L, c\tau_H, s_1, s_2 \,;\, \boldsymbol{\omega}_j, ct_j, \sigma_{ct_j}) = \frac{1}{N_{s,sig}} \left[\Omega_L + \Omega_H\right] \epsilon_s(\boldsymbol{\omega}_j) \tag{4.20}$$

where

$$\begin{aligned} \Omega_L &= c\tau_L \mathcal{T}_{sig}(c\tau_L, s_1, s_2, f_g \,;\, ct_j, \sigma_j) \sum_{i=1,2,5} k_i f_i(\boldsymbol{\omega}_j), \\ \Omega_H &= c\tau_H \mathcal{T}_{sig}(c\tau_H, s_1, s_2, f_g \,;\, ct_j, \sigma_j) k_3 f_3(\boldsymbol{\omega}_j), \end{aligned}$$

the normalization factor $N_{s,sig}$ is

$$N_{s,sig} = c\tau_L \sum_{i=1,2,5} k_i \xi_i^{B_s} + c\tau_H k_3 \xi_3^{B_s} \tag{4.21}$$

and

- $\epsilon_s(\boldsymbol{\omega}) = q_1(\varphi) q_2(\cos\theta) q_3(\cos\psi)$ is the normalized efficiency function for B_s^0,
- The integrals

$$\xi_i^{B_s} = \int_{\boldsymbol{\omega}} d\boldsymbol{\omega} f_i(\boldsymbol{\omega}) \epsilon_s(\boldsymbol{\omega}) \tag{4.22}$$

  are calculated by Monte Carlo methods,

- $c\tau_L (c\tau_H)$ is the light(heavy) lifetime, and
- $\mathcal{T}_{sig}$ was defined previously in eq. (4.13).

In our final distribution for this decay, we will replace $c\tau_L$ and $c\tau_H$ by the parameters $\Delta\Gamma_s$ and τ, which are related by the expressions

$$\Delta\Gamma_s = \frac{\tau_H - \tau_L}{\tau_L \tau_H} \tag{4.23}$$

$$\bar{\tau}_s = \frac{2\tau_L \tau_H}{\tau_L + \tau_H} \tag{4.24}$$

Mass model

We use a Gaussian like in Eq. (4.3).

4.2.2 Background

For the B_s^0 background, we also separate in two contributions as in the B_d^0, the prompt and non prompt components.

For the PDL and mass background models, we use the same as in the B_d^0 (see subsection 4.1.2).

Angular model

For the angular background we follow the same idea as in the $B_d^0 \to J/\psi K^{*0}$ decay: we model it with the same shape as in the signal. With this in mind, the angular background PDF is given by

$$\mathcal{A}^x_{bg,B_s^0}(|B_0|^x, |B_{||}|^x, \beta^x_{||}\ ;\ \boldsymbol{\omega}_j) = \sum_{i=1,2,3,5} j_i^x f_i(\boldsymbol{\omega}_j)\ \epsilon_s(\boldsymbol{\omega}_j) \tag{4.25}$$

where,

$$j_1^x = |B_0^x|^2 \tag{4.26}$$

$$j_2^x = |B_\parallel^x|^2 \tag{4.27}$$

$$j_3^x = |B_\perp^x|^2 \tag{4.28}$$

$$j_5^x = |B_0^x||B_\parallel^x| \cos\beta_\parallel \tag{4.29}$$

The final PDF background for the $B_s^0 \to J/\psi\phi$ is then given by

$$\mathcal{J}_{bg,B_s^0}(|B_0^x|, |B_\parallel^x|, \beta_\parallel^x, s, \lambda_{++}, f_{++}, \lambda_+, f_+, \lambda_-, f_-, b^x\ ;\ \boldsymbol{\omega}_j, ct_j, \sigma_{ct_j}, m_j) = \frac{1}{N_{s,bg}} \times \left[\mathcal{T}^p_{bg}\mathcal{M}^p_{bg}\mathcal{A}^p_{bg,B_s^0} + \mathcal{T}^{np}_{bg}\mathcal{M}^{np}_{bg}\mathcal{A}^{np}_{bg,B_s^0}\right]\epsilon_s(\boldsymbol{\omega}_j) \tag{4.30}$$

where

$$N_{s,bg} = c\tau_L \left(1 - f_{np}\right) \sum_{i=1,2,5} j_i^p \xi_i^{B_s^0} + c\tau_H f_{np} h_3^{np} \xi_3^{B_s^0}, \tag{4.31}$$

4.3 Fitting method

The method we used for both analyses is the 5-dimensional fit [26, 27] over all the mass windows for each candidate applied to the log-likelihood functions for the B_d^0 and B_s^0 mesons. Other methods such as the fixed background and simultaneous fit [28, 29] have been proved that are equivalent to the one we will use here.

For the $B_d^0 \to J/\psi K^{*0}$, the log-likehood function is as follows

$$L = \sum_{j=1}^{N} \ln \left[x_s \mathcal{G}_{sig} \mathcal{T}_{sig} + (1 - x_s) \mathcal{J}_{bg,B_d^0} \right] \tag{4.32}$$

where $\mathcal{G}_{sig}$, $\mathcal{T}_{sig}$, and $\mathcal{J}_{sig}$ are defined in Eqs. (4.6), (4.13), and (4.18), respectively; and x_s is the signal fraction, which is a free parameter in the fit.

The log-likelihood function to describe the $B_s^0 \to J/\psi\phi$ decay *restricted to no CP-violation* is

$$L = \sum_{j=1}^{N} \ln \left[x_s \mathcal{M}_{sig} \mathcal{F}_{sig} + (1 - x_s) \mathcal{J}_{bg,B_s^0} \right] \tag{4.33}$$

where $\mathcal{M}_{sig}$, $\mathcal{F}_{sig}$, and $\mathcal{J}_{bg,B_s^0}$ are defined in Eqs. (4.3), (4.20), and (4.30) respectively.

To do the fit and obtain the final measurements for the parameters, we used MIGRAD-HESSE-MINOS until the convergence of the fit was reached.

Chapter 5

The measurements

5.1 Measurements for the $B_d^0 \to J/\psi K^{*0}$ decay

The results of the fit for the $B_d^0 \to J/\psi K^{*0}$ are shown in Table 5.1. In Table 5.2 we show the correlations for the most important signal parameters.

Parameter	Measurement	Units	Parameter	Measurement	Units
$\|A_0\|^2$	0.587 ± 0.011	-	λ^-	90.2 ± 3.0	μm
$\|A_\parallel\|^2$	0.230 ± 0.013	-	f^-	1.44 ± 0.09	%
δ_1	-0.381 ± 0.06	rad	b^p	0.024 ± 0.011	-
δ_2	3.21 ± 0.06	rad	b^{np}	1.76 ± 0.03	-
λ	0.202 ± 0.032	rad	$\|B_0^p\|^2$	0.344 ± 0.003	-
δ_s	4.06 ± 0.14	rad	$\|B_\parallel^p\|^2$	0.368 ± 0.003	-
$c\tau_d$	424 ± 5.5	μm	$\beta_\parallel^p$	2.45 ± 0.01	rad
s_1	0.978 ± 0.005	-	$\beta_\perp^p$	-0.589 ± 0.008	rad
s_2	2.15 ± 0.03	-	λ^p	0.761 ± 0.004	rad
f_g	75.5 ± 0.7	%	δ_s^p	2.15 ± 0.008	rad
μ	5273.3 ± 0.6	MeV/c^2	$\|B_0^{np}\|^2$	0.492 ± 0.006	-
σ	38.40 ± 0.6	MeV/c^2	$\|B_\parallel^{np}\|^2$	0.261 ± 0.008	-
x_s	3.38 ± 0.05	%	$\beta_\parallel^{np}$	2.18 ± 0.03	rad
λ^{++}	409 ± 8.6	μm	$\beta_\perp^{np}$	2.44 ± 0.04	rad
f^{++}	3.34 ± 0.12	%	λ^{np}	0.536 ± 0.015	rad
λ^+	96.2 ± 1.4	μm	δ_s^{np}	1.62 ± 0.02	rad
f^+	12.3 ± 0.18	%			

Table 5.1: Measurements for the parameters of the $B_d^0 \to J/\psi K^{*0}$ decay.

	$\|A_0\|^2$	$\|A_\parallel\|^2$	δ_1	δ_2	$c\tau_d$
$\|A_0\|^2$	1.0	−0.410	−0.064	−0.001	0.011
$\|A_\parallel\|^2$	–	1.0	−0.072	0.079	0.005
δ_1	–	–	1.0	0.254	−0.001
δ_2	–	–	–	1.0	0.003
$c\tau_d$	–	–	–	–	1.0

Table 5.2: Correlation coefficients for the angular and lifetime parameters for B_d^0.

The projections for the invariant mass and PDL with the data from Table 5.1 are shown in Figs. 5.1 and 5.2.

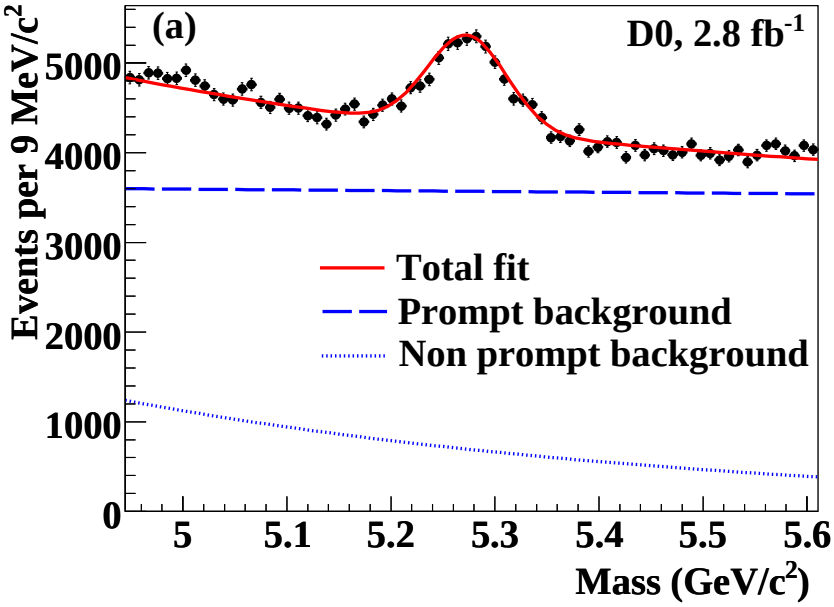

Figure 5.1: Invariant mass distribution for the B_d^0.The points with error bars represent the data, and the curves represent the fit projections for the total and the background components.

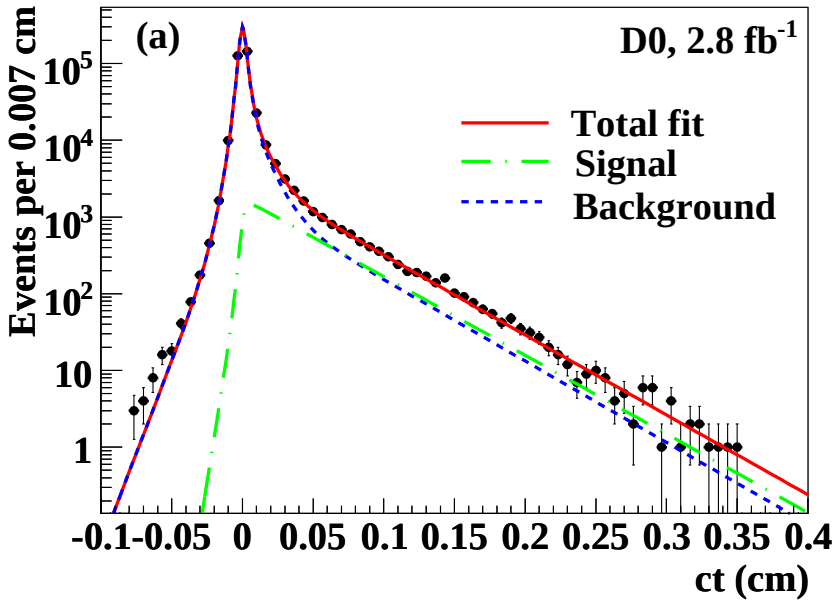

Figure 5.2: PDL distribution for the B_d^0.The points with error bars represent the data, and the curves represent the fit projections for the total and the background components.

5.2 Measurements for the $B_s^0 \to J/\psi\phi$ decay

The results of the fit for the B_s^0 are shown in Table 5.3. The correlation coefficients for the angular and lifetime parameters are reported in Table 5.4.

Parameter	Measurement	Units
$\Delta\Gamma$	$0.085^{+0.072}_{-0.078}$	ps^{-1}
$\bar{\tau}_s$	$1.487^{+0.060}_{-0.059}$	ps
s_1	0.992 ± 0.017	-
s_2	2.18 ± 0.09	-
f_g	75.4 ± 2.4	%
$\lvert A_0\rvert^2$	0.555 ± 0.027	-
$\lvert A_\parallel\rvert^2$	0.244 ± 0.032	-
$\delta_\parallel$	$2.72^{+1.12}_{-0.27}$	rad
μ	5362 ± 1.0	$\mathrm{MeV/c^2}$
σ	$29.3^{+1.0}_{-0.9}$	$\mathrm{MeV/c^2}$
x_s	4.62 ± 0.15	%
λ^{++}	399^{+26}_{-23}	μm
f^{++}	$3.56^{+0.42}_{-0.39}$	%
λ^{+}	$107^{+4.8}_{-4.7}$	μm
f^{+}	12.23 ± 0.51	%
λ^{-}	$126^{+13.4}_{-11.3}$	μm
f^{-}	$0.95^{+0.15}_{-0.16}$	%
b^p	0.195 ± 0.031	$(\mathrm{MeV}/c^2)^{-1}$
b^{np}	1.76 ± 0.1	$(\mathrm{MeV}/c^2)^{-1}$
$\lvert B_0^p\rvert^2$	0.340 ± 0.004	-
$\lvert B_{\lvert\rvert}^p\rvert^2$	0.296 ± 0.006	-
$\beta_{\lvert\rvert}^p$	1.98 ± 0.03	rad
$\lvert B_0^{np}\rvert^2$	0.383 ± 0.013	-
$\lvert B_{\lvert\rvert}^{np}\rvert^2$	0.298 ± 0.019	-
$\beta_{\lvert\rvert}^{np}$	1.81 ± 0.09	rad

Table 5.3: Nominal results for the $B_s^0 \to J/\psi\phi$ restricted to no CP-violation.

From Tables 5.1 and 5.3, we can get the values for the ratio $\bar{\tau}_s/\tau_d$ and obtain the corresponding errors by propagating it from those of τ_d ps and $\bar{\tau}_s$:

$$\bar{\tau}_s/\tau_d = 1.053 \pm 0.061$$

	$\Delta\Gamma$	τ	$\lvert A_0\rvert^2$	$\lvert A_\parallel\rvert^2$	$\delta_\parallel$
$\Delta\Gamma$	1.0	0.668	0.594	0.323	−0.005
τ	–	1.0	0.439	0.277	−0.053
$\lvert A_0\rvert^2$	–	–	1.0	−0.171	0.044
$\lvert A_\parallel\rvert^2$	–	–	–	1.0	−0.407
$\delta_\parallel$	–	–	–	–	1.0

Table 5.4: Correlation coefficients for the angular and lifetime parameters of B_s^0.

The projections for the invariant mass and PDL with the data from Table 5.3 are shown in Figs. 5.3 and 5.4, respectively.

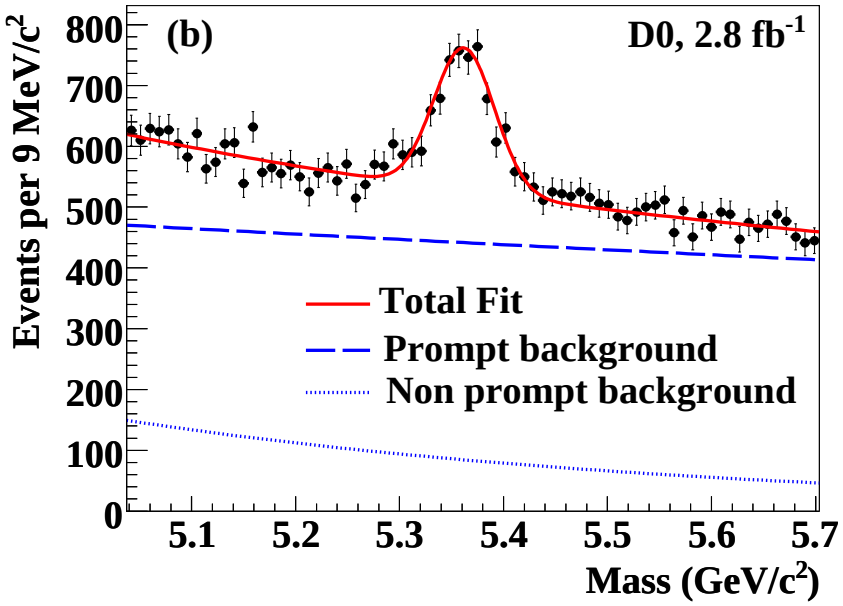

Figure 5.3: Invariant mass distribution for the B_s^0. The points with error bars represent the data, and the curves represent the fit projections for the total and the background components.

5.3 Systematic Uncertainties

In this section we will show only the systematic uncertainties that are most reliable to the measurements. We will explain the source of the systematic uncertainty and then report the systematic uncertainty as follows:

$$\sigma_{syst} = \text{mean}_{\alpha,nominal} - \text{mean}_{\alpha,ss} \tag{5.1}$$

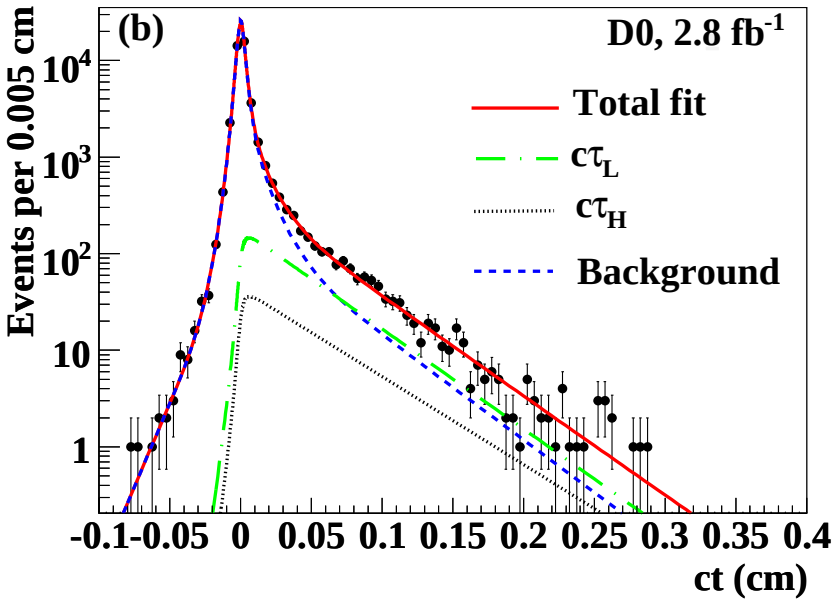

htbp

Figure 5.4: PDL distribution for the B_s^0. The points with error bars represent the data, and the curves represent the fit projections for the total and the background components.

where $\text{mean}_{\alpha,nominal}$ is the nominal measurement for any parameter α reported in Tables 5.1 or 5.3 and $\text{mean}_{\alpha,ss}$ is the measurement for source of systematic uncertainty for the same parameter α.

5.3.1 The mass background model

In both cases (the B_d^0 and B_s^0) we use two normalized negative exponentials -one for the prompt and other for the non prompt component- as our nominal model for the mass background. As a systematic uncertainty, we change the model to two (normalized) 1st-order polynomials, one for the prompt ($x = p$) and one for the non prompt ($x = np$), i.e.,

$$\mathcal{M}_{bg}^{x}\left(a_1^x, a_0^x\ ;\ m_j\right) = a_1^x m_j + a_0^x \tag{5.2}$$

where

$$a_0^x = \frac{1}{m_{max} - m_{min}}\left[1 - \frac{a_1^x}{2}\left(m_{max}^2 - m_{min}^2\right)\right] \tag{5.3}$$

The systematic uncertainties are reported in Tables 5.5 and 5.6, respectively.

Parameter	Systematic Uncertainty	Units
$\|A_0\|^2$	–	-
$\|A_\parallel\|^2$	± 0.024	-
δ_1	± 0.088	rad
δ_2	± 0.05	rad
$c\tau_d$	± 9.0	μm

Table 5.5: For B_d^0. Systematic uncertainties for each parameter due to the change in the mass background model.

Parameter	Systematic uncertainty	Units
$\Delta\Gamma$	–	ps^{-1}
$\bar{\tau}_s$	± 0.021	ps
$\|A_0\|^2$	± 0.004	-
$\|A_\parallel\|^2$	± 0.002	-
$\delta_\parallel$	± 0.02	rad

Table 5.6: For B_s^0. Systematic uncertainties of each parameter due to the change in the mass background model for the prompt component.

5.3.2 The PDL resolution model

To study the effect of uncertainties in our resolution model, we modified the functional form of eq. (4.11) to a single Gaussian weighted by the event-by-event PDL errors and a single scale factor s; i.e., now we use

$$\text{Res}(s\ ;\ ct_j, \sigma_j) = \frac{1}{\sqrt{2\pi}\sigma_{ct_j} s} e^{-\frac{ct_j^2}{2s^2\sigma_{ct_j}^2}} \tag{5.4}$$

The fitted values for the scale factors are reported in table 5.7.

Parameter	B_d^0	B_s^0	Units
s	1.12 ± 0.003	1.13 ± 0.008	-

Table 5.7: Fit results for the scale factors s for each decay

The systematic uncertainties due to the use of only one Gaussian as the resolution are reported in tables 5.8 and 5.9.

Parameter	Systematic Uncertainty	Units
$\|A_0\|^2$	± 0.013	-
$\|A_\parallel\|^2$	± 0.008	-
δ_1	± 0.020	rad
δ_2	± 0.03	rad
$c\tau_d$	± 4.0	μm

Table 5.8: For B_d^0. Systematic uncertainties due to use eq. (5.4) as the resolution model.

Parameter	Systematic Uncertainty	Units
$\Delta\Gamma$	$-$	ps^{-1}
τ	± 0.016	ps
$\|A_0\|^2$	± 0.005	-
$\|A_\parallel\|^2$	± 0.003	-
$\delta_\parallel$	$-$	rad

Table 5.9: For B_s^0. Systematic uncertainties of each parameter using eq. (5.4) in the resolution model.

5.3.3 The fitting procedure

To estimate the systematic due to the fitting procedure we generate 1,394 Toy MC samples for B_d^0 and 1,085 for B_s^0. If we are not introducing any bias to the measurement we should see the fitted values to those Toy MC samples equal to the corresponding input values. The values are reported in tables 5.10 and 5.11. The distributions and pulls of this studies are shown in figures 5.5-5.8. Since the difference between the samples are the cuts and no the fitting code, these systematic errors apply to the three sets.

	For B_d^0. Toy MC input and fitted values.			
Parameter	Input	Fitted value	Difference	Units
$\|A_0\|^2$	0.564	0.563 ± 0.0003	0.001	-
$\|A_\parallel\|^2$	0.265	0.265 ± 0.0004	$-$	-
δ_1	3.11	3.11 ± 0.003	$-$	rad
δ_2	0.283	0.285 ± 0.0025	0.002	rad
$c\tau$	438.4	437.2 ± 0.2	1.2	μm

Table 5.10: For B_d^0. Systematics due to fitting procedure.

	For B_s^0. Toy MC input and fitted values.			
Parameter	Input	Fitted value	Difference	Units
$\Delta\Gamma$	0.021	0.020 ± 0.003	0.001	ps^{-1}
τ	1.470	1.462 ± 0.002	0.008	ps
$\lvert A_0 \rvert^2$	0.527	0.523 ± 0.001	0.004	-
$\lvert A_\parallel \rvert^2$	0.211	0.225 ± 0.001	0.014	-
$\delta_\parallel$	3.44	3.71 ± 0.009	0.27	rad

Table 5.11: For B_s^0. Systematics due to fitting procedure.

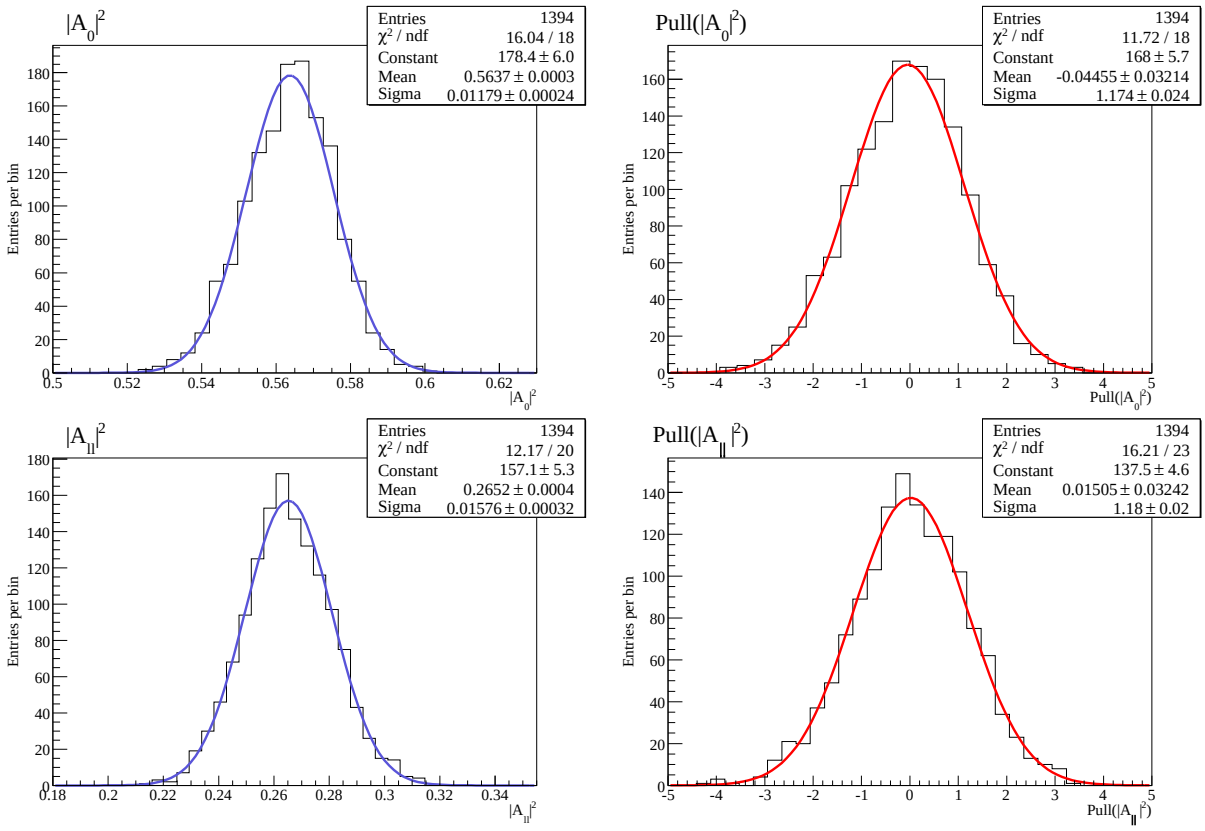

Figure 5.5: Distribution and pull of the fitted values for $|A_0|^2$ (top) and $|A_\parallel|^2$ (bottom) for B_d^0.

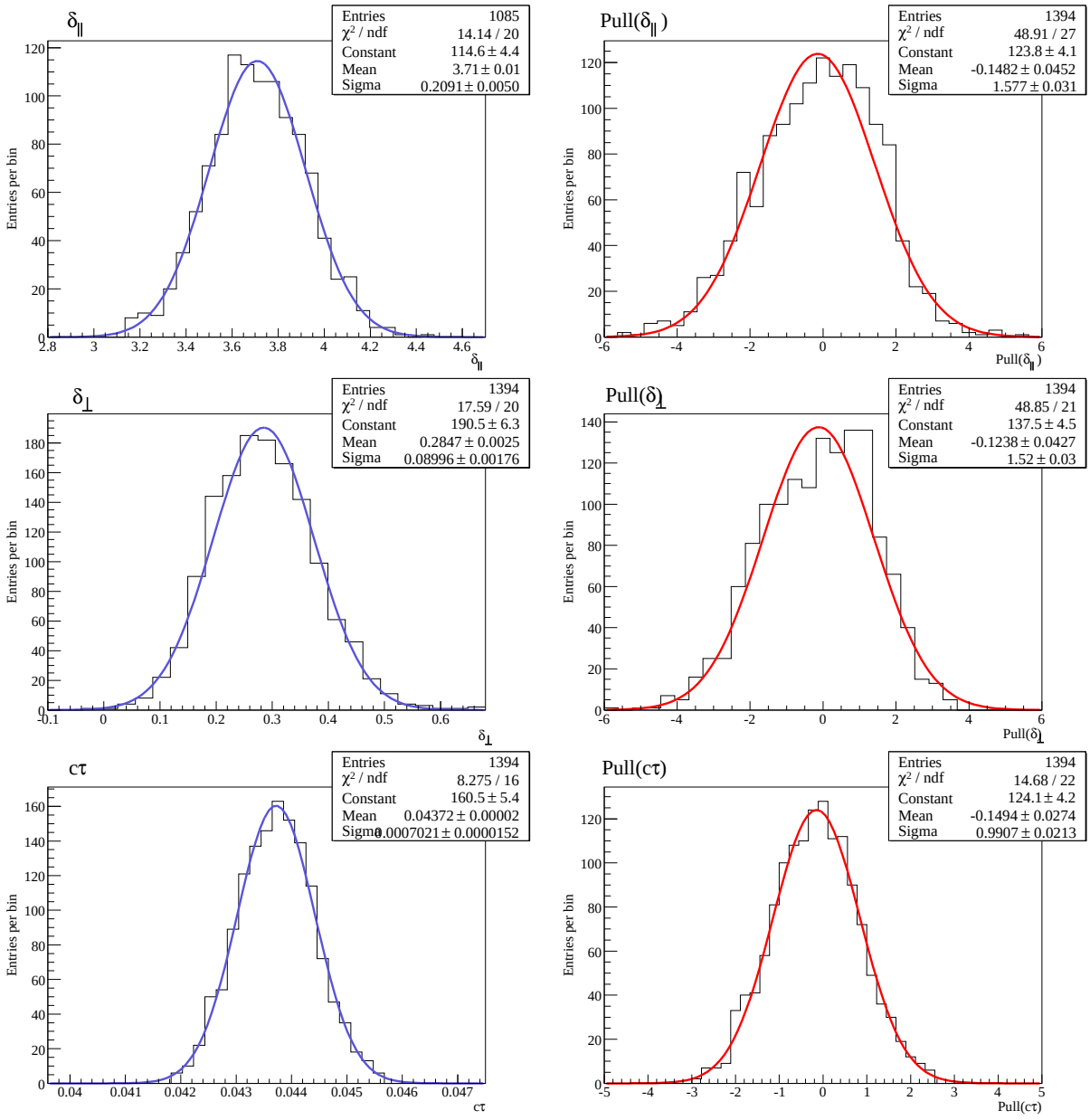

Figure 5.6: Distribution and pull of the fitted values for $\delta_{\parallel}$ (top), $\delta_{\parallel}$ (middle) and $c\tau$ (bottom) for B_d^0.

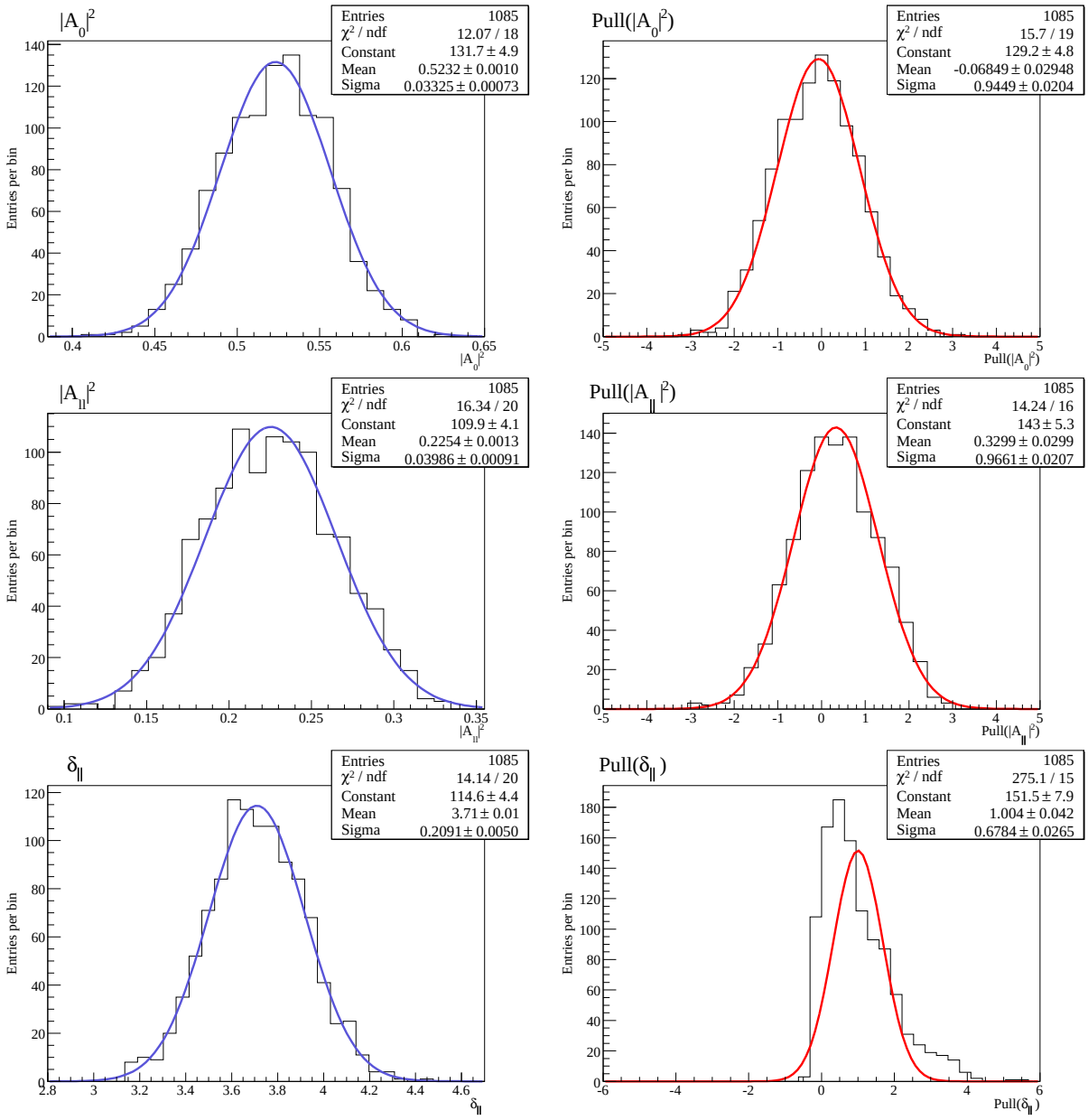

Figure 5.7: Distribution and pull of the fitted values for $|A_0|^2$ (top), $|A_\parallel|^2$ (middle) and $\delta_\parallel$ (bottom) for B_s^0.

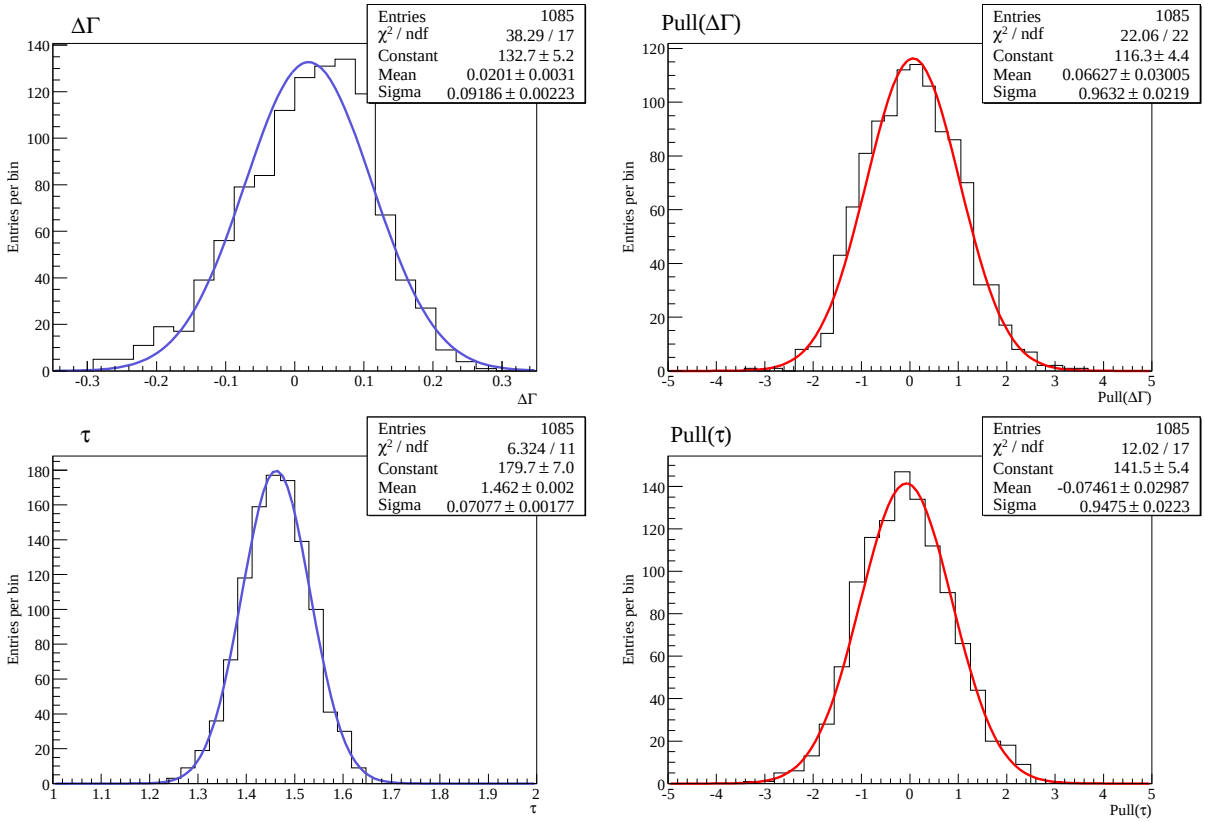

Figure 5.8: Distribution and pull of the fitted values for $\Delta\Gamma$ (top) and τ (bottom) for B_s^0.

Other sources of systematic uncertainties that gave negligible variations in measured parameters are the following:

- **Monte Carlo reweighting.** As mentioned in Appendix E, we do the reweighting for the MC using *only* the transverse momentum of J/ψ, $p_T(J/\psi)$. Instead of using only this momentum, we use both, the $p_T(J/\psi)$ and $p_T(K^{*0})$.

- **PDL background model.** We changed the nominal PDL background model (section 4.1.2) in the following ways:

  - We use only one component for $ct_j > 0$ and one component for $ct_j < 0$
  - We use two components for $ct_j > 0$ and two components for $ct_j < 0$
  - We use one component for $ct_j > 0$ and two components for $ct_j < 0$

- $K\pi$ **mass swap.** We vary the fraction of swap events as $f_{sw} = 13\% \pm 3\sigma$.

- S**-wave.** As reported in previous measurements of this phenomenon, the fix the value of $\lambda = 0$ in order to measure only the P-wave contribution.

5.3.4 Systematic uncertainties summary

In Tables 5.12 and 5.13 we summarize the systematic uncertainties for the $B_d^0 \to J/\psi K^{*0}$ and $B_s^0 \to J/\psi\phi$, respectively. The systematic uncertainties for the lifetime ratio $\bar{\tau}_s/\tau_d$ are obtained by evaluating a new value for each source reported above and do the difference with the nominal values reported in Table 5.14.

	Systematic uncertainties					
Parameter	fitting	resolution	mass bg	alignment	**Total**	Units
$\|A_0\|^2$	± 0.001	± 0.013	–	–	$\mathbf{\pm 0.013}$	–
$\|A_\parallel\|^2$	–	± 0.008	± 0.024	–	$\mathbf{\pm 0.025}$	–
δ_1	–	± 0.020	± 0.088	–	$\mathbf{\pm 0.090}$	rad
δ_2	–	± 0.03	± 0.05	–	$\mathbf{\pm 0.06}$	rad
$c\tau_d$	± 1.1	± 4.0	± 9.0	± 2.0	$\mathbf{\pm 10.1}$	μm

Table 5.12: Summary of systematic uncertainties for B_d^0. We take the alignment systematic uncertainty from the Refs. [29, 30]

	Systematic uncertainties					
Parameter	Fitting	resolution	mass bg	alignment	**Total**	Units
$\Delta\Gamma$	± 0.001	–	–	–	$\mathbf{\pm 0.001}$	%
τ	± 0.008	± 0.016	± 0.021	± 0.007	$\mathbf{\pm 0.028}$	μm
$\|A_0\|^2$	± 0.004	± 0.005	± 0.004	–	$\mathbf{\pm 0.006}$	–
$\|A_\parallel\|^2$	± 0.014	± 0.003	± 0.002	–	$\mathbf{\pm 0.014}$	–
$\delta_\parallel$	± 0.26	–	± 0.02	–	$\mathbf{\pm 0.26}$	rad

Table 5.13: Summary of systematics errors for B_s^0 (restricted case).

Parameter	Fitting	resolution	mass bg	alignment	**Total**	Units
$\bar{\tau}_s/\tau_d$	± 0.003	± 0.012	± 0.009	–	$\mathbf{\pm 0.015}$	–

Table 5.14: Summary of systematic errors for the ratio $\bar{\tau}_s/\tau_d$.

Chapter 6

Results and conclusions.

Using data equivalent to 2.8 fb^{-1}, we have measured all the angular and temporal parameters corresponding to the untagged analysis that describe the decays $B_d^0 \to J/\psi K^{*0}$ and $B_s^0 \to J/\psi\phi$ in the transversity basis. For the former, we obtain the results reported in Table 6.1, and for the latter, the measurements are reported in table 6.2. For the ratio $\bar{\tau}_s/\tau_d$, the final measurement is reported in Table 6.3.

Parameter	Final measurement	Units
$\|A_0\|^2$	$0.587 \pm 0.011\,(\text{stat}) \pm 0.013\,(\text{syst})$	-
$\|A_\parallel\|^2$	$0.230 \pm 0.013\,(\text{stat}) \pm 0.025\,(\text{syst})$	-
δ_1	$-0.381^{+0.060}_{-0.061}\,(\text{stat}) \pm 0.090\,(\text{syst})$	rad
δ_2	$3.21 \pm 0.06\,(\text{stat}) \pm 0.06\,(\text{syst})$	rad
$c\tau$	$424 \pm 5.5\,(\text{stat}) \pm 10.1\,(\text{syst})$	μm
x_s	3.38 ± 0.05	%
Total Entries	$334,199$	-
Signal Entries	$11,816 \pm 181$	-

Table 6.1: Final measurements for B_d^0 parameters.

Parameter	Final measurement	Units
$\Delta\Gamma$	$0.085^{+0.072}_{-0.078}\,(\text{stat}) \pm 0.001$	ps^{-1}
τ	$1.487^{+0.060}_{-0.059}\,(\text{stat}) \pm 0.028$	ps
$\lvert A_0\rvert^2$	$0.555 \pm 0.027\,(\text{stat}) \pm 0.006$	-
$\lvert A_\parallel\rvert^2$	$0.244 \pm 0.032\,(\text{stat}) \pm 0.014$	-
$\delta_\parallel$	$2.72^{+1.12}_{-0.27}\,(\text{stat}) \pm 0.26$	rad
x_s	4.62 ± 0.15	%
Total Entries	$41,691$	-
Signal Entries	$1,964 \pm 63$	-

Table 6.2: Nominal results for B_s^0 restricted to no CP-violation.

Parameter	Final measurement	Units
$\bar{\tau}_s/\tau_d$	$1.053^{+0.062}_{-0.061}\,(\text{stat}) \pm 0.015\,(\text{syst})$	-

Table 6.3: Nominal measurement for the ratio $\bar{\tau}_s/\tau_d$

6.1 Conclusions for the decay $B_d^0 \to J/\psi K^{*0}$.

Comparison with other experiments

We can compare the results obtained in this study with other ones reported in literature, as is shown in Table 6.4.

Experiment	$\lvert A_0\rvert^2$	$\lvert A_\parallel\rvert^2$	δ_1 (rad)	δ_2 (rad)
CDF	$0.569 \pm 0.009 \pm 0.009$	$0.211 \pm 0.012 \pm 0.006$	$-0.343 \pm 0.02 \pm 0.03$	$2.97 \pm 0.06 \pm 0.01$
BaBar	$0.556 \pm 0.009 \pm 0.010$	$0.211 \pm 0.010 \pm 0.006$	$-0.593 \pm 0.03 \pm 0.07$	$2.96 \pm 0.07 \pm 0.05$
BELLE	$0.574 \pm 0.012 \pm 0.009$	$0.231 \pm 0.012 \pm 0.008$	$-0.458 \pm 0.03 \pm 0.01$	$2.94 \pm 0.06 \pm 0.01$
DØ	$0.587 \pm 0.011 \pm 0.013$	$0.230 \pm 0.013 \pm 0.025$	$-0.381^{+0.060}_{-0.061} \pm 0.090$	$3.21 \pm 0.06 \pm 0.06$

Table 6.4: Comparison of angular parameters with other experiments for $B_d^0 \to J/\psi K^{*0}$. Measurements from CDF, BaBar, and Belle are reported in References [4, 16, 31] respectively. The uncertainties are in the conventional order: statistical and systematic.

As can be seen in this table, our values are consistent and the errors are competitive with B factories. This can be seen easily in the Fig. 6.1.

6.1.1 Final-state interactions in the decay $B_d^0 \to J/\psi K^{*0}$?

From theory [13, 17], in the absence of strong-final state interactions, the values of the phases δ_1 and δ_2 should be 0 (mod π). From our measurements, we conclude that there are final

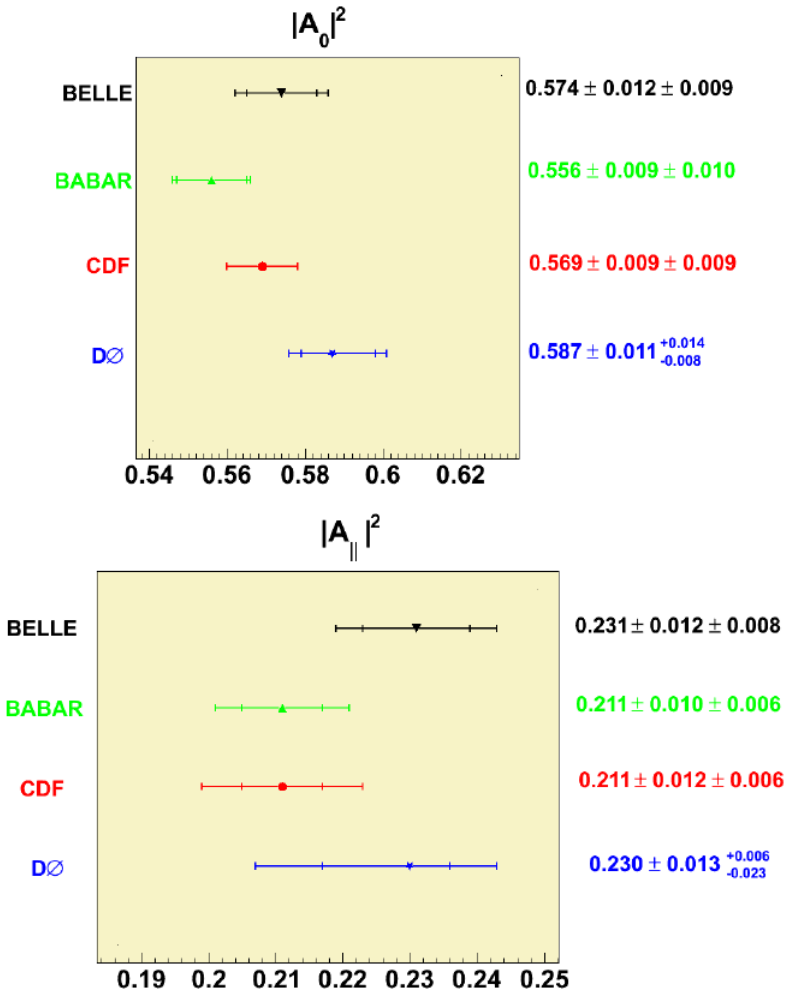

Figure 6.1: Comparison of the measurements of the angular amplitudes with other experiments

state interactions in this decay since our value of δ_1 is[1] $3.5\sigma_T$ away from the theoretical prediction. This is the first measurement of this phenomena at DØ .

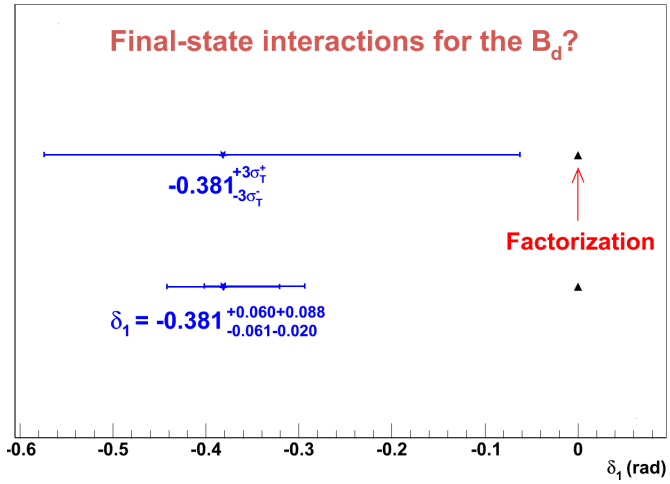

Figure 6.2: Comparison of the measurements of the strong phase δ_1 with mod(π) in order to know if our measurement establish (or not) the existence of the final-state interactions in the decay $B_d^0 \to J/\psi K^{*0}$.

6.2 Conclusions for both decays.

6.2.1 SU(3) symmetry for this decays?

From theory [13, 20], if the amplitudes of both decays are consistent we can say that SU(3) holds for these mesons. Now, as can be seen from Tables 6.1 and 6.2, we can establish whether the SU(3) symmetry holds or is broken for these two mesons. We show this in the Fig. 6.3. We conclude that the SU(3) symmetry holds for these decays.

6.2.2 Ratio of τ_s/τ_d

From the values reported in Tables 6.1 and 6.2, we found

$$\frac{\bar{\tau}_s}{\tau_d} = 1.053 \pm 0.061\,(\text{stat}) \pm 0.015\,(\text{syst}) \tag{6.1}$$

[1] $\sigma_T^2 = \sigma_{stat}^2 + \sigma_{syst}^2$

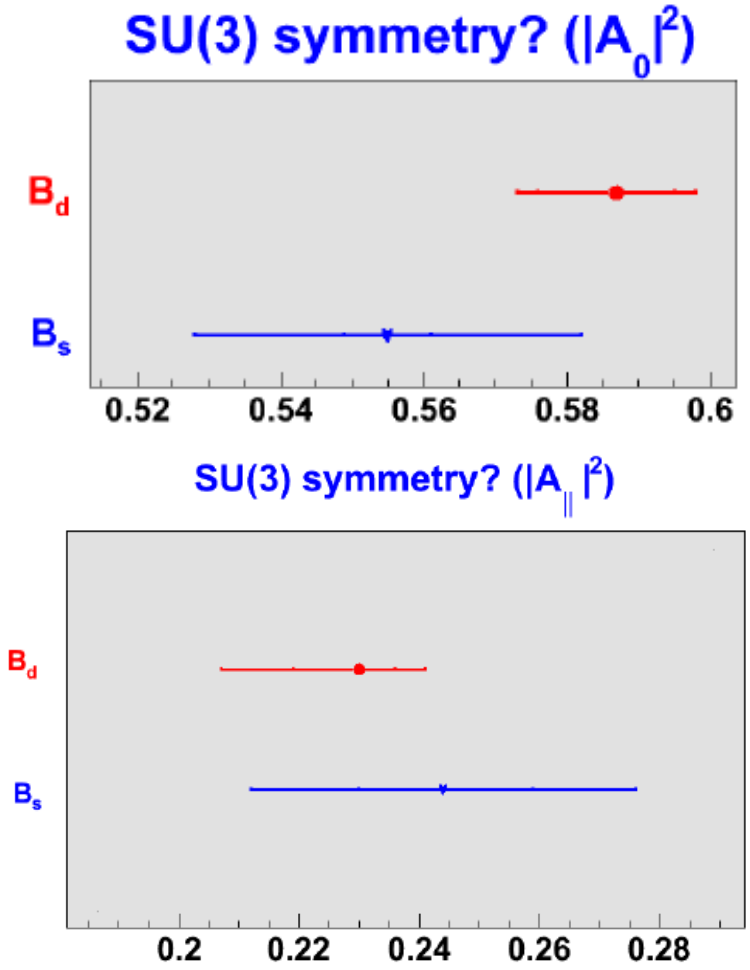

Figure 6.3: Comparison of angular parameters in order to know if SU(3) symmetry is broken in these decays.

It is important to mention here that theory [3, 5] has a prediction of

$$\frac{\tau_s}{\tau_d} = 1.00 \pm 0.01 \tag{6.2}$$

Our measurements are consistent with theory and with the ones reported in literature [7]. A comparison with theory and CDF can be seen in Fig. 6.4.

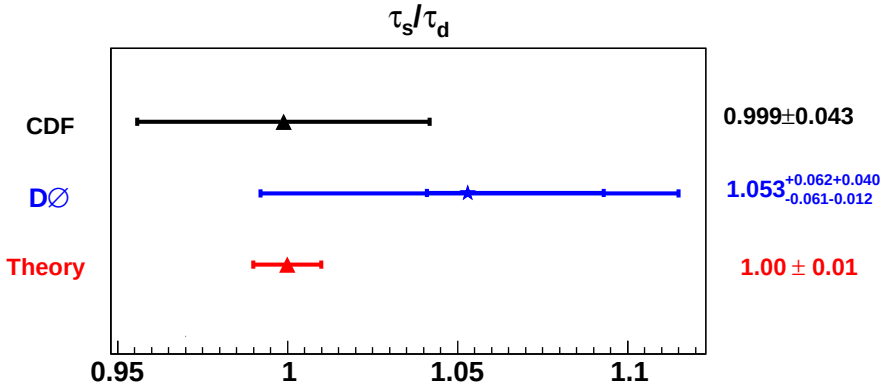

Figure 6.4: Comparison of the measurement for the lifetime ratio with theory and CDF.

Appendix A

Variable distributions

A.1 B_d^0

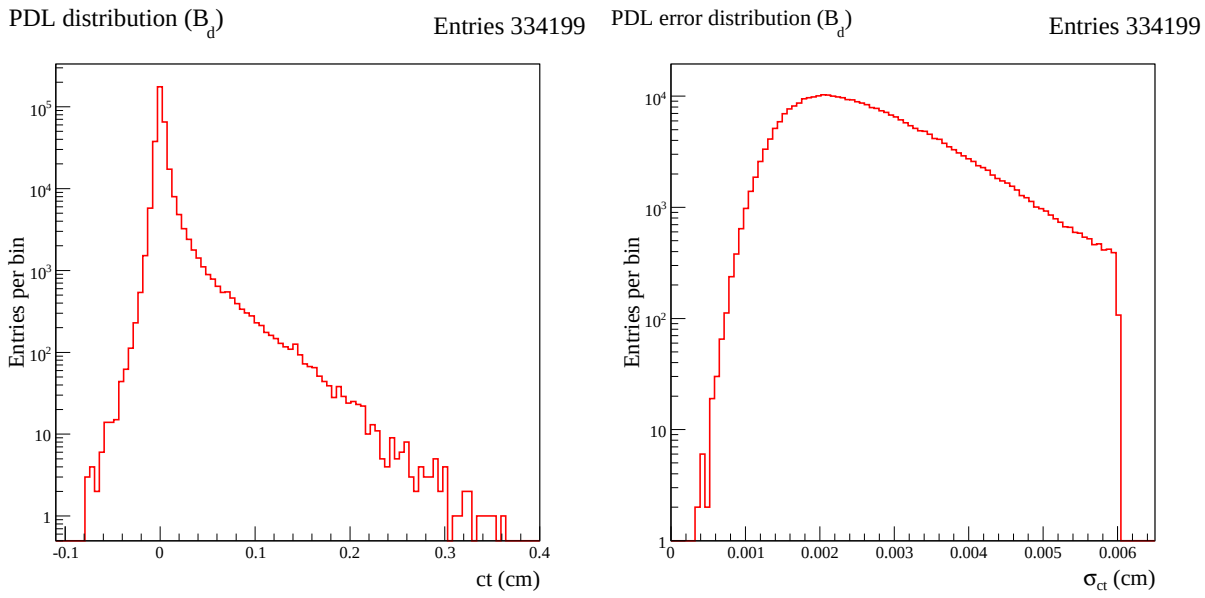

Figure A.1: Variable distributions for the PDL ct (left) and PDL error σ_{ct} (right) for the $B_d^0 \to J/\psi K^{*0}$.

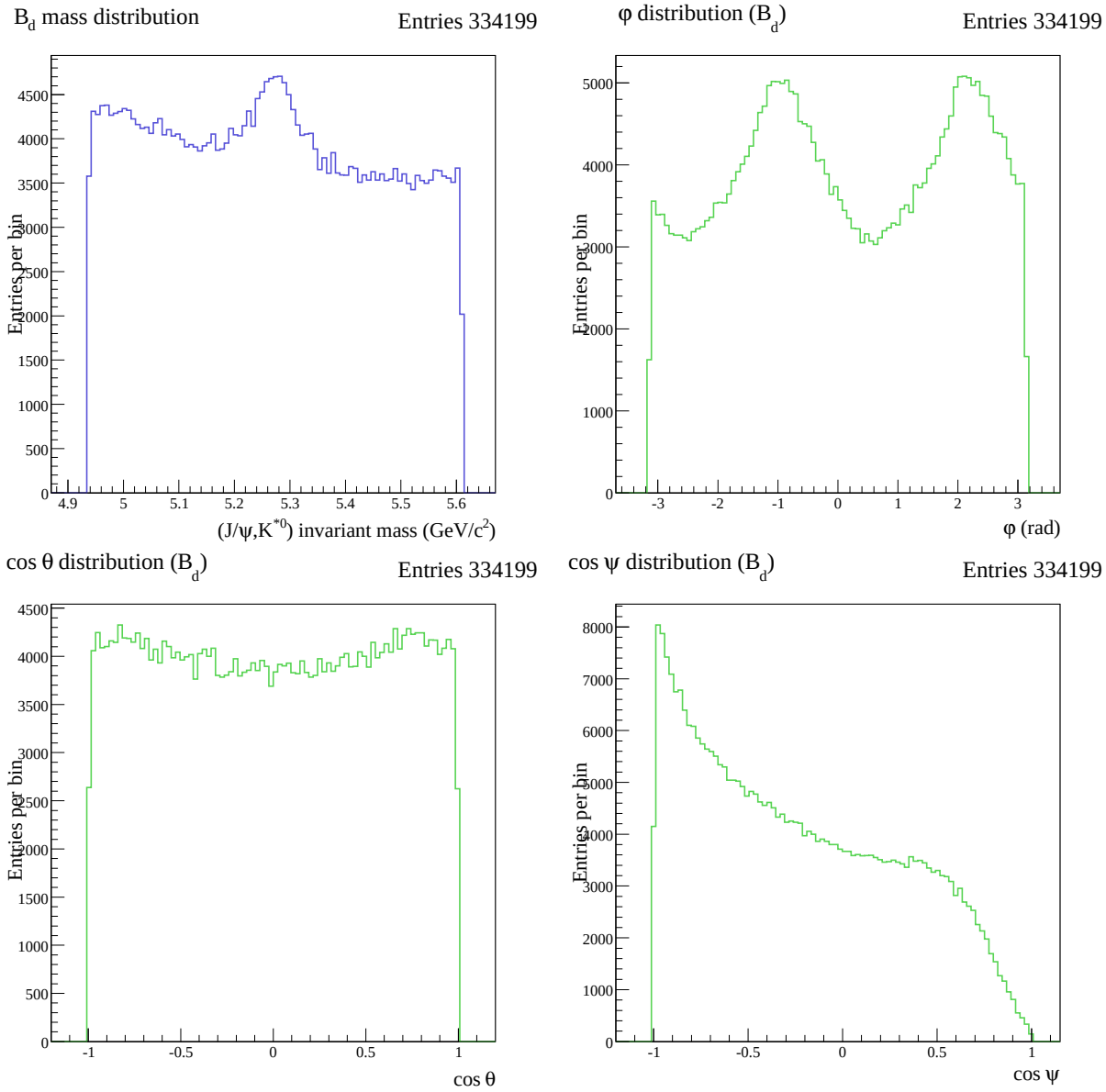

Figure A.2: Variable distributions for the mass (top left) and the angular variables ϕ (top right), $\cos\theta$ (bottom left), and $\cos\psi$ (bottom right) for the $B_d^0 \to J/\psi K^{*0}$.

A.2 B_s^0

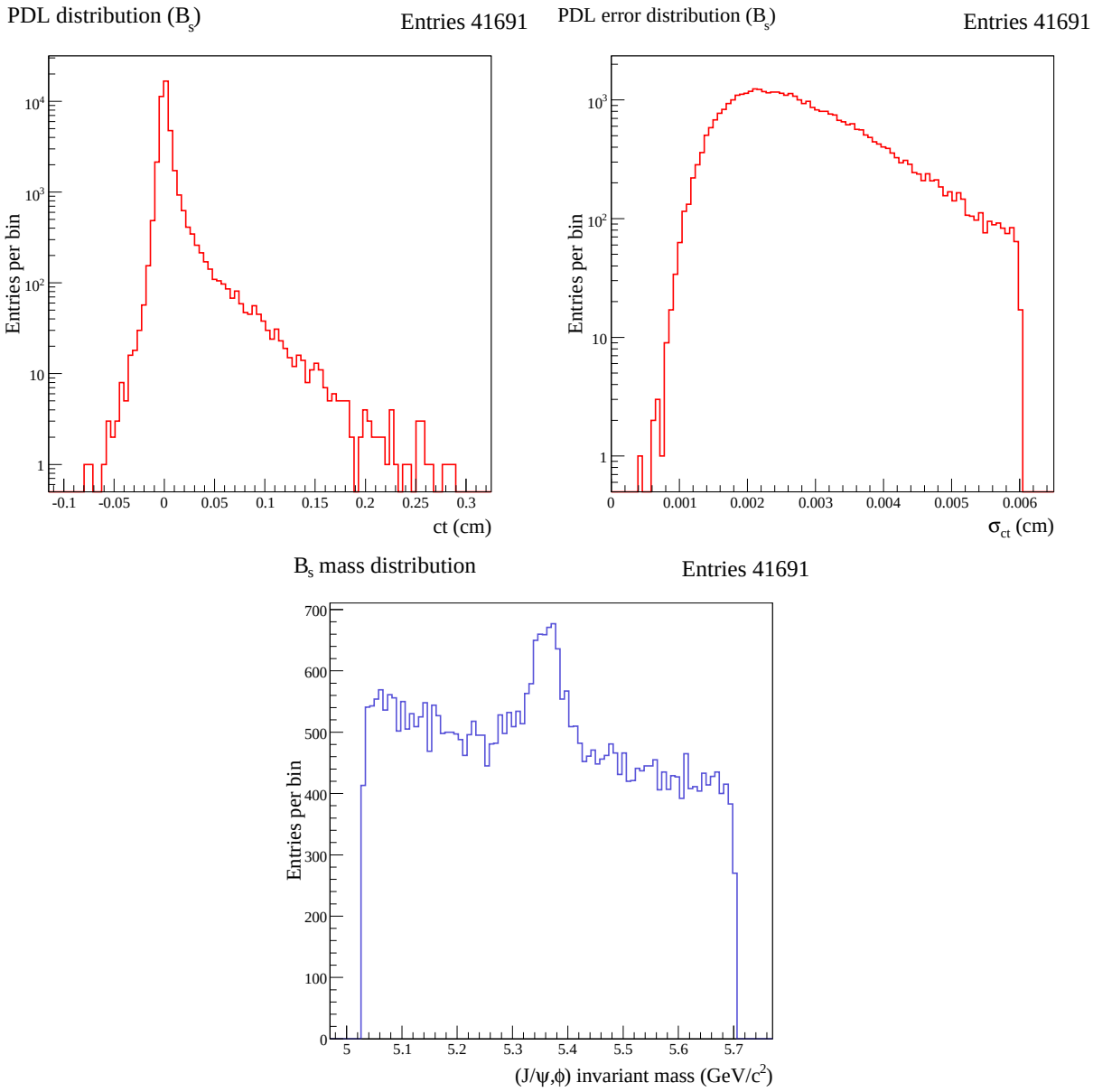

Figure A.3: Variable distributions for the PDL ct (top left), PDL error σ_{ct} (top right) and the mass m (bottom) for the $B_s^0 \to J/\psi\phi$.

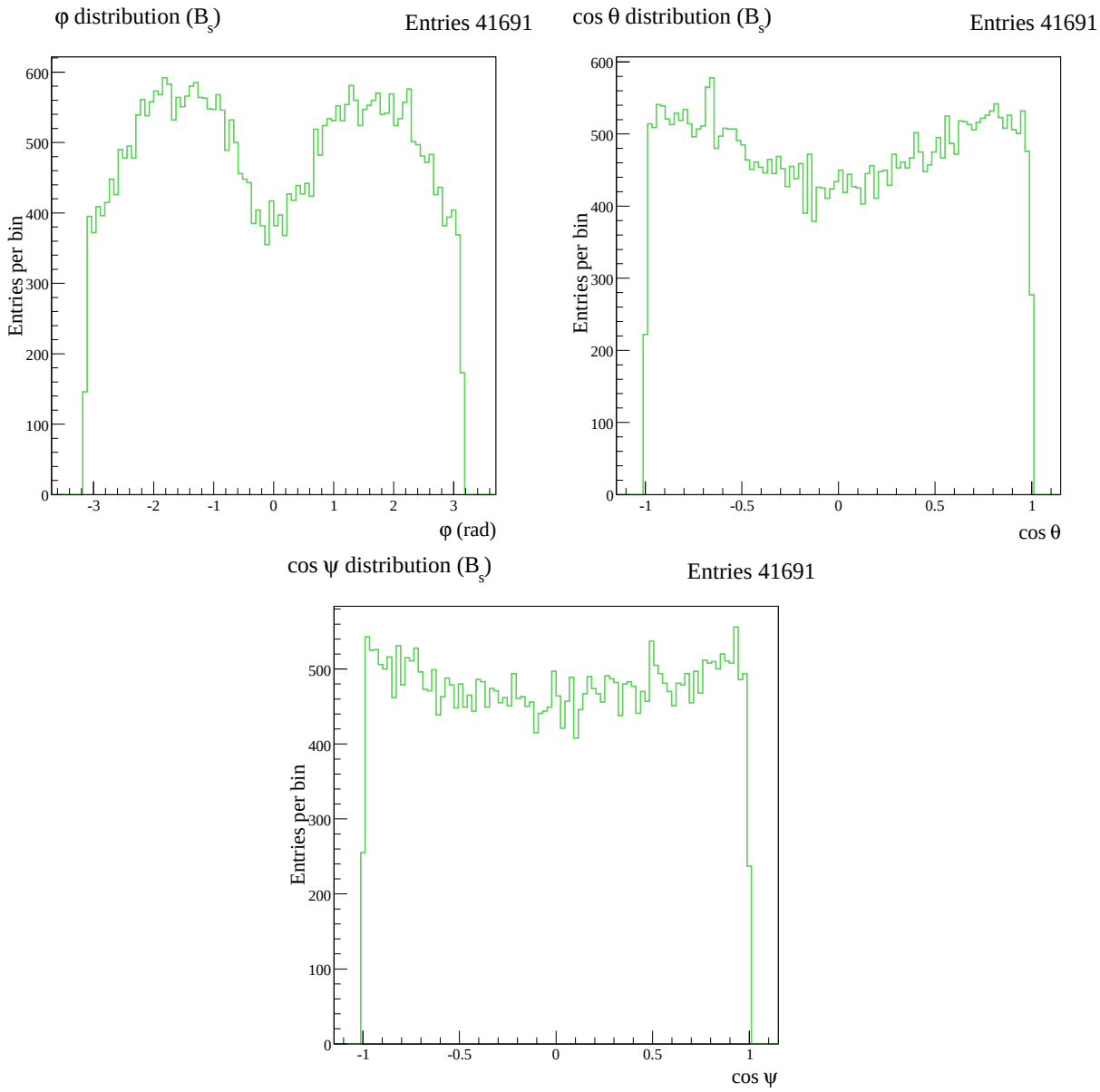

Figure A.4: Variable distributions for the angular variables ϕ (top), $\cos\theta$ (bottom left), and $\cos\psi$ (bottom right) for the $B_s^0 \to J/\psi\phi$.

Appendix B

Calculation of efficiencies

B.1 B_d^0

B.1.1 Unswapped efficiencies.

We calculated the integrals ξ_i by means of the definition of a Monte Carlo integral, i.e.,

$$\xi_i = \frac{8\pi}{N_{gen}} \sum_{j=1}^{N_{gen}} f_i(\boldsymbol{\omega}_j)\epsilon(\boldsymbol{\omega}_j) \tag{B.1}$$

where $N_{gen} = 1 \times 10^7$ is the number of generated events for each transversal variable.

As we have already mentioned, the efficiency polynomial is a product of three normalized polynomials: $p_1(\phi), p_2(\cos\theta)$, and $p_3(\cos\psi)$ given by

$$p_1(\phi) = \sum_{i=0}^{9} \alpha_i \phi^i, \tag{B.2}$$

$$p_2(\cos\theta) = \sum_{i=0}^{8} \beta_i (\cos\theta)^i, \tag{B.3}$$

$$p_1(\cos\psi) = \sum_{i=0}^{8} \gamma_i (\cos\psi)^i, \tag{B.4}$$

The coefficients α_i, β_i, and γ_i obtained from the normalization of the polynomials shown in Fig. B.1 are reported in Table B.1. The resulting unswapped efficiencies are shown in Table

B.2.

φ $(\times 10^{-3})$		$\cos\theta$ $(\times 10^{-1})$		$\cos\psi$ $(\times 10^{-1})$	
$\alpha_0 = 165.50$	$\alpha_6 = -1.02$	$\beta_0 = 4.69$	$\beta_6 = 31.52$	$\gamma_0 = 5.59$	$\gamma_6 = -17.45$
$\alpha_1 = -30.38$	$\alpha_7 = 0.62$	$\beta_1 = 0.46$	$\beta_7 = -0.56$	$\gamma_1 = -1.42$	$\gamma_7 = -1.34$
$\alpha_2 = -17.33$	$\alpha_8 = 0.050$	$\beta_2 = 6.33$	$\beta_8 = -14.50$	$\gamma_2 = -2.17$	$\gamma_8 = 10.29$
$\alpha_3 = 22.57$	$\alpha_9 = -0.026$	$\beta_3 = -1.45$		$\gamma_3 = -1.35$	
$\alpha_4 = 7.08$		$\beta_4 = -23.44$		$\gamma_4 = 7.43$	
$\alpha_5 = -5.62$		$\beta_5 = 1.51$		$\gamma_5 = 0.99$	

Table B.1: Coefficients of the polynomials $p_j(x_i)$

i	$\xi_i^{un}(\times 10^{-3})$
1	35.06
2	42.38
3	41.98
4	0.171
5	0.240
6	-0.020

Table B.2: Unswapped efficiencies for the B_d^0.

B.1.2 Swapped efficiencies.

For the swapped efficiencies, we need to obtain the polynomial $R(\boldsymbol{\omega})$, that is also composed by a product of three normalized polynomials, i.e.,

$$R(\boldsymbol{\omega}) = R_1(\phi)R_2(\cos\theta)R_3(\cos\psi) \tag{B.5}$$

To obtain this polynomials we did as follows: we divide the histogram for the swapped angular variable (using the information related to the incorrect assignment of the masses for the kaon and the pion) to the histogram of the corresponding unswapped angular variable. After this, we fit the resulting histogram and obtain the coefficients for each of the three polynomials $R_i(x)$. Each one of them are normalized such that their integral is equal to one. The coefficients of this polynomials are shown in table B.3. The resulting swapped efficiencies are shown in table B.4.

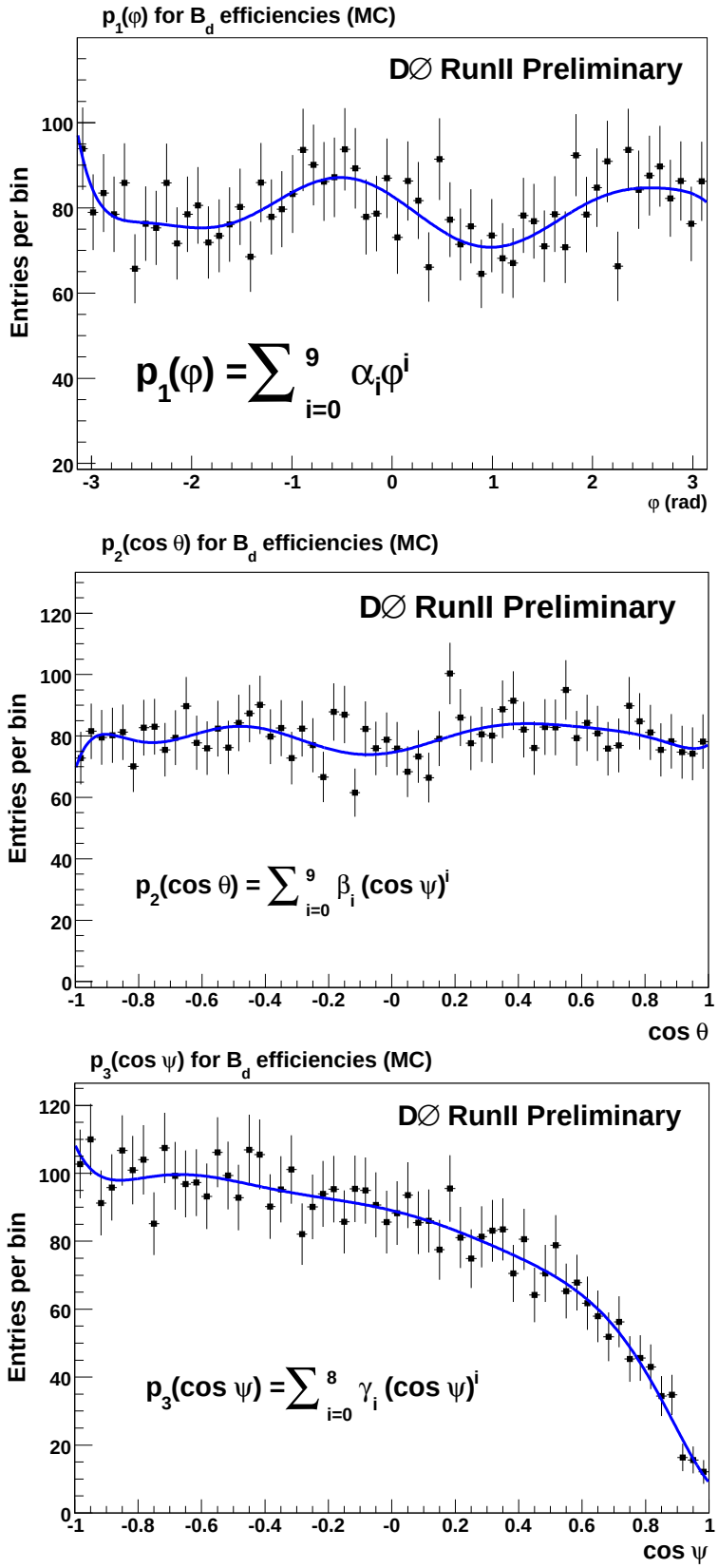

Figure B.1: Polynomials p_i for B^0_d unswapped efficiencies.

φ $(\times 10^{-3})$		$\cos\theta$ $(\times 10^{-1})$		$\cos\psi$ $(\times 10^{-1})$	
$\beta_0 = 146.39$	$\beta_6 = 2.83$	$\beta_0 = 4.66$	$\beta_6 = -54.53$	$\beta_0 = 6.60$	$\beta_6 = -83.93$
$\beta_1 = -19.47$	$\beta_7 = 0.040$	$\beta_1 = 1.35$	$\beta_7 = -42.56$	$\beta_1 = -7.79$	$\beta_7 = 25.65$
$\beta_2 = 32.58$	$\beta_8 = -0.167$	$\beta_2 = 2.59$	$\beta_8 = 35.39$	$\beta_2 = -15.64$	$\beta_8 = 44.0$
$\beta_3 = 9.32$		$\beta_3 = -21.95$		$\beta_3 = 16.98$	
$\beta_4 = -15.80$		$\beta_4 = 16.67$		$\beta_4 = 53.57$	
$\beta_5 = -1.22$		$\beta_5 = 60.97$		$\beta_5 = -33.23$	

Table B.3: Coefficients of the polynomials for $R_j(x_i)$.

i	$\xi_i^{sw}(\times 10^{-4})$
1	14.54
2	23.24
3	22.80
4	−0.530
5	−0.789
6	0.054

Table B.4: Swapped efficiencies for the B_d^0.

B.2 B_s^0

As in the case of B_d^0, the efficiency polynomial ϵ^{B_s} is a product of three polynomials: $q_1(\phi), q_2(\cos\theta)$,and $q_3(\cos\psi)$ given by

$$q_1(\phi) = \sum_{i=0}^{9} \nu_i \phi^i, \tag{B.6}$$

$$q_2(\cos\theta) = \sum_{i=0}^{8} \kappa_i (\cos\theta)^i, \tag{B.7}$$

$$q_1(\cos\psi) = \sum_{i=0}^{8} \lambda_i (\cos\psi)^i, \tag{B.8}$$

The coefficients ν_i, κ_i, and λ_i obtained from the normalization of the polynomials shown in Fig. B.2 are reported in Table B.5. The resulting efficiencies are shown in Table B.6.

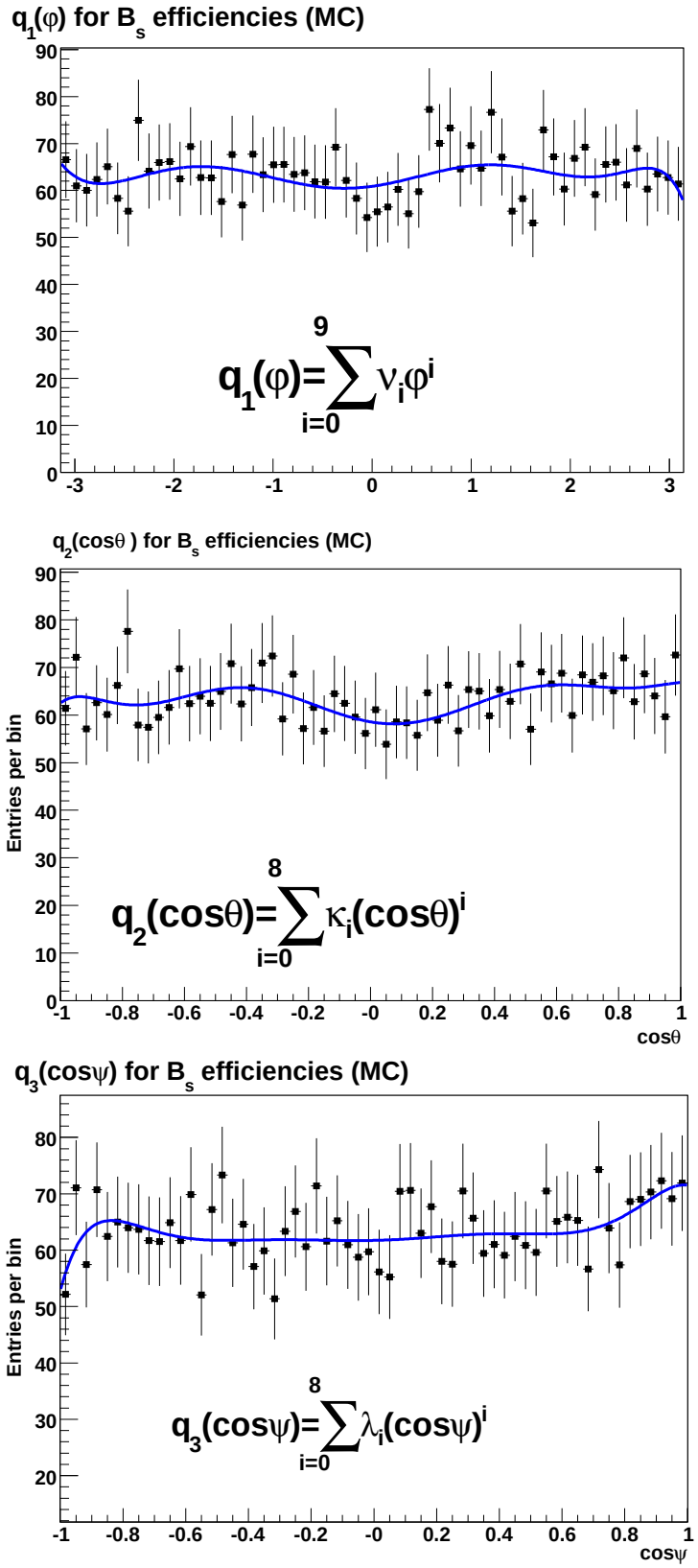

Figure B.2: Polynomials q_i for B_s^0 efficiencies.

φ $(\times 10^{-3})$		$\cos\theta$ $(\times 10^{-1})$		$\cos\psi$ $(\times 10^{-2})$	
$\nu_0 = 153.26$	$\nu_6 = 0.582$	$\kappa_0 = 4.62$	$\kappa_6 = 22.11$	$\lambda_0 = 48.81$	$\lambda_6 = 130.97$
$\nu_1 = 7.28$	$\nu_7 = 0.0064$	$\kappa_1 = -0.858$	$\kappa_7 = 4.42$	$\lambda_1 = 0.964$	$\lambda_7 = 27.45$
$\nu_2 = 11.53$	$\nu_8 = -0.026$	$\kappa_2 = 5.34$	$\kappa_8 = -9.35$	$\lambda_2 = 9.02$	$\lambda_8 = -8.34$
$\nu_3 = -4.80$	$\nu_9 = -0.0042$	$\kappa_3 = 5.45$		$\lambda_3 = 4.33$	
$\nu_4 = -4.32$		$\kappa_4 = -17.62$		$\lambda_4 = -56.31$	
$\nu_5 = 0.727$		$\kappa_5 = -8.84$		$\lambda_5 = -25.32$	

Table B.5: Coefficients of the polynomials $q_j(x_i)$.

i	$\xi_i(\times 10^{-3})$
1	41.01
2	39.36
3	39.01
4	0.0094
5	-0.011
6	0.015

Table B.6: B_s^0 efficiencies.

Appendix C

Swap of the mass for K and π in the decay $B_d^0 \to J/\psi K^{*0}$.

In the decay of B_d^0 under study, we have the problem of the correct assignment of the masses of the final products came from K^{*0}. We are looking to compare mass distributions of the swapped candidates to their correctly reconstructed counterparts. All the plots in this appendix were generated with a mass window $(5160.5, 5385.5)$ MeV/c^2. Since we are interested in the signal mass, not in the background mass, we apply an extra cut of PDL> 100μm in data; this is for making a better comparison of the signal peaks between data and Monte Carlo.

On top left and right of Fig. C.1 there are the comparison of the mass distributions of the candidates reconstructed with correct $K\pi$ mass assignment to the same for the candidates in which incorrect mass assignment was preferred by the selection algorithm. On the bottom of the same figures, there are the contrast fo the B_d^0 peaks in data with the combined B_d^0 peak in Monte Carlo. We attribute the width difference in these peak to an additional smearing which is not modeled in Monte Carlo. The size of this smearing, σ_{smear} can be estimated by in-quadrature substraction between the peak width in Monte Carlo combined plot (34.74 MeV/c^2) from the width of peak in data (38.41 MeV/c^2), which yields $\sigma_{smear} = 16.37$ MeV/c^2.

We fit the incorrect mass assignment plot to a double Gaussian to obtain two widths, σ_n and σ_w, the offset ΔM_{sw} with respect to the mean of combined Gaussian, and the ratio of the wide component to the total, f_w. We correct the smaller width to be adjusted for the detector smearing not modeled in Monte Carlo by $\sigma_n \to \sqrt{\sigma_n^2 + \sigma_{smear}^2}$. Finally, we also need to obtain the fraction f_{sw} of the number of swapped candidates to the total.

The final equation that models the swapped mass in this decay is given by Eq. (4.4), and the values of the parameters are given in Table C.1.

Parameter	
σ_w	73.86 ± 37.24
σ_n	38.03 ± 8.23
ΔM_{sw}	-3.0 ± 1.2
f_w	51.28
f_{sw}	13.30

Table C.1: Fit of parameters related with the mis-assignment for the $K \leftrightarrow \pi$ mass. All this values are fixed in the likelihood fit.

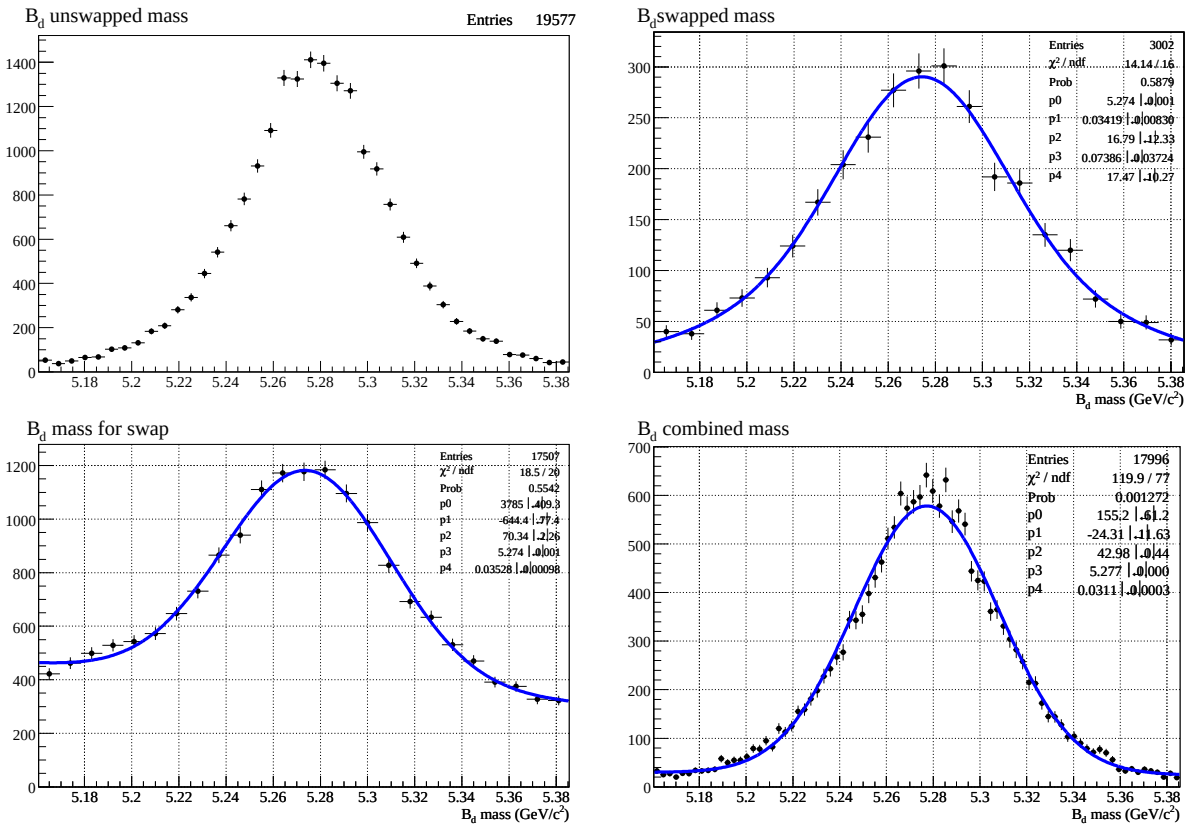

Figure C.1: Plots related with the misassignment for the $K \leftrightarrow \pi$ mass.

Appendix D

Projecting fit results on the angular distributions.

To projecting fit results on the angular distributions for the signal [Eqs. (1.69) and (1.54)], it is necessary to eliminate the explicit inclusion of the efficiency in the angular distributions. To make this, we proceed as follows:

- Apply a cut of $c\tau > 100\mu$m to the angular distributions (in the case of B_d^0, we only deal with the unswapped angular distributions) taking into account only the mass peak window;

- Take the form of the background from the sidebands and make a background substraction in the mass peak window with the correct fraction for the background in this region. With this procedure, we obtained at this step a signal distribution only affected by the efficiency;

- Correct the obtained distribution in the last step dividing by the corresponding efficiency distribution. With this, we obtained a pure signal distribution;

- Overimpose the projection of the corresponding variable on the pure signal distribution with the values of all the parameters fixed from the results reported in the tables of final results for each meson.

The analytical shape of φ projection is obtained by integrating the signal PDF [Eq. (1.69) for B_d^0 and Eq. (1.54) for B_s^0) over $\cos\theta, \cos\psi$, and t. Similarly, $\cos\theta$ and $\cos\psi$ projections are obtained by integrating the signal PDF over the other two transversity variables and time. The analytical expressions for the B_d^0 are the following:

$$\begin{aligned}\frac{d\mathcal{P}}{d\varphi} = \;& \cos^2\lambda^x \tfrac{3}{8\pi}\left[|B_0^x|^2\left(2-\tfrac{4}{3}\cos^2\varphi\right)+|B_\parallel^x|^x\left(2-\tfrac{4}{3}\sin^2\varphi\right)+\tfrac{4}{3}|B_\perp^x|^2\right]+\\ & +\sin^2\lambda^x\tfrac{3}{8\pi}\left(2-\tfrac{4}{3}\cos^2\varphi\right)-\tfrac{\sqrt{6}}{32}\sin 2\lambda^x\sin 2\varphi\cos\left(\beta_\parallel^x-\delta_S^x\right)|B_\parallel|^x \end{aligned} \tag{D.1}$$

$$\begin{aligned}\frac{d\mathcal{P}}{d\cos\theta} &= \cos^2\lambda^x\left[\frac{3}{8}\left(|B_0^x|^2+|B_\parallel^x|^2\right)\left(1+\cos^2\theta\right)+\frac{3}{4}|B_\perp^x|^2\left(1-\cos^2\theta\right)\right]\\ &+ \sin^2\lambda^x\frac{3}{8}\left(1+\cos^2\theta\right)\end{aligned} \tag{D.2}$$

$$\begin{aligned}\frac{d\mathcal{P}}{d\cos\psi} &= \cos^2\lambda^x\left[\frac{3}{4}\left(1-|B_0^x|^2\right)+\left(\frac{9}{4}|B_0^x|^2-\frac{3}{4}\right)\cos^2\psi\right]+\frac{1}{2}\sin^2\lambda^x\\ &+ \frac{\sqrt{3}}{2}\sin 2\lambda^x\,\cos\psi\,\cos\delta_S^x\,|B_0^x|\end{aligned} \tag{D.3}$$

where x stands for prompt and non prompt.

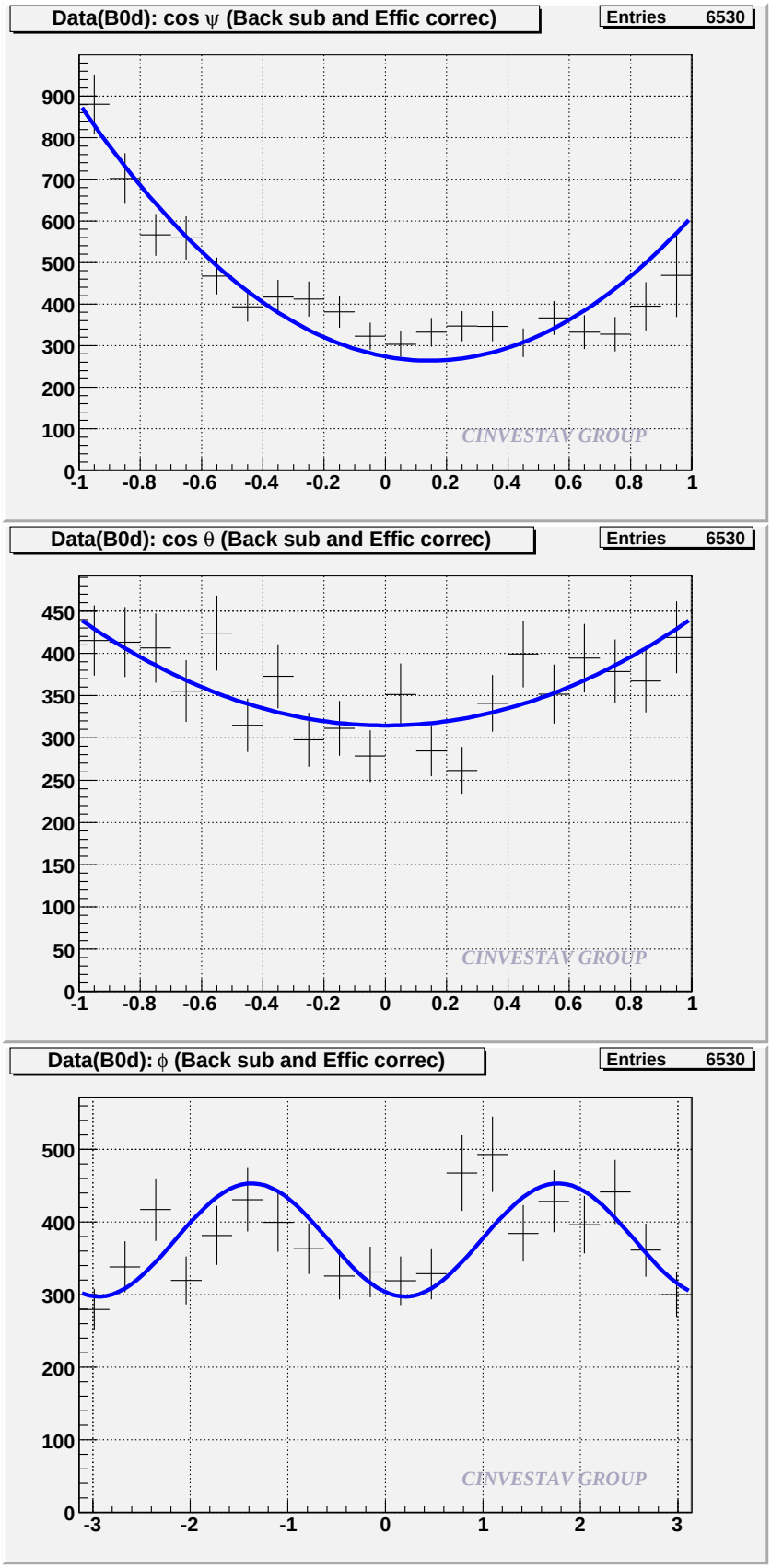

Figure D.1: Angular projections for the three angular variables $\cos\psi$ (top), $\cos\theta$ (middle), and ϕ (bottom) for the B_d^0. The points with error bars represent the data (sideband substracted), and the curves represent the fit projections.

Appendix E

Monte Carlo weighting

The MonteCarlo(MC) Sample Generated after reconstruction is not equal for certain kinematic variables. As a consequence any kind of physics result mixing MonteCarlo and Real Data should be proved to be independent of this differences or modify the MC to be similar to data. Since a tunning of a MC is quite complicated we decided to use a weighting method to correct the MC. We use the transverse momentum of the J/ψ for both decays, since we have an identification of the muon in our detector. Such a method was implemented in the following way:

1. Apply the same cuts to both samples MC and DATA. The cuts are the same as in from the selection chapter with an extra cut of $c\tau > 100\mu$m, we also divide the sample in two regions one central and other forward this is based in the pseudorapidity of the leading muon coming from the J/ψ.

2. Make the distributions that we want to see the effect on. In this case we choose as representatives the pT of the particles we reconstruct and some angular distribution of them

3. We make a background subtraction for each distribution; because we are only generating the signal for the MC. For the mass model we use a Gaussian of the signal an a 2 degree polynomial from the background. We take as a signal region 3σ ($\sigma(B_d) = 37.5$

MeV/c^2 from the mean of the Gaussian (Mean(B_d) = 5273 MeV/c^2, Mean(B_s) = 5361 MeV/c^2) and as sidebands of background from 4σ to 9σ from the mean.

4. Using this we create 2 kinds of distributions for each variable one for the signal region we can call the DistSignalBkgrd and other for the Sideband Region: DistSB

5. We calculate the number of events of background in the signal region (fbgkr) using Fit of the mass distribution.

6. We normalize the DistSB to have the same number of events that fbgkr , then we subtracted it from MCDistSignalBkgrd, for each variable, obtaining the desired distribution corresponding only to the signal DistSignal.

7. Normalize the DistSignal to have the same events as in the corresponding MC distribution MCDistSignal. Since in MC we only have signal.

8. Divide DistSignal/MCDistSignal to obtain the weight distribution WeightDist, in the ideal case if both distribution were equal then the resulting WeightDist, will be flat centered in 1. This can be for each variable, as we said before using the J/ψ distribution. Next we make a fit to the distributions this is to take in account the low statistic at high momentum.

9. Using the resulting fit, we weight all other distribution obtaining the following corrections.

10. When the fit probability is near to zero, we correct by the $p_T(J/\psi)$ histogram instead by the function.

In summary we have find a method to correct the difference in the distribution between MC and DATA.

For the present version of this note, we correct both the B_d^0 and the B_s^0 distributions using the histogram.

For the sake of space, we will show here only some distributions related to the central region.

E.1 MC for B_d^0

E.1.1 Central region

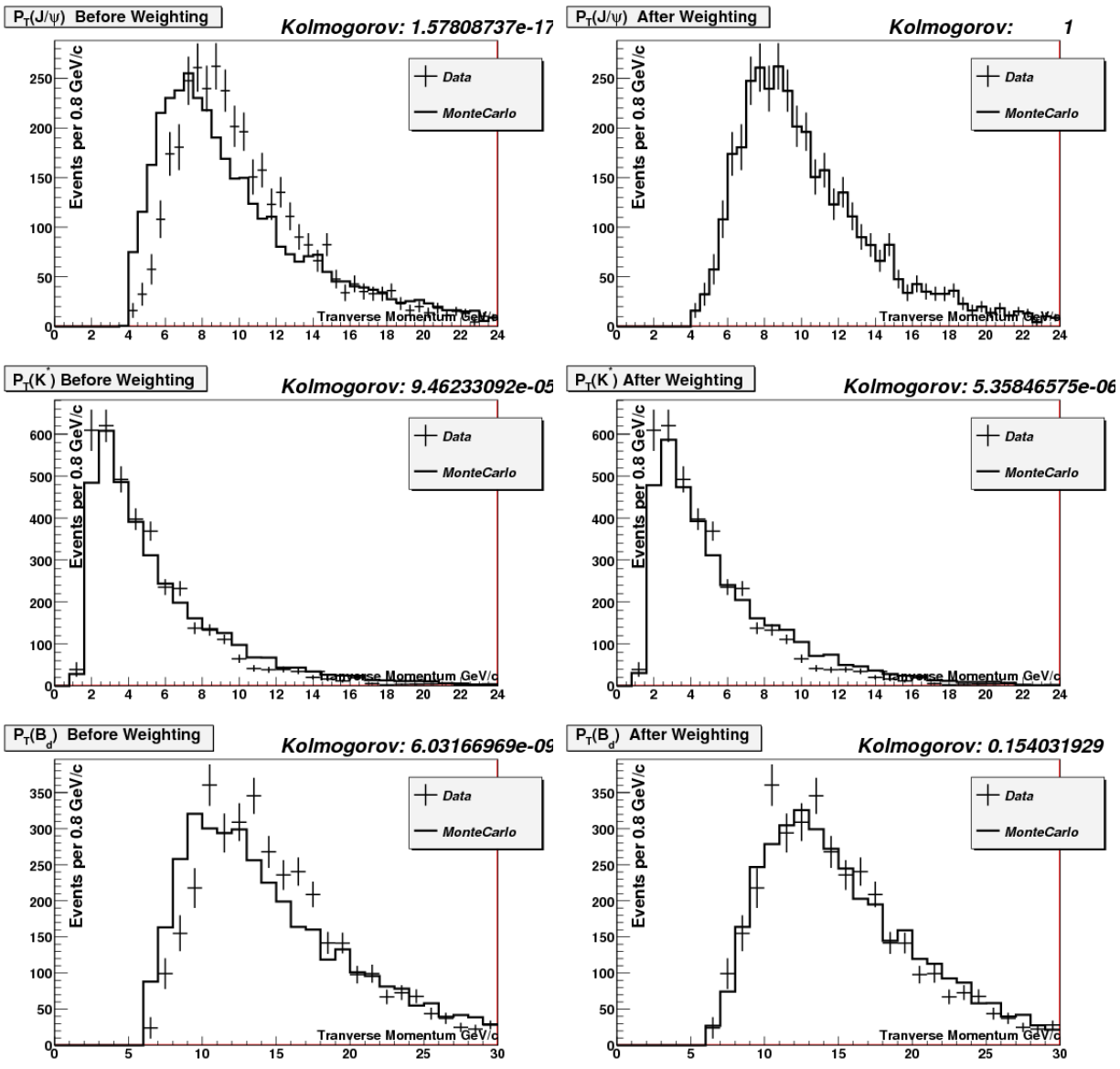

Figure E.1: MC correction of the $p_T(J/\psi)$, $p_T(K^{*0})$, and $p_T(B_d^0)$ for the B_d^0. Left column before weighting, right after. Solid line: MC. Points: data. Forward region.

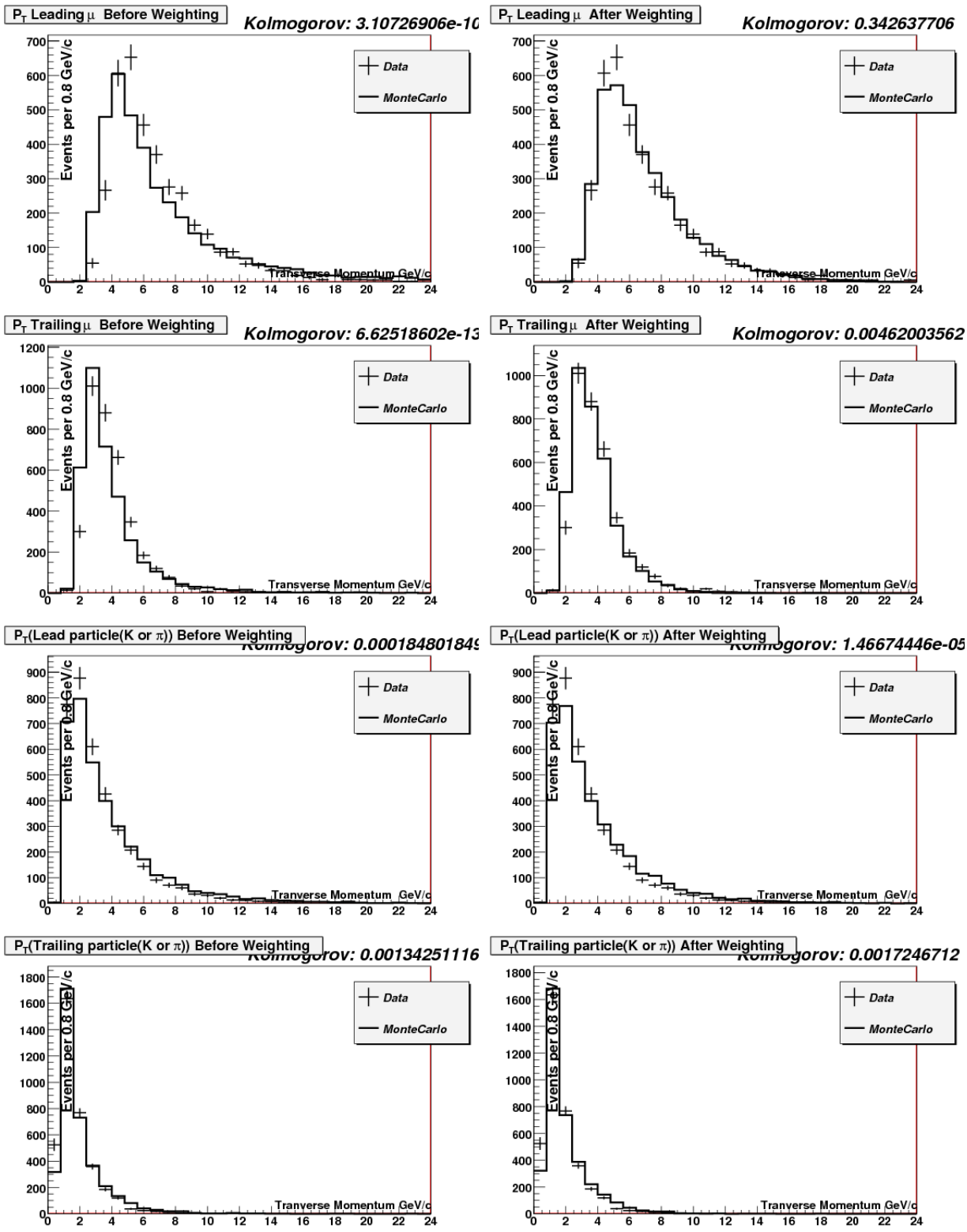

Figure E.2: MC correction of the transverse momentum of the leading muon, $p_T(\mu^{lead})$ trailing muon, $p_T(\mu^{trail})$, leading particle (K or π) $p_T^{lead}(K,\mu)$, and trailing particle (K or π) $p_T^{trail}(K,\mu)$ for the B_d^0. Left column before weighting, right after. Solid line: MC. Points: data. Central region.

E.1.2 Forward region

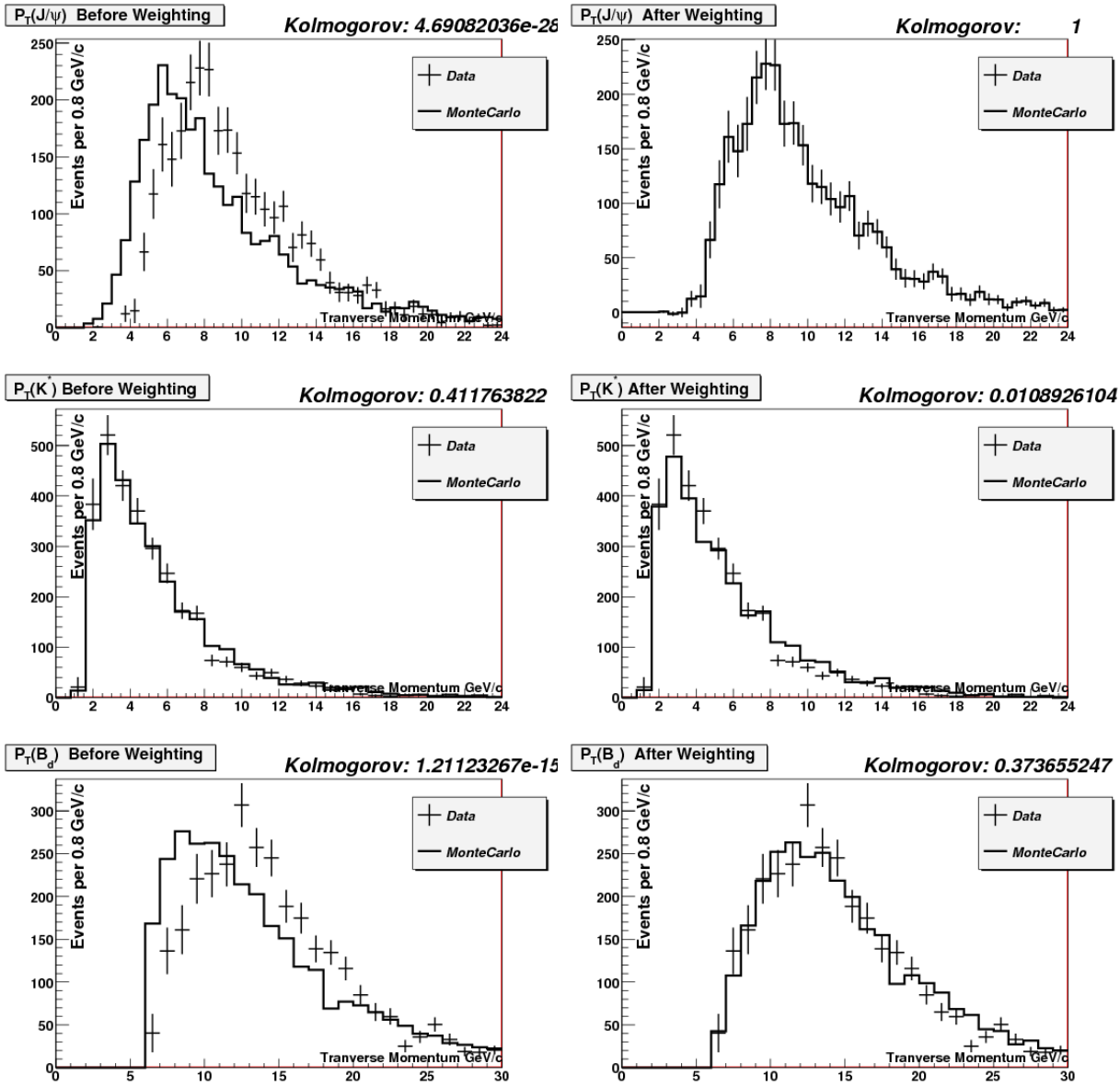

Figure E.3: MC correction of the $p_T(J/\psi)$, $p_T(K^{*0})$, and $p_T(B_d^0)$ for the B_d^0. Left column before weighting, right after. Solid line: MC. Points: data. Forward region.

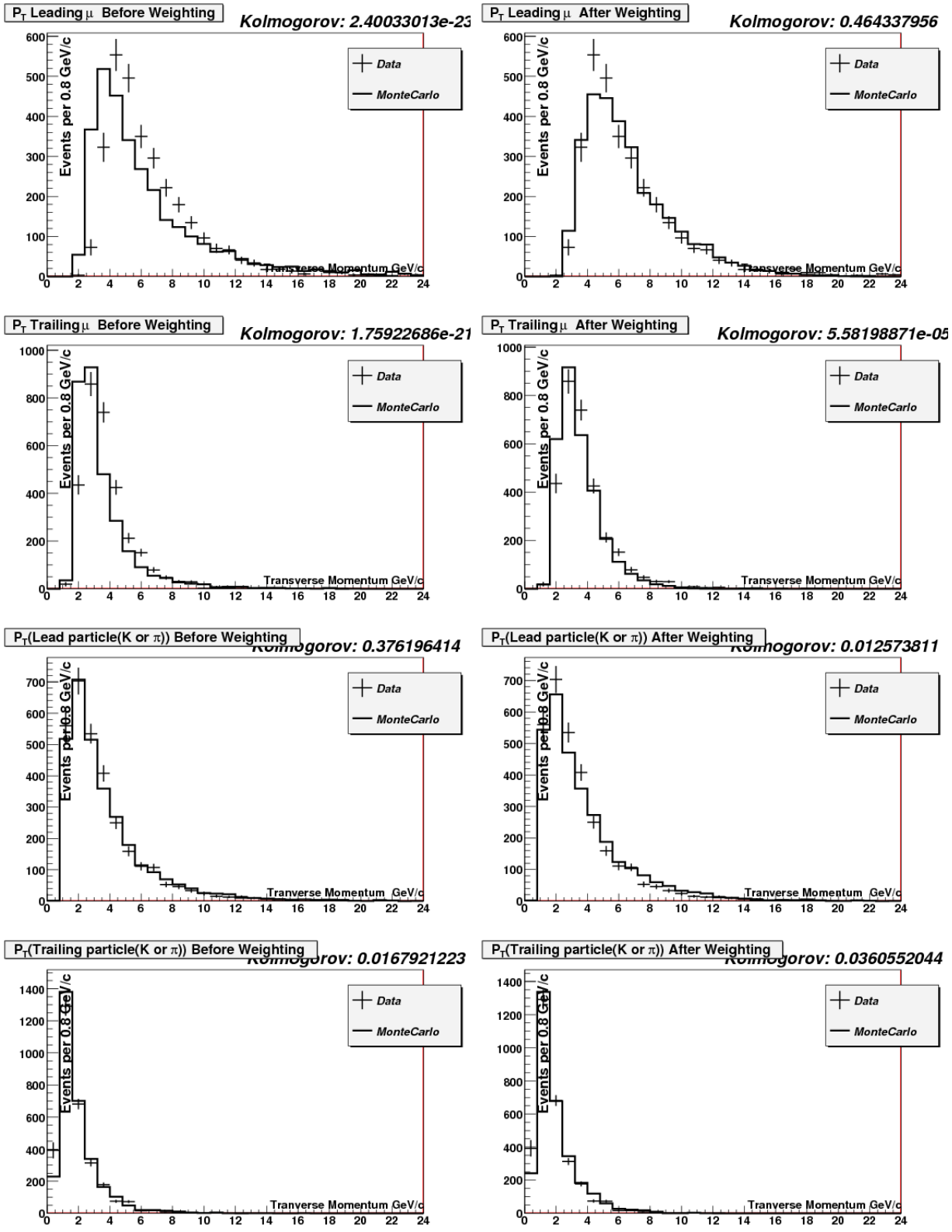

Figure E.4: MC correction of the transverse momentum of the leading muon, $p_T(\mu^{lead})$ trailing muon, $p_T(\mu^{trail})$, leading particle (K or π) $p_T^{lead}(K,\mu)$, and trailing particle (K or π) $p_T^{trail}(K,\mu)$ for the B_d^0. Left column before weighting, right after. Solid line: MC. Points: data. Forward region.

E.2 MC for B_s^0

E.2.1 Central region

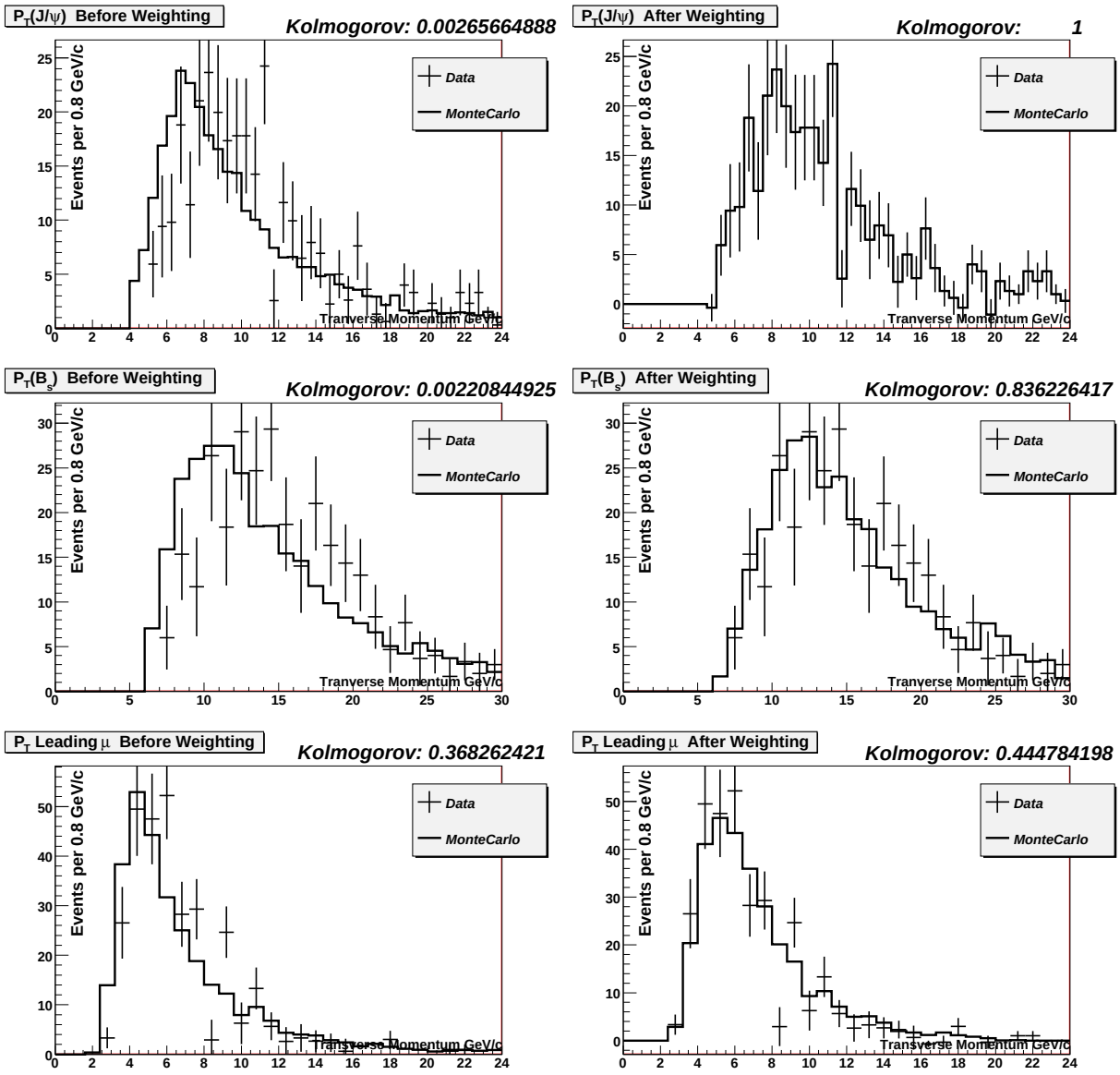

Figure E.5: MC correction of the $p_T(J/\psi)$, $p_T(B_s^0)$, and $p_T(\mu^{lead})$ for the B_s^0. Left column before weighting, right after. Solid line: MC. Points: data. Central region.

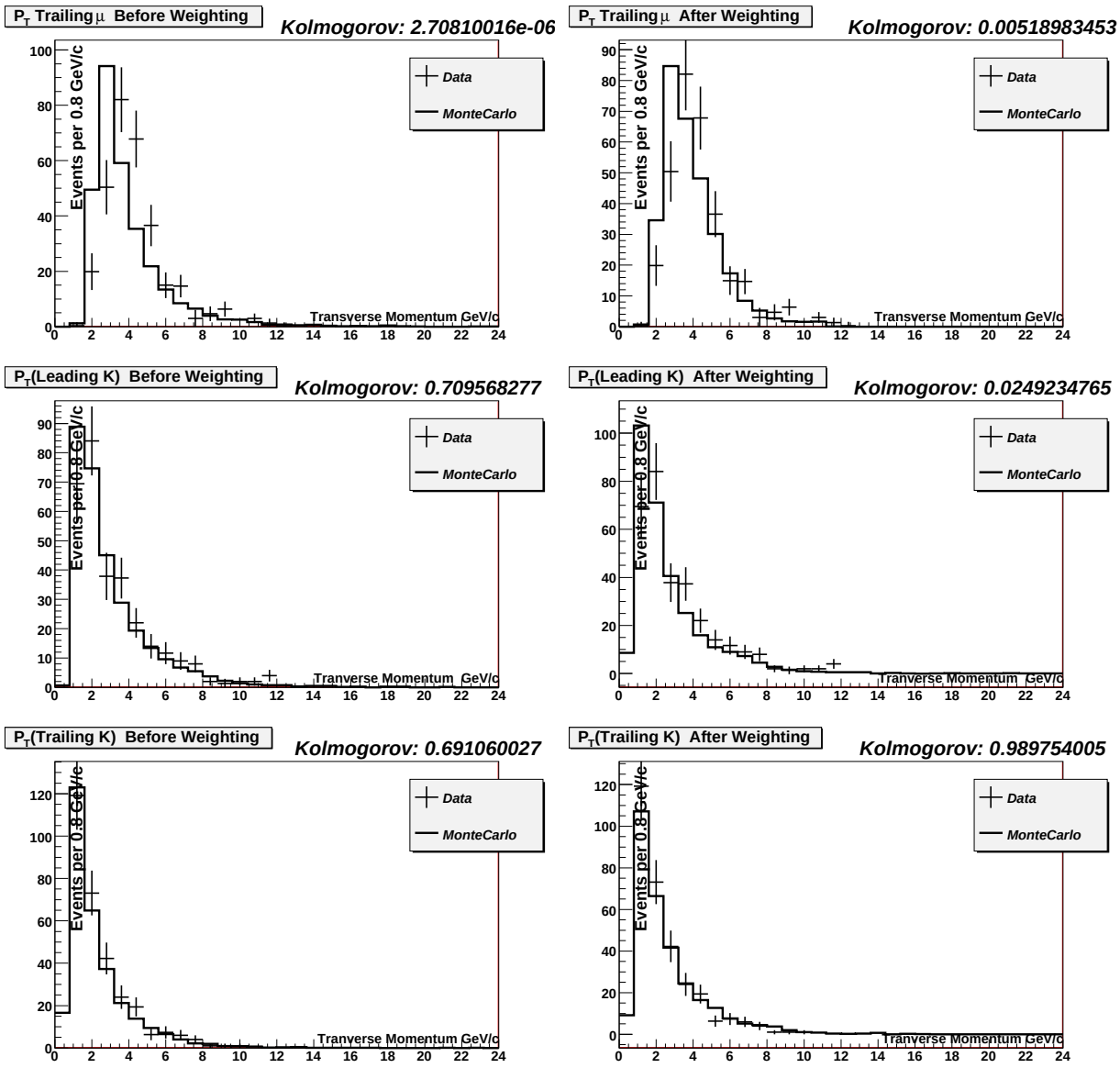

Figure E.6: MC correction of the $p_T(\mu^{trail})$, $P_T(K^+)$ and $p_T(K^-)$. for the B_s^0. Left column before weighting, right after. Solid line: MC. Points: data. Central region.

Forward region

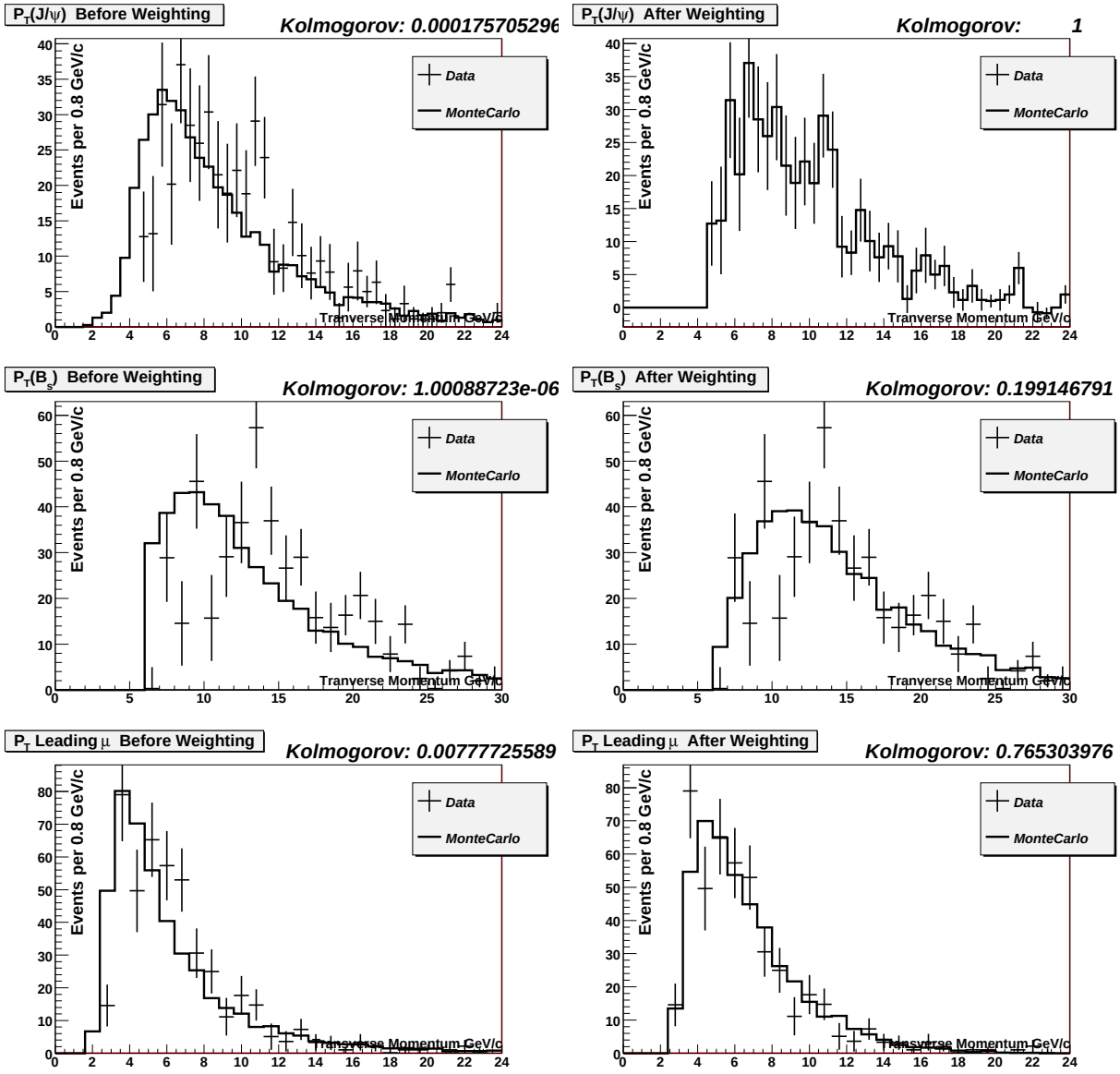

Figure E.7: MC correction of the $p_T(J/\psi)$, $p_T(B_s^0)$, and $p_T(\mu^{lead})$ for the B_s^0. Left column before weighting, right after. Solid line: MC. Points: data. Forward region.

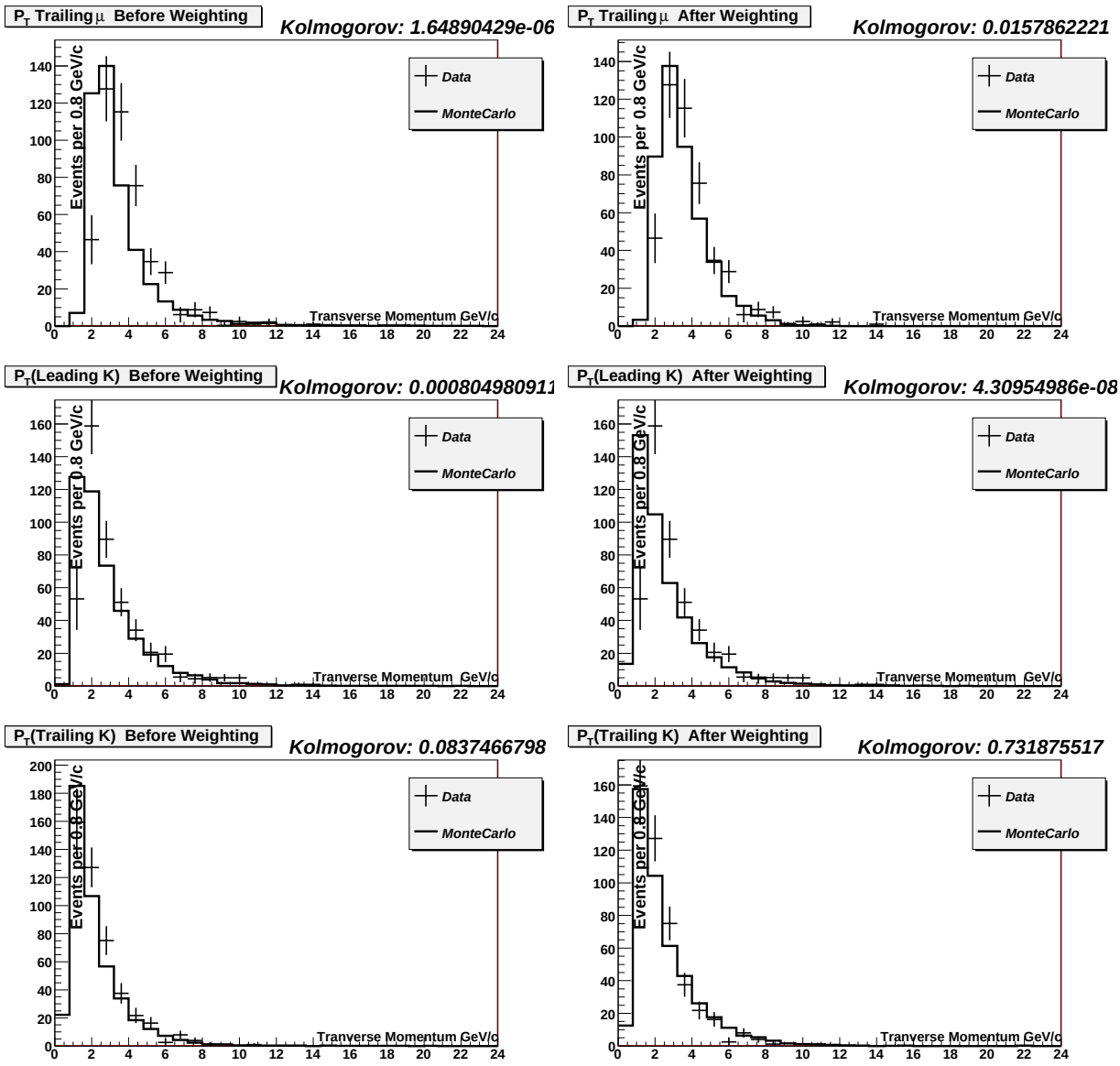

Figure E.8: MC correction of the $p_T(\mu^{trail})$, $p_T(K^+)$, and $p_T(K^-$ for the B_s^0. Left column before weighting, right after. Solid line: MC. Points: data. Forward region.

Bibliography

[1] V. Abazov *et al.* [D0 Collaboration], Phys. Rev. D**74**, 112002 (2006);
F. Abe *et al.* [CDF Collaboration], Phys. Rev. Lett. **80**, 2057 (1998);
A. Abulencia *et al.* [CDF Collaboration], Phys. Rev. Lett. **97**, 242003 (2006);
V. Abazov *et al.* [D0 Collaboration], Phys. Rev. Lett. **97**, 021802 (2006).

[2] B. Aubert *et al.* [BaBar Collaboration], Phys. Rev. D**73**, 012004 (2006);
K. Abe *et al.* [Belle Collaboration], Phys. Rev. D**71**, 072003 (2005).

[3] A. Lenz and U. Nierste, JHEP **06**, 072 (2007).

[4] T. Aaltonen *et al.* [CDF collaboration], Phys. Rev. Lett. **100**, 121803 (2008); V. Abazov *et al.* [D0 Collaboration], Phys. Rev. D**76**, 057101 (2007).

[5] E. Franco *et al.*, Nucl. Phys. B **633**, 212 (2002).

[6] *"Combined CDF and DØ upper limits on standard model Higgs boson production at high mass (155-200 GeV) with* $3.0\, fb^{-1}$ *of data"*. Preliminary results.
http://www-d0.fnal.gov/Run2Physics/WWW/results/prelim/HIGGS/H64/

[7] C. Amsler *et al* [Particle Data Group], Phys. Lett. B **667**, 1 (2008);
http://pdg.lbl.gov.

[8] V. Abazov *et al.* [D0 Collaboration], Phys. Rev. Let. **98**, 121801 (2007).

[9] "*CP Violation in the renormalizable theory of weak interactions*" Prog. Theor. Phys. **49**, 625 (1973).

[10] N. Cabibbo Phys. Rev. Lett. **10**, 531 (1963).

[11] L.L Cahu and W.Y. Keung, Phys. Rev. Lett. **53**, 1802 (1984).

[12] L. Wolfeinstein, Phys. Rev Lett. **51**, 1945 (1983).

[13] A.S. Dighe, I. Dunietz, and R. Fleischer. Eur. Phys. J. **C6**, 647 (1999).

[14] I. Dunietz, R. Fleischer, and U. Nierste. Phys. Rev. D**63**, 114015 (2001).

[15] S. T'Jampens. Ph. D. Thesis. Université Paris XI. UFR Scientifique D'Orsay (2002).

[16] B. Aubert *et al.* [BaBar Collaboration], Phys. Rev. D**71**, 032005 (2005).

[17] T. E. Browder, K. Honscheid, and D. Pedrini, Annu. Rev. Nucl. Part. Sci **46**, 395 (1996).

[18] O. F. Hernández, arXiv:9502355v1 [hep-ph] (2005).

[19] V. Abazov *et al.* [D0 Collaboration], arXiv:0802.2255 [hep-ex] (2008), submitted to Phys. Rev. Lett. .

[20] S. Nandi and U. Nierste, Phys. Rev. D**77**, 054010 (2008).

[21] M. Gronau and J. L. Rosner, arXiv:0808.3761v5 [hep-ph] (2008), submitted to Phys. Lett. B

[22] V. Abazov *et al.* [D0 Collaboration], Nucl. Instr. and Meth. Phys. Res. A **565**, 463 (2006).

[23] S. Abachi *et al.* [D0 Collaboration], Nucl. Instrum. Methods Phys. Res. A. **338**, (1994) 185.

[24] *"Three Dimensional Computer Program (TOSCA) for nonlinear electromagnetic fields"*. J. Simkin, C. Trowbridge RL-79-079 (1979).

[25] W. N. Cottingham and D. A. Greenwood. "An Introduction to the Standard Model of Particle Physics". Cambridge University Press. 2003.

[26] G. A. García-Guerra. M. Sc. Thesis. CINVESTAV-México. 2006. *http://www.fis.cinvestav.mx/˜gagarcia/tm020706.pdf*

[27] L. Lyons. *Statistics for nuclear and particle physicists.* Cambridge University Press. 1999.

[28] E. De la Cruz-Burelo. PhD. Thesis. CINVESTAV-México. 2005.

[29] P. L. M. Podesta-Lerma. PhD. Thesis. CINVESTAV-México. 2005.

[30] V. Abazov *et al.* [D0 Collaboration], Phys. Rev. Lett. **94**, 042001 (2005).

[31] K. Abe *et al.* [Belle Collaboration], Phys. Rev. Lett. **95**, 091601 (2005).

[32] V. Abazov *et al.* [D0 Collaboration], Phys. Rev. Lett. **99**, 241801 (2007).

[33] Y. I. Azimov, Phys. Atom. Nucl. **59** (1996) 856, and references therein.

[34] "*The DO object management system: DOom*" *http* : $//www - d0.fnal.gov/computing/infrastructure/d0om/d0om.html$

[35] An object oriented analysis framework $http : //root.cern.ch/$

[36] standard format for Monte Carlo generators output *http* : $//cepa.fnal.gov/psm/stdhep/$

[37] GEANT detector description and simulation tool *http* : $//wwwasd.web.cern.ch/wwwasd/geant/$

[38] Pythia $http : //www - d0.fnal.gov/computing/MonteCarlo/generators/pythia.html$ Pythia main page $http : //home.thep.lu.se/ \sim torbjorn/Pythia.html$ Monte Carlo generation using Pythia and QQ
$http : //www - d0.fnal.gov/ kinyip/bphysics/MCinstruction.html$
Cookbook guide for Monte Carlo production
$http : //www.hep.ph.ic.ac.uk/ villeneu/mcprod/cook_book.html$

[39] D. J. Lange, Nucl. Instrum. Meth. **A462**, 152, (2001); for details of the decay models in the package, please see *http* : *//www.slac.stanford.edu/ lange/EvtGen.*

[40] http://d0server1.fnal.gov/users/nomerot/Run2A/B_ANA.html

[41] Offline Run Quality Database, *http* : *//d0db.fnal.gov/qualitygrabber/qualQueries.html.*

[42] "Studies of $\Upsilon(1S)$ bottomonium state production with the DØ Detector at Fermilab"; D0 Note 4264; D. Bauer, J. Huang and A. Zieminski; 2004.

[43] "*Inclusive B lifetime at DØ* ", E. Cruz-Burelo, DØ Note 4257

[44] "*Charged B lifetime at DØ* ", P. Podesta, DØ Note 4273

[45] *B_s^0 and B_d^0 angular-mass-PDL and CP-violating phase analysis.* G.A. García-Guerra, H. Castilla-Valdez, A. Sánchez-Hernández, P. Podesta-Lerma. DØNote 5228. 2006.

[46] *Update of the $B_d^0 \to J/\psi K^{*0}$ and $B_s^0 \to J/\psi\phi$ untagged analyses with 2.8 fb^{-1}* G.A. García-Guerra, H. Castilla-Valdez, A. Sánchez-Hernández, P. Podesta-Lerma. DØNote 5456. 2007.

[47] K Anikeev. Ph. D. Thesis. MIT. 2004.

[48] Geometry Files where provided by A. Sopczak:
*clued*0 : */home/sopczak/ricksgeometries*

[49] *http://www-clued0.fnal.gov/˜dstrom/p17.09.00.html,*
http://www-clued0.fnal.gov/˜dstrom/p17.09.03.html,
http://www-clued0.fnal.gov/˜gweber/b-phys/runIIb-aadsts.html

[50] *http://d0db.fnal.gov/qualitygrabber/qualQueries.html*

[51] *http://d0server1.fnal.gov/users/nomerot/Run2A/BANA/Dskim.html*

[52] *http://d0server1.fnal.gov/users/nomerot/Run2A/BANA.html*